Title
Source Localization of the Gastric Slow Wave

Permalink
https://escholarship.org/uc/item/1k21791c

Author
Allegra, Alexis B

Publication Date
2021

Peer reviewed|Thesis/dissertation

UNIVERSITY OF CALIFORNIA SAN DIEGO

Source Localization of the Gastric Slow Wave

A dissertation submitted in partial satisfaction of the
requirements for the degree Doctor of Philosophy

in

Electrical Engineering (Signal and Image Processing)

by

Alexis Beatrice Allegra

Committee in charge:

Professor Todd P. Coleman, Chair
Professor William Hodgkiss, Co-Chair
Professor Truong Nguyen
Professor Piya Pal
Professor Geert W. Schmid-Schoenbein

2021

The dissertation of Alexis Beatrice Allegra is approved, and it is acceptable in quality and form for publication on microfilm and electronically.

University of California San Diego

2021

DEDICATION

This work is dedicated to everyone who supported me on my winding journey to get here.

Ron Lasser, who planted a seed.

Wade Lowdermilk, who encouraged me to reach higher and helped provide me with resources to both work and perform my research.

My parents, for their continued love, support and excitement as I walked this path.

Daniel Carr, my husband, partner, and best friend who continuously reminded me that I was good enough and smart enough to accomplish my goals.

To all of my family and friends, thank you for believing in me, supporting me, and helping me get here.

To Cassini may you find your way among the stars, we love you always.

EPIGRAPH

Any sufficiently advanced technology is indistinguishable from magic.

—Arthur C. Clarke

It was our use of probability theory as logic that has enabled us to do so easily what was impossible for those who thought of probability as a physical phenomenon associated with ”randomness”. Quite the opposite; we have thought of probability distributions as carriers of information.

—Edwin Thompson Jaynes

TABLE OF CONTENTS

LIST OF FIGURES

LIST OF TABLES

ACKNOWLEDGEMENTS

I would like to acknowledge Professor Todd P. Coleman for his support as the chair of my committee and the guiding force in my research. His dedication and guidance in this research has been critical to its success. I would also like to acknowledge Professor William Hodgkiss as my co-chair for his patience and support throughout my time at UCSD.

The entire Neural Interaction Laboratory was instrumental in my success, providing meaningful discussions and whiteboard sessions that allowed me to clarify my research and goals. The collaboration with other lab members was critical to this research.

Finally to my ECE study group, Leverett and Derek Bezanson, thank you for making the coursework portion of this fun!

Chapter 1, in full, is a reprint of the material as it appears in PLOS ONE, October 2019. Alexis B. Allegra, Armen A. Gharibans, Gabriel E. Schamberg, David C. Kunkel, Todd P. Coleman, 2019. The dissertation author was the primary investigator and author of this paper.

Chapter 2, in full, has been submitted for publication to IEEE Transactions on Biomedical Engineering, 2021. Alexis B. Allegra, David C. Kunkel, and Todd P. Coleman The dissertation author was the primary investigator and author of this paper.

Chapter 3, in full, has been prepared for publication. Alexis B. Allegra., Jonas F. Kurniawan; David C. Kunkel; Timothy Pham; Andrew K.L. Nguyen; Nathan L.J. Sit Boris Tjhia, Andrew J. Shin and Todd P. Coleman. The dissertation author was the primary investigator and author of this paper.

VITA

2007	B. S. in Electrical Engineering *cum laude*, Tufts University, Boston MA
2017	M. S. in Electrical Engineering Signal and Image Processing, University of California San Diego, La Jolla CA
2021	Ph. D. in Electrical Engineering (Signal and Image Processing), University of California San Diego, La Jolla CA

PUBLICATIONS

A. B. Allegra, J. F Kurniawan, K. C. David, T. Pham, A. K.L. Nguyen, N. L.J. Sit, B. Tjhia, A. J. Shin, and T. P. Coleman, ”Biopotential Electrode Array Optimization for Source Localization of the Gastric Slow Wave,” 2021, manuscript prepared for publication.

A. B. Allegra, K. C. David, and T. P. Coleman, Model Selection Procedures for Bayesian Inference Based Source Localization of the Gastric Slow Wave, 2021, manuscript submitted for publication.

Agrusa, Anjulie S., et al. ”Robust Methods to Detect Abnormal Initiation in the Gastric Slow Wave from Cutaneous Recordings.” 2020 42nd Annual International Conference of the IEEE Engineering in Medicine & Biology Society (EMBC). IEEE, 2020.

Alexis Allegra, et. al., “Bayesian inverse methods for spatiotemporal characterization of gastric electrical activity from cutaneous multi-electrode recordings”, *PLOS ONE*, 314, 2019.

Agrusa, Anjulie S., et al. A deep convolutional neural network approach to classify normal and abnormal gastric slow wave initiation from the high resolution electrogastrogram. IEEE transactions on biomedical engineering 67.3 (2019): 854-867

Mendoza, Marcela, Alexis Allegra, and Todd P. Coleman. Bayesian Lasso posterior sampling via parallelized measure transport. arXiv preprint arXiv:1801.02106 (2018).

Coleman, Todd P., et al. Diffeomorphism learning via relative entropy constrained optimal transport. Signal and Information Processing (GlobalSIP), 2016 IEEE Global Conference.

Allegra, Alexis, Michael Spinali, and David Carey. Automating Microwave Measurements with Software Defined Synthetic Instrumentation. Microwave Journal 58.3 (2015): 100-+.

Allegra, Alexis B., et al. Method of performing synthetic instrument based noise analysis using proportional bandwidth spectrum analysis techniques. U.S. Patent No. 8,717,006. 6 May 2014

Carey, David, et al. A methodology for enhancing legacy TPS/ATS sustainability via employing Synthetic Instrumentation technology. AUTOTESTCON, 2011 IEEE.

Lowdermilk, Wade, et al. Proportional bandwidth spectrum analysis in a synthetic instrument. AUTOTESTCON, 2010 IEEE.

ABSTRACT OF THE DISSERTATION

Source Localization of the Gastric Slow Wave

by

Alexis Beatrice Allegra

Doctor of Philosophy in Electrical Engineering (Signal and Image Processing)

University of California San Diego, 2021

Professor Todd P. Coleman, Chair
Professor William Hodgkiss, Co-Chair

Gastrointestinal (GI) problems give rise to 10 percent of initial patient visits to their primary care physician. Although blockages and infections are easy to diagnose, more than half of GI disorders involve abnormal functioning of the GI tract, where diagnosis entails subjective symptom-based questionnaires or objective but invasive, intermittent procedures in specialized centers. Although common procedures capture motor aspects of gastric function, which do not correlate with symptoms or treatment response, recent findings with invasive electrical recordings show that spatiotemporal patterns of the gastric slow wave are associated with diagnosis, symptoms, and treatment response. In this dissertation, I develop non-invasive approaches to extract this spatial information. Using Computed Tomography (CT) or Magnetic Resonance Imaging (MRI) scans from human subjects, I simulate normative and disordered gastric surface electrical activity along with associated abdominal activity. I employ Bayesian inference to solve the ill-posed inverse problem of estimating gastric surface activity from cutaneous multi-electrode human subject recordings as well as the simulated observations. In Chapter 1, I explore Bayesian inference methods with different prior distributions to extract spatiotemporal patterns and identify an optimal technique termed Group Sparsity whose prior enforces both spatial sparsity in the recovered sources and temporal smoothness. In Chapter 2, I explore a modification to the inference method and develop automated techniques for isolating an optimal solution for the Group Sparsity approach. Finally in Chapter 3, Using Fisher information, I turn to exploring the limits of this problem by investigating how electrode size and density affect the reconstruction of the gastric slow wave. I find that there is an electrode array configuration that optimally trades off electrode noise variance with spatial resolution, both of which increase with electrode density. Ultimately, this research shows that the gastric slow wave can be non-invasively characterized with a recording from a cutaneous electrode array and medical imaging (CT or MRI). While my approach still requires a simultaneous invasive measure for complete validation, this body of work represents a critical step towards clinical non-invasive measures of gastric health.

Chapter 1

Bayesian inverse methods for spatiotemporal characterization of gastric electrical activity from cutaneous multi-electrode recordings

Introduction

Gastrointestinal (GI) problems are the second leading cause for missing work or school in the US [1], giving rise to 10% of the reasons a patient visits their physician, and costing $142 billion annually [2]. Symptom management is routinely used by primary care physicians, and patients are referred to GI specialists if symptoms persist, which happens most of the time [2]. While pathologic findings can be detected with a blood test, endoscopy, or imaging, oftentimes symptoms cannot be attributed to a medical condition despite appropriate workup. These disorders fall under the umbrella of functional and motility GI disorders such as Functional dyspepsia and gastroparesis (which affects Parkinson's and diabetes patients [3,4]). These disorders make up a majority of patient referrals to GI specialists.

The clinical gold standard for diagnosing motility disorders is gastric emptying, which typically involves imaging after ingestion of a meal containing radioactive tracer. However, gastric emptying does not correlate with symptoms [5] and is not associated with symptom improvement [6]: some drugs improve symptoms but not gastric emptying and vice versa [7–9]. In fact, the NIH Gastroparesis Consortium has recently recommended that improvement in gastric emptying not be considered a requirement for clinical drug trials in gastroparesis [5].

The GI system contains smooth muscle cells (SMCs) that are controlled by rhythmically oscillating slow waves, whose spatiotemporal coordination enables peristalsis to propel food through the GI tract [10,11]. It has been observed during surgery with invasive high-resolution electrical mapping of the stomach surface that direction and speed patterns of the gastric slow wave co-varies with functional GI disorders, such as gastroparesis, chronic nausea and vomiting, and functional dyspepsia [12,13]. In a normal functioning stomach, the slow wave is characterized by bands of electric-motor activity which initiate in the pacemaker region (near the fundus) and propagate in equipotential rings in the anterograde direction towards the pylorus [11]. It has also been shown that in patients with GI disorder diagnoses, abnormal initiation can occur, where the bands of activity initiate outside the pacemaker region and bifurcate into a retrograde propagating wave and anterograde propagating wave.

Moreover, recent findings show that features of mucosal multi-electrode recordings predict symptom improvement from gastric stimulation [14–16]. This suggests that new opportunities may emerge to phenotype, localize, and treat such disorders, if such information could be extracted non-invasively.

Conventional electrogastrography (EGG), a noninvasive technique for recording the gastric myoelectric activity using electrodes placed cutaneously on the abdominal surface overlying the stomach [17], is attractive in its non-invasiveness and simplicity in interpretation of a single waveform with spectral analysis. However, conventional EGG solely extracts spectral information [18] and it has been shown that spatial abnormalities can occur at normal frequencies and thus go undetected by conventional EGG [19]. This inability to capture spatial abnormalities that co-vary with functional GI disorders, as well as its inability to correlate with symptoms, might explain why conventional EGG is seldom used clinically [20]. Our recent advances with the high-resolution electrogastrogram (HR-EGG) [21], acquired non-invasively from cutaneous multi-electrode arrays, allows for extraction of abdominal wave propagation parameters at every time point (e.g. presence of a wave, propagation direction and speed). We have recently demonstrated that these features correlate with symptom severity in a population of GI patients spanning a wide range of BMI and ages [22]. This is significant, given the lack of association between symptom severity and gastric emptying. The HR-EGG, however, extracts spatial information relative to the cutaneous surface of the abdomen. From volume conduction, the voltages from cutaneous recordings are the results of an average of complex electrical sources from the gastric surface. Moreover, it was shown [12, 13, 23] that retrograde and anterograde waves from one or more sources can arise at the same time in the distal stomach, suggesting that cutaneous spatial analyses will not be able to resolve them. As such, it has yet to be determined if one can develop a fully non-invasive and simple signal acquisition procedure to reliably extract dynamic spatial patterns of gastric surface electrical activity.

In order to address the problem of non-invasively localizing the site of spatial abnormalities on the gastric surface, we here consider developing inverse methods to infer spatiotemporal electrical patterns on the stomach surface based upon multi-electrode abdominal recordings. Ideally this problem could be solved with a standard linear least squares method if the number electrodes in the observation array exceeds the number of unknowns we aim to infer. For instance, if a linear model relating the unknowns x to the observation array y is governed by a matrix A, then it is well-known that the least squares fit $\hat{x}(t)$ is given by:

$$\hat{x}(t) = (A^T A)^{-1} A^T y(t). \tag{1.1}$$

However, eq. (1.1) can only be implemented when A is full rank. When it is not, e.g. when the number of unknown variables exceeds the number of observations, the problem is considered ill-posed and there are infinitely many candidate solutions which are equally consistent with the data. One way to address this issue is to use Bayesian inference, in which a prior distribution is specified that enforces a unique solution to a regularized model-fitting problem.

Using computed tomography (CT) scans from human subjects, we simulate gastric surface electrical activity of stomachs for normative (with proximal wave generation and anterograde propagation) and disordered (with distal wave generation and retrograde and anterograde propagation) cases (see Figs 1.1 and 1.2). With a forward model to relate the gastric surface potentials to the abdominal surface potentials, we generate a simulated abdominal surface observation array positioned according to the same CT scan. To simplify the computational complexity of the problem, we exploit how circumferential bands of equal potential travel in the organoaxial direction [11] to construct a set of spatial basis functions defined on these annular rings of the gastric surface. These different basis functions represent different numbers of wavefronts per unit space. Thus, estimation of the gastric surface spatiotemporal electric activity is now in terms of estimating the time series of weight vectors.

Even with the simplification of the problem to a set of spatial basis functions, the estimation problem remains ill-posed. As such, we take a Bayesian inference perspective and develop different prior distributions on the time series of weight vectors, each of which pertains to an estimation problem for finding the Bayes optimal point estimate, also termed the Maximum a Posteriori (MAP) estimate. We consider three widely used prior distributions on the time series of weights: Tikhonov regularization, ℓ_1 regularization (which encourages sparsity in the number of active spatial wavefronts and can be solved with the LASSO), and a linear Gaussian state space model (which encourages temporal smoothness and can be solved with the Kalman smoother). In addition, we consider a recently developed [24] group sparsity prior which encourages both sparsity in active spatial wavefronts *and* temporal smoothness. Further, we implement a recently-developed computationally efficient procedure to construct the MAP estimate [25] associated with this group sparsity prior.

We demonstrate that the estimation algorithm pertaining to group sparsity has superior performance in comparison to all other methods, across a range of noise conditions, for both normative and disordered gastric activity. Region-specific wave direction information is calculated and consistent with normal (anterograde propagation in all regions) and abnormal (anterograde propagation on one side of wave origination and retrograde propagation on the other) cases. We apply these methods to cutaneous multi-electrode recordings of two human subjects who have the same clinical description of motor function, but different underlying diagnosed causes (diabetic gastroparesis in subject 1 and idiopathic gastroparesis in subject 2). We find statistically significant wave propagation in all regions for both subjects, anterograde activity in all stomach regions for subject 1, and retrograde activity in some stomach regions for subject 2.

Previous Work

Much of the previous work on solving the inverse problem to infer the gastric slow wave from cutaneous recordings is based on the magnetogastrogram (MGG) [26, 27] which measures the magnetic fields produced by the gastric electric currents. Although the MGG shows promise in its ability distinguish between normative and disordered gastric activity [27], it requires measuring the magnetic field with large environmentally controlled equipment [28, 29]. The HR-EGG signals, in comparison, do not require such shielding and have the potential to be deployed in ambulatory settings. [30].

One previous implementation of an inverse approach to gastric slow wave localization based on simulated abdominal surface electrical measurements utilized a highly detailed but generic ionic channel biophysical model using a generic torso model [31]. This previous approach leveraged classic linear regression (Tihkonov and Tikhonov-greensite) techniques that have been used in the EEG and ECG localization literature [31]. These regression methods attempt to combat the under-determinedness of the problem through the use of regularization either solely in the spatial domain with Tikhonov regression (as in [31, eqn 2]) or through the use of spatiotemporal regularization with Tikhonov-Greensite regularization (as in [31, eqn 3]) which uses a spatiotemporal basis [32] to accommodate spatiotemporal continuity in the solution.

Materials and Methods

Key to this study was the development of a three dimensional (3D) time evolving electrical model from which we could generate dynamic simulations. To accomplish this, we first extracted the 3D model of both the stomach and the abdominal surface from a human subject CT. We then developed models of normal and abnormal gastric slow wave electrical activity using a solution to a one-dimensional (1D) wave equation. To map this solution to the 3D stomach model, we sliced it along planes normal to a curve along the stomach which we term the organoaxial curve (see Fig 1.1). To map the dynamic 3D model of the stomach to the abdominal surface, we solve a standard forward model which assumes that the medium between the stomach surface and abdominal surface is homogeneous with fixed conductivity. The output of this is the simulated abdominal observation array of electric potentials into which we inject additive white Gaussian noise (AWGN) and then apply the aforementioned Bayesian inference techniques to solve the ill-conditioned inverse problem.

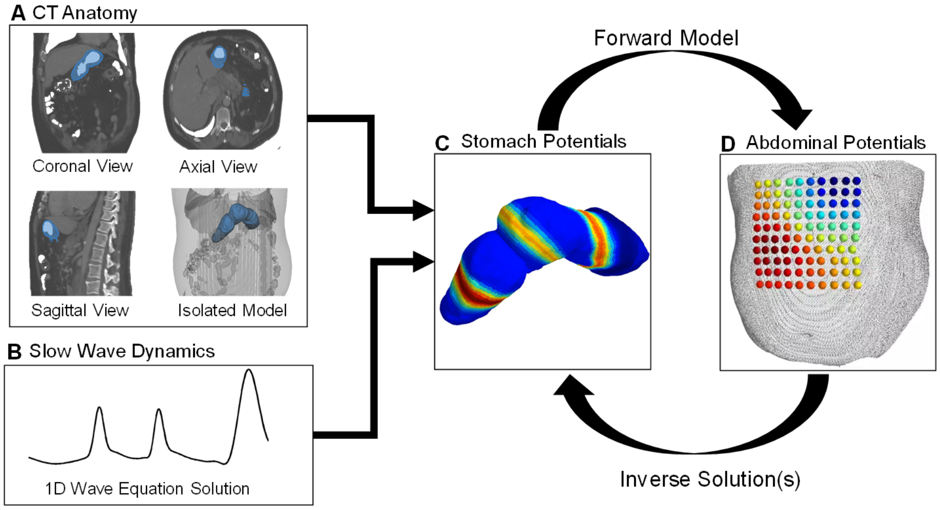

Figure 1.1: **Process Workflow** A) Using the 3 standard CT views, a 3D model of the stomach is extracted. B) We develop a spatially inhomogeneous solution to the 1D wave equation, pertaining to propagation down the organoaxial direction of the stomach, with region-specific amplitudes and speeds based upon recent findings in the literature from invasive human recordings. C) The 1D wave equation solution is mapped to the 3D model to generate the dynamic dipole moment solution. D) We solve a forward model to generate the dynamic simulated observations and inject additive measurement noise.

Simulation Development

3D Physiology

Using 3D Slicer, an open source medical imaging tool [33], we extract an anatomical 3D model of the stomach and abdomen. We placed fiducial points on the abdomen to estimate electrode positions and fiducial lines were drawn on the stomach model surface using a secondary tool (Meshlab) [34]. To simulate the averaging effect of the electrodes, the forward model was solved at several points around the fiducial electrode marker on the abdominal model and averaged together to generate the observation data $Y \in \mathbb{R}^{N \times T}$ where N is the number of electrodes and T is the number of time samples. For this simulation N is 100 (a 10x10 grid of electrodes) and T is 300 time samples at a sampling rate of 5 samples/second. To map the dynamic simulation of the gastric slow wave to the 3D model of the stomach, three equi-spaced fiducial lines consisting of 120 spatial points were drawn along the surface of the stomach model (see Fig 1.2 for an example of one of the fiducial lines). From these lines, we derived a series of planes normal to the stomach, and created grouped rings of spatial points. The center-line of the planes forms the organoaxial curve. Onto each one of these rings, we mapped a value of the 1D wave equation solution as a function of time sample. This represents the activation of the normative stomach in equi-potential rings.

1-D Wave Equation

The gastric slow wave, like the heart, begins with the activation of a group of pacemaker cells on the greater curvature of the stomach [35]. The signal emitted spreads isotropically from the pacemaker region via activation of the interstitial cells of Cajal (ICC), which initiate muscle contractions through the corpus and antrum. Typically, less than 5 simultaneous slow wave wavefronts occur at any time in the human stomach [35].

Due to the continuous nature of the gastric slow wave, and the clear wave-like propagation, we simulated a signal model based on the wave equation. In the normal simulation, wave activity begins in the proximal stomach and the wave direction is entirely anterograde (traveling from the proximal toward the distal stomach). As has been done with other gastric models of the slow wave [21], we ignored circumferential propagation of the serosal slow-wave and solved the

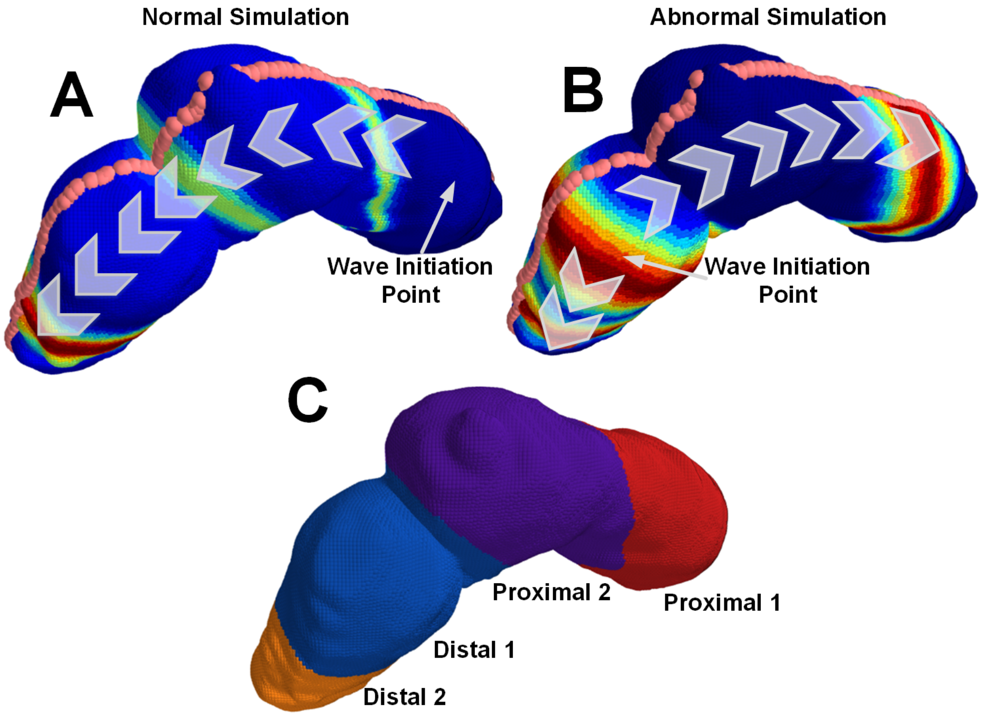

Figure 1.2: **Abnormal and Normal Simulation Propagation Directions** A) 3D physiology mapped normal simulation. The wave initiates in the proximal stomach and has only anterograde propagation. B) 3D physiology mapped abnormal simulation. The wave initiates in the distal stomach and has both retrograde and anterograde propagation. C) The different proximal and distal regions of the stomach

following 1D wave equation using a finite difference approach:

$$\frac{\partial^2 u}{\partial t^2} = c\left(x\right)^2 \frac{\partial^2 u}{\partial x^2} \tag{1.2}$$

where $c(x)$ is the stomach surface location dependent wave speed, and $u(x,t)$, the 1D wave equation solution, is the amplitude of the wave at each location x and time t. Gaussian pulses with a width of 35 mm were generated every 20 seconds (0.05 Hz) in the first proximal region of the stomach. The pulse width, in addition to the modulations of its speed and amplitude along the organoaxial direction of the stomach, were chosen to be consistent with the most recent description in the literature for healthy subjects [35–37]. Both the speed and amplitude were highest in the first proximal region (6.0 mm/s, 0.57 mV), followed by a reduction in the second proximal and first distal regions (3.0 mm/s, 0.25 mV), and finally increased in the second distal region (5.9 mm/s, 0.52 mV). See Fig 1.2 for a description of regions. Mur's boundary condition was used to ensure the pulses were absorbed into the pylorus rather than being reflected back into the stomach. The Courant-Friedrichs-Lewy condition dictated the temporal step-size to guarantee a converged finite-difference solution.

This same approach is used to develop a dynamic simulation for abnormal initiation. For this part of the simulation, we kept the pulse width as well as speed and amplitude of the wave constant, but modified the initial conditions so that wave patterns were consistent with the findings in invasive recordings [12]: a wave was initiated in the distal stomach and bifurcated into two waves, one propagating anterograde at more distal locations and the other retrograde at more proximal locations. Fig 1.2 describes the differences between the normal and abnormal initiation simulations.

Forward Model

The 3D stomach model is sliced into annular rings and the 1D wave equation is mapped onto the geometry to represent rings of equipotentials (Fig 1.3). This solution provides current dipole moments at each point in time, and each dipole is oriented along the organoaxial direction of the stomach [38], as seen in Fig 1.4A. We compute the estimated EGG signal at each electrode [39] as:

$$y_n(t) = \sum_{i=1}^{D} A_{n,i} x_i(t) + N_n(t) \tag{1.3}$$

where $y_n(t)$ is the signal received at each of the N electrodes, $A_{n,i}$ is the solution to the forward model at each of the D sources on the stomach surface, and $x_i(t)$ is the dipole moment at each source location and each instant in time. $N_n(t)$ is additive white Gaussian noise (AWGN) of adjustable variance σ^2, giving rise to adjustable signal-to-noise ratio (SNR) in simulations, in accordance with previous EEG simulation and inverse modeling methods [39].

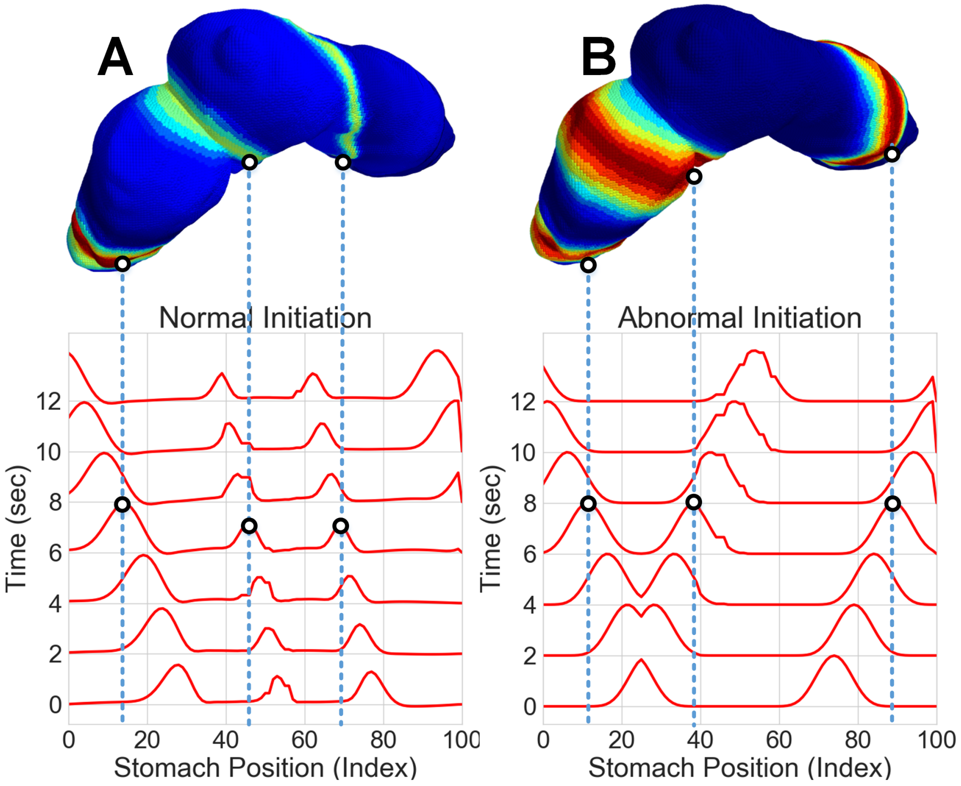

Figure 1.3: **Visualization of Source Activity Mapped to the 3D Stomach Model** A) 3D stomach model with the normal dynamic simulation mapped at the 6 second time point. The two dimensional time/space plot is shown below the 3D model. B) 3D stomach model with the abnormal dynamic simulation mapped at the 6 second time point. The two dimensional time/space plot is shown below the 3D model.

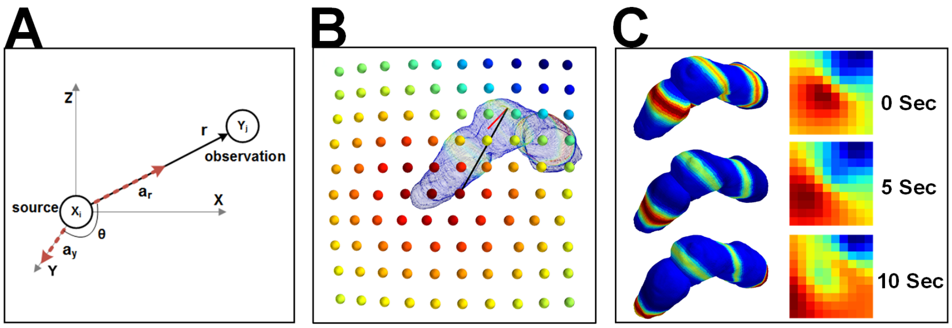

Figure 1.4: **Dynamic Dipole Moment Simulations and Forward Model** A) Forward model relationship between dynamic dipole moments (X) and observed abdominal surface potentials (Y) B) 3D models of dynamic dipole moments and observed array C) Time evolution of dipole moments and observations for normal simulation

For the purposes of this analysis, the body is modeled as a homogeneous medium which contains the stomach surface. The solution to the forward model reduces to an attenuation constant which depends on the positions of the source (stomach) and the sensor (abdomen). In matrix notation, the simulated observations are generated as $\overrightarrow{y}(t) = A\overrightarrow{x}(t) + \overrightarrow{N}(t)$, and the solution for the matrix is:

$$A_{n,i} = \frac{\cos\theta}{4\pi\sigma r_{n,i}^{2}} \tag{1.4}$$

where θ is the angle between the current dipole (oriented organoaxially) and the observation point on the abdominal surface, σ is the tissue conductivity (a constant due to the homogeneous medium), and r the straight line distance between the current dipole and the abdominal observation [38].

Inverse Solutions

Although the problem is ill-posed, we aim to take advantage of the fact that the electrical activity of the stomach has key physiologic mechanisms that commonly occur both in normal and diseased states. Specifically, (1) there is a small number of electrically active bands along the surface of the stomach, and further (2) they move continuously over time. We aim to take advantage of this prior physiologic knowledge to utilize Bayesian inference techniques to find an estimate of the gastric electrical activity over time. Since the electrically active bands propagate as waves along the gastric surface, we represent the stomach electrical activity at any point in time as a weighted combination of different spatial basis functions, each of which represents the numbers of wavefronts per unit space. As such, the estimation of electrical activity of the stomach over time, boils down to estimation of the vector of weights over time. We consider different models (prior distributions) of the weights over time which encode different subsets of the two aforementioned physiologic underpinnings of gastric electrical activity. As a baseline, we consider using Tikhonov regularization, the most common form of regularization in inverse problems, which neither encodes physiologic mechanism (1) nor continuous activity over time (2). To solely address (1), the small number of electrically active bands on the stomach surface, we use an L1 regularizer, which promotes sparsity in the number of active weights, and can be solved with the least absolute shrinkage (LASSO) estimation algorithm. To solely address (2), the smooth evolution of the waves, we use a Gaussian state space model, which promotes smoothness overtime and can be solved with the Kalman smoother. To address (1) and (2) in the same estimation method, we consider using a group sparsity model. Further, we use a computationally efficient procedure to solve the MAP estimation problem for this model.

Basis Functions

For the problem of estimating the stomach surface potentials, we take into consideration how the gastric slow wave contains bands of electrical activity that propagate as rings continuously along the gastric surface [11]. We thus represent the spatiotemporal activity on the gastric surface as a weighted combination of basis functions over space, where the functions are invariant with time but the weights are indexed by time. Under our assumption that the gastric slow wave travels along the organoaxial curve in rings of equi-potential, the bases are solely functions of the position along the one-dimensional organoaxial curve. This curve is visualized in Fig 1.2 as the points along the top of the geometry.

To construct the set of basis functions, we considered a spatial Fourier basis in which the different sinusoids represent different spatial frequencies, or number of wavefronts that exist per unit space:

$$(H)_{k,i} = \cos\left(\pi i \frac{k}{K}\right) \tag{1.5}$$

$$(H)_{k+\frac{K}{2},i} = \sin\left(\pi i \frac{k}{K}\right) \tag{1.6}$$

where $i = 0, \ldots, D-1$ represents the spatial index along the organoaxial curve, and k/K for

$k = 1, \ldots, K/2$ the relative spatial frequency component.

As such, we solve the problem with respect to basis functions of a line of sources and map the inverse result to the full ring of sources.

$$\overrightarrow{x}(t) = H^T \overrightarrow{w}(t) \tag{1.7}$$

where H^T is the basis matrix ($D \times K$) and $w_k(t)$ are the K time evolving weights. This reduces the problem to finding an optimum set of weights which are less than the total number of sources. Eq (1.3) becomes

$$y_n(t) = \sum_{i=1}^{D} A_{n,i} \sum_{k=1}^{K} h_{d,k} w_k(t) + N_n(t) \tag{1.8}$$

where $h_{d,k}$ is the index into the basis matrix and $w_k(t)$ is the kth weight. Eq (1.7) simplifies in matrix notation to:

$$\overrightarrow{y}(t) = AH^T \overrightarrow{w}(t) + \overrightarrow{N}(t). \tag{1.9}$$

MAP Estimation for Source Localization

With the measurement model with respect to the basis representation given by eq (1.8), which encodes the statistical model $p(Y|W)$, we formulate the localization problem as one of finding the Bayes optimal point estimate of the time series of weights, which maximizes $p(W|Y)$ over W for any set of measurements Y. This MAP estimation approach takes into consideration the measurement model $p(Y|W)$ along with the prior distribution $p(W)$ to identify a solution to our ill-posed problem. The general form of the MAP estimation procedure is as follows:

$$\hat{W}_{MAP} = \underset{W \in \mathbb{R}^{K \times T}}{\arg\max}\, p(W|Y) \tag{1.10}$$

where $p(W|Y)$ is the posterior probability of a set of weights W given a set of observations Y. Using Bayes' rule

$$p(W|Y) \quad = \quad \frac{p(W)p(Y|W)}{p(Y)}. \tag{1.11}$$

Since $p(Y)$ is not a function of W, and since the $-\log$ function is monotonically decreasing, the maximizer in eq. (1.10) is equivalent to the minimizer of eq. (1.12):

$$\hat{W}_{MAP} \quad = \quad \underset{W\in\mathbb{R}^{K\times T}}{\arg\min} \; -\log p(Y|W) - \log p(W). \tag{1.12}$$

Since the likelihoood $p(Y|W)$ is governed by the forward model and additive Gaussian noise model at the electrodes, from eq. (1.3), we have that the estimator in eq. (1.12) becomes:

$$\hat{W}_{MAP} \quad = \quad \underset{W\in\mathbb{R}^{K\times T}}{\arg\min} \sum_{t=0}^{T-1} ||\overrightarrow{y}(t) - AH^T\overrightarrow{w}(t)||_2^2 + \lambda \text{pen}(W) \tag{1.13}$$

where $-\log p(W)$ is proportional to the penalty term pen(W). In each inverse method described, it is this penalty term which will change to support the underlying model assumptions.

Our source estimate for any time t is then:

$$\hat{\overrightarrow{x}}(t) = H^T \hat{\overrightarrow{w}}_{MAP}(t) \tag{1.14}$$

We evaluate four different priors (pen(W)) over the weights, which encode different assumptions about smoothness and sparsity. First, we consider Tikhonov regularization, a classic penalty which was used in previous work [31] and is extensively used in EEG and EKG inverse analysis [40] but does not enforce smoothness or sparseness in the solution. Second, we consider pen(W) to be a sum of ℓ_1 penalties over $\overrightarrow{w}(t)$ so that eq (1.13) becomes a LASSO problem [41], which encourages sparsity in the solution. Third, we consider pen(W) to encode a linear Gaussian state space model so that the solution to eq (1.13) becomes a Kalman smoother, which has been applied to the problem of EEG source localization [42] and emphasizes smoothness (i.e. the solution at time t_1 is dependent on the solution at time t_0) in the model. Finally we consider a group sparsity prior, recently developed in [24] for robust spectrotemporal decomposition of time series, for which an efficient and modular solution of eq (1.13) with respect to this prior was recently developed in [25]. This group sparsity prior encourages spatial sparsity in the active wavefronts, akin to the LASSO, and encourages temporal smoothness, akin to the Kalman smoother. Each of these methods require finding one or more penalty coefficients λ. Because we generate the ground truth simulation, we find the optimum λ by minimizing the error between the solution found and the simulated data.

Tikhonov/Ridge Regression

Tikhonov ridge regression makes no assumptions about smoothness or sparsity but is a classic method for solving ill-conditioned problems, by imposing an ℓ_2-norm penalty on W:

$$\text{pen}(W) = \sum_{t=0}^{T-1} ||\Gamma \overrightarrow{w}(t)||_2^2 \tag{1.15}$$

for some square matrix Γ. Unlike the other methods, Tikhonov regression has a closed form solution:

$$\overrightarrow{w}_{ridge}(t) = ((AH)^T AH + \lambda \Gamma^T \Gamma)^{-1} (AH)^T Y(t) \tag{1.16}$$

Tikhonov regression has been applied to this problem with some success in previous work on gastric electrical source localization [31,43], hence it is included here with $\Gamma = I$ for completeness.

The LASSO

The LASSO is similar in formulation to Tikhonov regression except that is uses an ℓ_1-norm instead of an ℓ_2-norm. As a result, the LASSO encourages 0-valued weights which enforces sparsity in the solution:

$$\text{pen}(W) = \sum_{t=0}^{T-1} ||\overrightarrow{w}(t)||_1 \tag{1.17}$$

For this study we use the python Sci-kit Learn implementation of the LASSO [44].

The Kalman Smoother

The linear Gaussian state space model of the form

$$\overrightarrow{w}(t+1) = \overrightarrow{w}(t) + \overrightarrow{m}(t)$$

where each $\overrightarrow{m}(t)$ is a multivariate Gaussian with zero mean and covariance matrix Σ. This gives rise to the Kalman smoother as the MAP solution, which enforces smoothness in time. For $\Sigma = I$, the penalty is as follows:

$$\text{pen}(W) = ||\overrightarrow{w}(0)||_2^2 + \sum_{t=1}^{T-1} ||\overrightarrow{w}(t) - \overrightarrow{w}(t-1)||_2^2 \tag{1.18}$$

For implementation of the Kalman smoother we used the python pykalman package [45].

Group Sparsity

We here consider a group sparsity regularization technique that promotes sparsity among groups of coefficients [46] (in our case, weights on the spatial basis functions). For this problem, we establish groups of coefficients over time and impose the penalty on the first differences of the coefficients [47], which imposes temporal smoothness on evolution of the coefficients. As a result, only a sparse subset of the coefficients are non-zero at any given time, and those that are non-zero evolve smoothly over time. Formally, the penalty associated with eq (1.13) is given by:

$$\text{pen}(W) = \sum_{k=0}^{K-1} \left(\sum_{t=0}^{T-1} d_k(t)^2 \right)^{\frac{1}{2}} \tag{1.19}$$

where d represents the first differences (in time) of w:

$$\overrightarrow{d}(0) = \overrightarrow{w}(0) \tag{1.20a}$$

$$\overrightarrow{d}(t) = \overrightarrow{w}(t) - \overrightarrow{w}(t-1),\ t = 1, \ldots, T-1. \tag{1.20b}$$

The group LASSO can alternatively be viewed as the composition of ℓ_1 and ℓ_2-norms. To see this, first note that:

$$\left(\sum_{t=0}^{T-1} d_k(t)^2 \right)^{\frac{1}{2}} = ||\overrightarrow{d}_k||_2 \tag{1.21}$$

where $\overrightarrow{d}_k \triangleq [d_k(0), \ldots, d_k(T-1)]$ is a vector representing the first differences of the coefficients associated with the k^{th} basis function. Note the similarity in eq (1.20b) combined with eq (1.21) to the Kalman smoother penalty in eq (1.18), involving an ℓ_2 norm operating on temporal differences of the weight vectors. Using the representation in eq (1.21), we can rewrite eq (1.19) as:

$$\text{pen}(W) = \sum_{k=0}^{K-1} ||\overrightarrow{d}_k||_2 = ||\overrightarrow{v}||_1 \tag{1.22}$$

where $\overrightarrow{v} \triangleq [||\overrightarrow{d}_0||_2, \ldots, ||\overrightarrow{d}_{K-1}||_2]$. Succinctly, the penalty is an ℓ_1-norm of an ℓ_2-norm of time differences.

Under this interpretation, the ℓ_1 norm will allow for only a small number of non-zero elements in $\overrightarrow{v}$. Furthermore, $v_k = 0$ implies that $d_k(t) = 0$ for all t, which by virtue of eq (1.20), further implies that $w_k(t) = 0$ for all t. Considering only the k for which $v_k > 0$, we can consider the effect of the ℓ_2 norm in eq (1.21) for which, in analogy with the Kalman smoother, the non-zero weights $\overrightarrow{w}_k$ will evolve smoothly over time. As a result, we can expect the estimated sources

$\hat{X}$ to be composed of a small number of spatial frequency components evolving continuously in time.

We solve the proposed group LASSO problem using a consensus formulation of the alternating directions method of multipliers (ADMM) [48]. A generalized solution framework for using ADMM to estimate latent time-series using sparse regularization is presented in [25].

Calculation of Wave Propagation Parameters

We extracted estimates of the gastric surface potentials using the MAP estimation procedure in eq. (1.13) with the group sparsity prior pertaining to eq (1.19). With these gastric surface potentials along the organo-axial curve, we identified region-specific wave propagation features of the gastric slow wave. Specifically, we extracted directional information from the phases of the estimated electrical activity on the gastric surface. To determine when the directional information was statistically significant, we utilized a technique called the phase gradient directionality (PGD), which was originally developed in physics and neuroscience communities [49] and was recently employed to describe spatial patterns of GI activity with cutaneous multi-electrode recordings [21].

We extracted wave propagation features of the slow wave from the estimated patterns along the organoaxial curve by first performing the Hilbert transform on each individual estimated source on the curve $(\hat{x}_i(t) : i = 1,\ldots,D, t = 1,\ldots,T)$ in the array to extract instantaneous amplitude and phase information:

$$\hat{x}_i(t) + jHb\,[\hat{x}_i(t)] = a_i(t)e^{j\phi_i(t)}, \qquad i = 1,\ldots,D,\ t = 1,\ldots,T. \tag{1.23}$$

where j is defined to be $\sqrt{-1}$, Hb is the Hilbert transform, $\phi_i(t)$ is the instantaneous phase of the ith source on the organoaxial curve, and $a_i(t)$ is the instantaneous amplitude of source i.

We represented instantaneous phase information as a function of $\eta \in [0,1]$ which parameterizes the organoaxial curve. Discretizing this into D points, we have:

$$\phi(\eta_i, t) \equiv \phi_i(t), \quad i = 1, \ldots, D.$$

The spatial gradient of instantaneous phase, $\nabla_\eta \phi(\eta, t)$, was constructed at each point η_i along the organoaxial curve. Since the wave velocity vector v is normal to contours of constant phase, it satisfies

$$v(\eta, t) \propto -\nabla_\eta \phi(\eta, t). \tag{1.24}$$

We found the direction of source i at position η_i on the organoaxial curve, at time t, as

$$\Lambda_i(t) = \operatorname{sign}\left(-\nabla_\eta \phi(\eta, t)\right), \quad i = 1, \ldots, D,\ t = 1, \ldots, T. \tag{1.25}$$

In order to determine if a consistent wave is propagating in a sub-region of the stomach $\mathcal{R} \subset \{1, \ldots, D\}$, we calculate the PGD in that region, which is the ratio of the norm of the spatially averaged electrode velocities with the spatial average of the norm of electrode velocities:

$$PGD_{\mathcal{R}}(t) = \frac{\| \frac{1}{|\mathcal{R}|} \sum_{i \in \mathcal{R}} \nabla_\eta \phi(\eta_i, t) \|}{\frac{1}{|\mathcal{R}|} \sum_{i \in \mathcal{R}} \| \nabla_\eta \phi(\eta_i, t) \|}, \quad t = 1, \ldots, T \tag{1.26}$$

where $|\mathcal{R}|$ indicates the number of elements in the set $\mathcal{R}$ and velocities are replaced with $-\nabla\phi$ by virtue of eq (1.24). The PGD is a measure of how aligned the wave velocities at different positions are at any point in time, lies between 0 and 1, and equals 1 for planar waves [49]. Thus one interpretation of the PGD is as a measure of how "close" the activity is to being a plane wave, which is akin to what occurs for a normal slow-wave HR-EGG recordings, exhibiting predominantly anterograde propagation.

In order to control the false discovery rate associated with PGD, we defined statistically significant planar wave propagation to be present when $PGD_{\mathcal{R}}(t) > 0.5$ for 1 second or longer (see [21, Fig 2]). A beneficial side effect of computing the PGD is the computation of the wave velocities, from which we can identify anterograde or retrograde propagation at the time points for which the PGD is > 0.5 (i.e. a wave is present). The PGD results for the simulated data are compared in Table 1.1.

Human Data Processing

In simulated data, we can fully characterize the performance of our estimation procedures because the ground truth is known. We here considered applying the group sparsity estimation procedure, e.g. solving eq (1.13) with the penalty given by (1.19), on data collected from two human subjects. Specifically, we collected cutaneous 100-channel EGG recordings on two human subjects for whom CTs were available. Both subjects provided written consent to participate in the study and was part of an ongoing study at the University of California, San Diego, whose institutional review board provided ethical approval (IRB number 141069 ”A pilot trial to evaluate the utility of passive, skin-mounted electrodes to monitor the electrical activity of the human digestive system.”). We used a 10×10 electrode array with a reference electrode outside of the recording grid. The amplifier was a 256 channel GTec g.HIamp system, sampled at 256 Hz and then down-sampled to 4 Hz. We recorded 90 minutes of EGG data, 30 minutes into which the patient ate a small meal. Prior to analysis, we filtered the data with a band-pass filter with pass band frequencies between 0.015 Hz and 0.25 Hz. We showcase detailed results from one human subject whose CT was used for the aforementioned simulations. We compare summary findings of the human recorded data from both subjects in Table 1.2. The detailed simulation results and human recording results of the second subject are available in the supplemental materials.

Results

In both abnormal and normal scenarios we generated a simulated EGG observation array and injected AWGN with varying amounts of noise variance in terms of signal to noise ratio (50 dB SNR down to -4 dB SNR). From these noisy observations, we solved the inverse problem associated with each of the four previously described penalties and evaluated the efficacy of the methods with the correlation coefficient and root-mean-squared error (RMSE) against the true simulated sources. We also provide the 3D results on the geometry as well as a time/space representation of the surface electrical potentials. For the human data, we show the time/space representation of the inverse as well as wave stomach region specific descriptions of propagation pertaining to (a) retrograde vs anterograde propagation and (b) the fraction of time there is a statistically significant wave. These propagation patterns extract phase information across time and utilize the relationship between phase and direction underlying the planar wave equation to extract the PGD measure.

Simulated Data

Fig 1.5 shows the results of the group sparsity method against several different noise levels, for both normal (A) and abnormal (B) simulations. The plots for the other methods can be found in the supplemental materials. In low SNR scenarios, the inverse results visually tracked the ground truth in the distal portions of the stomach (positions 0-50) but struggled to reconstruct the wave in the proximal sections (positions 60-100). However, as the SNR increases, the inverse solution reconstructs the wave in all portions of the stomach. The same findings hold in the abnormal simulation. Additionally, the group sparsity is able to detect the separation of wavefronts in the distal stomach earlier and more clearly than the other methods (see Supporting Information S1, S2, and S3 Figs). In particular, for the 10 dB noise level, group sparsity is the only method that is able to resolve the two nearby wavefronts in the distal segment at 4 seconds into the recording. Additionally it is able to reconstruct wavefronts occurring in both the proximal and distal segments of the stomach simultaneously.

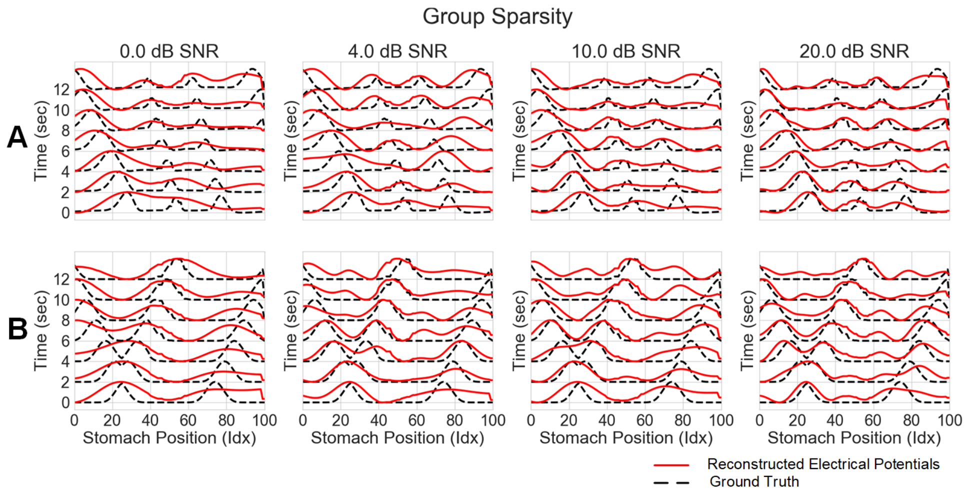

Figure 1.5: **Group Sparsity Inverse Solution on a Stomach Surface Line Across Noise Levels** A) Group sparsity results (electrical potentials) against the ground truth for normal initiation simulation. B) Group sparsity results (electrical potentials) against the ground truth for abnormal initiation. In both normal and abnormal simulations group sparsity is able to reconstruct the ground truth wave pattern even under unrealistically noisy conditions. Additionally the time at which it reconstructs the separate waves in the abnormal simulation is earlier (i.e. the waves are closer together) than in any of the other inverse methods

Fig 1.6 shows the correlation coefficient and RMSE mean across space for all methods, all noise levels, and both normal and abnormal simulations. The group sparsity method remains consistently higher in correlation coefficient and lower in RMSE across all noise levels and in both simulation scenarios. In high additive noise cases (<10 dB SNR), the Kalman smoother based inverse performs similarly to that of group sparsity; however in the abnormal case, LASSO performs slightly better than the Kalman smoother.

Fig 1.7 shows the correlation coefficients and RMSEs for all methods at each point along the geometric line in space, for both normal and abnormal simulations, at 10dB SNR. Again, group sparsity has higher correlations and lower errors in both cases. As can be seen in Fig 1.4, the normal simulation increases in signal amplitude in the distal stomach. The ability to resolve signals in the distal stomach is likely a combination of both the closer proximity to the abdominal

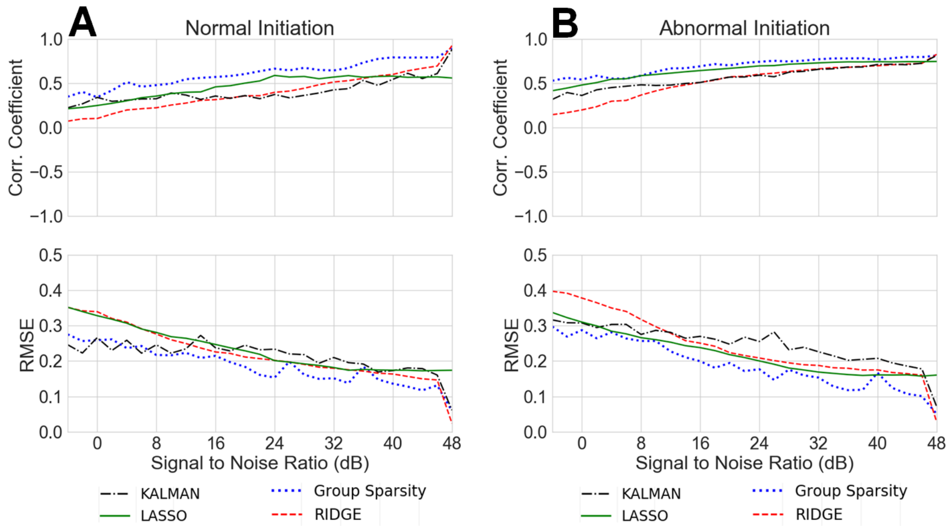

Figure 1.6: **Average Correlation Coefficient and RMSE for Different Noise Levels (All Methods)** A) Normal simulation inverse results average correlation coefficient and RMSE as a function of AWGN noise level, B) Abnormal simulation inverse results average correlation coefficient and RMSE as a function of AWGN noise level

surface and the increased signal strength. Specifically, our forward model given by eq (1.4) encodes the body conductivity and the distance between source and sensor points and indicates that sources of the stomach with same amplitude that are closer to the abdominal surface will go through less attenuation. The ability to better resolve signals across the entirety of the stomach in the abnormal simulation is most likely due to the constant signal power in the underlying simulation.

Fig 1.8 shows the localization results (electrical potentials) mapped back to the geometry for the 10 dB noise level, at 6 seconds into the simulation, in both normal and abnormal cases. The group sparsity method is the only one that resolves the two near wavefronts in the distal stomach, and it is also the only method that can resolve both the activity near the distal stomach and near the proximal stomach simultaneously. The ability of the group sparsity method to resolve near wavefronts and activity across the entirety of the stomach suggests that the joint assumptions of sparsity and smoothness, that it exploits, are critical for reconstruction of the underlying time-evolving gastric electrical activity.

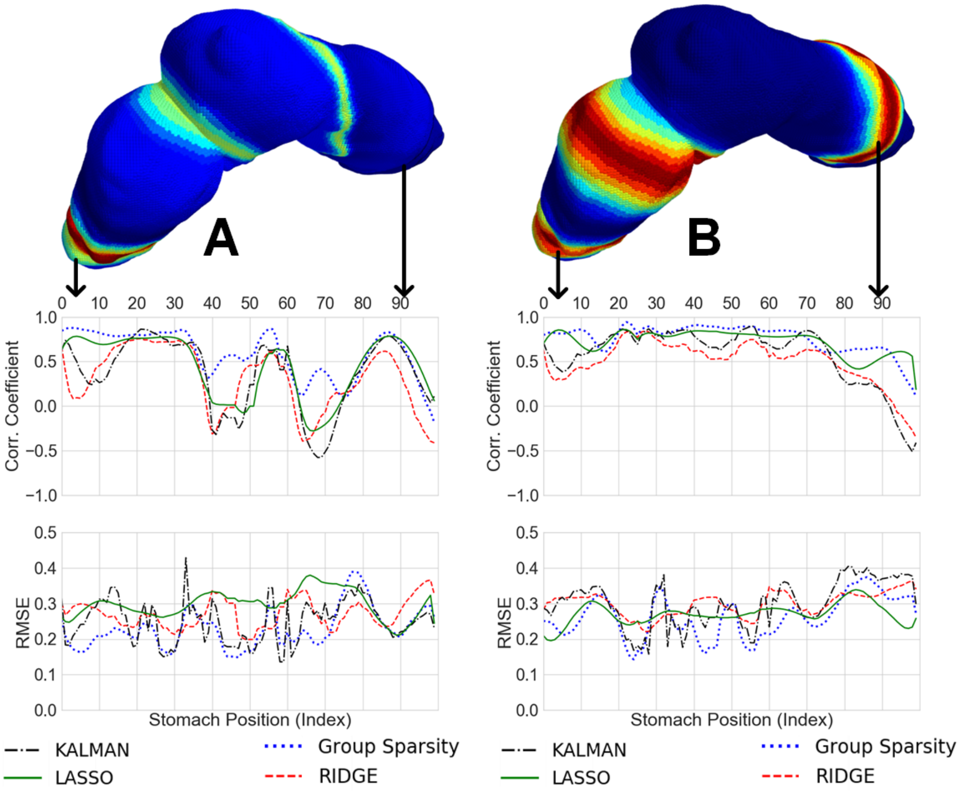

Figure 1.7: **Average Correlation Coefficient and RMSE for the 10 dB Noise Level Across Geometry (All Methods)** A) Normal simulation inverse results average correlation coefficient and RMSE as a function of geometry, B) Abnormal simulation inverse results average correlation coefficient and RMSE as a function of geometry

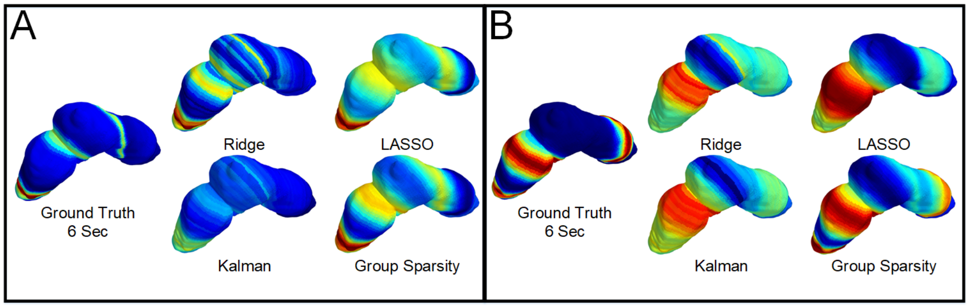

Figure 1.8: **Time Snapshot of the Inverse Results Mapped Back to Geometry** A) Normal simulation at the 10 dB SNR level at the 6 Second time point. B) Abnormal simulation at the 10 dB SNR level and the 6 second time point

Region-Specific Analyses of Simulated Data

We split the stomach into four sections (proximal 1, proximal 2, distal 1, and distal 2) so that spatial wave propagation parameters can be found in a region-specific manner (see Fig 1.2C).

We analyzed the PGD in each of those regions over time, and found the percentages of time, per region, in which $PGD_{\mathcal{R}}(t) > 0.5$. See Table 1.1.

Table 1.1: **Percentage of time that PGD $>$ 0.5 for Inverse Results Via Simulation Type and Region**

Data Source	**Proximal 1**	**Proximal 2**	**Distal 1**	**Distal 2**
Normal Simulation	45.7	59.3	82.3	99.0
Abnormal Simulation	60.7	80.6	75	72.3
Noise Alone Simulation	0.0	0.0	1.67	0.0

Table notes: For the normal simulation, the PGD percentage increases from the proximal to the distal stomach locations. In the abnormal simulation the PGD percentage remains highest in the second proximal and first distal regions, where we detect strong retrograde wave activity. As expected, the noise alone results show no statistically significant wave propagation.

A byproduct of the PGD processing is direction information (anterograde or retrograde) at each point along the organoaxial curve and at each point in time. Fig 1.9 B and C showcases region-specific histograms of anterograde vs retrograde propagation whenever $PGD_{\mathcal{R}}(t) > 0.5$, for both normal and abnormal simulations. As expected, the normal results have few retrograde waves in each of the four regions, and the abnormal results showcase a large majority of retrograde waves for all regions except distal 2 (where the wave initiation began). In distal 2, a majority of the waves operate in anterograde fashion, as shown by Fig 1.2. Note that in the abnormal simulation, the signal amplitude remained constant across time, whereas in the normative simulation the signal amplitude varied between the proximal and distal sections of the stomach (see Fig 1.3). This may explain why the PGD percentages in the proximal sections are higher for the abnormal simulation. More importantly, these results showcase our ability to find the correct direction of propagation in the proximal regions for both retrograde and anterograde, and owing to the large PGD percentages in both contexts, we have confidence that we can determine these directions for a large fraction of the recording.

Human Subject Recording

We applied the group sparsity method to a two-minute window of data collected from two human subjects. Both subjects had the same clinical description of motor function, specifically severely delayed gastric emptying in the absence of a mechanical obstruction (severe gastroparesis) with 30% of radiotracer label still in the stomach at 4 hours during a gastric emptying study. Whereas the first subject was diabetic, the most common known cause of gastroparesis due to possible damage of the vagus nerve or enteric nerve cells [50], the second subject was idiopathic, with no known reason for the severe delay in gastric emptying [51].

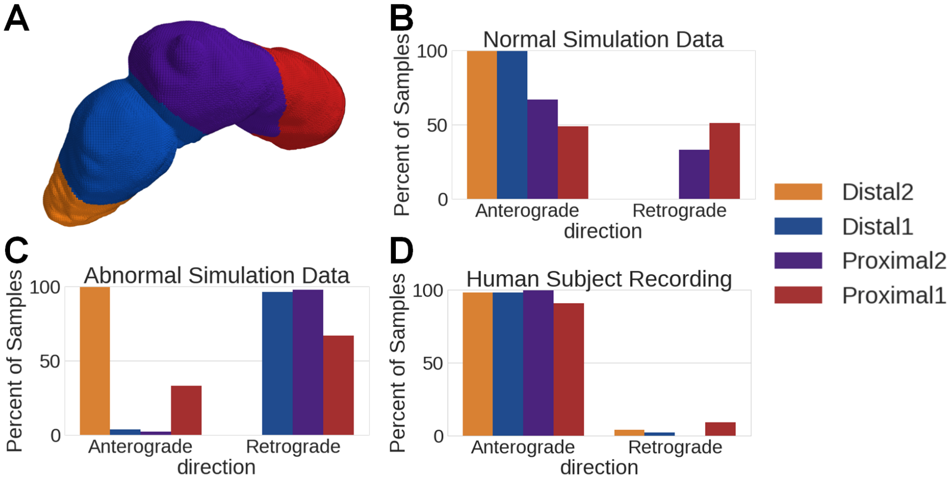

Figure 1.9: **Wave Direction Histogram by Stomach Region, for Time Points in Which PGD $>$ 0.5** A) Color coded stomach regions B) Normal data wave directions show strong anterograde wave propagation in all segments of the stomach. C) Abnormal data wave directions show strong retrograde wave propagation in the first distal and all proximal segments, while we see strong anterograde propagation in the distal 2 segment. This aligns with the simulation patterns. D) Human subject data wave directions show anterograde wave movement across all segments of the stomach, the strongest region being the distal 2 segment.

While we do not have ground truth on which to compare the results, the group sparsity method clearly resolves wave activity on the surface of the stomachs, as can be shown in Fig 1.10 for subject 1. This presence of sustained wave activity is confirmed quantitatively for both subjects in Table 1.2, which indicates the percentage of time for which a statistically significant wave is present (specifically, $PGD_{\mathcal{R}}(t) > 0.5$ for one second).

Table 1.2: **Percentage of PGD > 0.5 for Inverse Results on Human Recording and Region**

Data Source	Proximal 1	Proximal 2	Distal 1	Distal 2
Subject 1	17.9	33.7	42.5	97.5
Subject 2	24.6	92.1	7.9	95.6

In human subject 1, all areas of the stomach showed wave propagation, with the distal 2 section showcasing propagation during a significant percentage of the processed data set. The second subject shows strongest activity in the distal 2 segment and the proximal 2 segment. Also of note is that there is very little detected propagation in the distal 1 segment of subject 2, which may be due to the curvature of this particular stomach, as is seen in S7 Fig in the supplemental materials, versus that of subject 1 Fig 1.9. Differences in stomach geometry and stomach region proximity to the cutaneous surface are likely explanations for the percentages shown in Table 1.2. S8 and S9 Figs in supplemental materials show the localization results on the stomach geometry of the two human subjects.

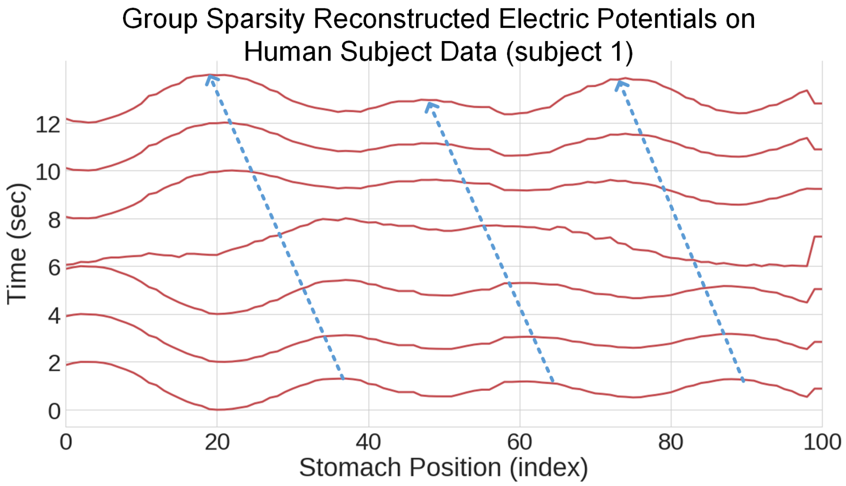

Figure 1.10: **Inverse Solution for Human Subject Data** As with the simulated data, this represents twelve seconds of computed inverse data across the sources on the organoaxial curve

For subject 1, as shown in Fig 1.9D, almost all waves with PGD > 0.5 contain anterograde propagation, strongly suggesting that this control subject does not have abnormal myoelectric function. We also implemented the group sparsity method on white Gaussian noise to verify that our estimation results were not due to chance. As shown in Table 1.1, the percentage of time for which PGD>0.5 for the white Gaussian noise simulation is 1.67% in the distal 1 segment and zero everywhere else. See S4 Fig in the supplemental materials for the reconstructed electrical potentials for the noise alone output.

Discussion

Simulation Results

Our work provides a novel application of Bayesian methods for spatiotemporal analysis to source localize the gastric slow wave. By exploiting the commonly used assumption of equipotentials along the bands of the organoaxial curve, we were able to parameterize the problem more succinctly (e.g. searching for optimal weights on an over-complete basis). These methods are however generalized, relying only on the relative positions in space of the sources and the sensors, the relationship between the source signal and the sensors (the forward model), and the basis representation. The key assumptions we make with our group sparsity prior are that there are only a few bands of stomach are electrically active at any point in time, and that the electrical activity will evolve smoothly in time. Our method requires knowledge of the stomach and abdominal positioning in 3D space, but otherwise the method is agnostic to specific geometry. To this point, we include an additional human subject for which we developed a model with their CT and applied analogous normal and abnormal simulations for which we evaluated the performance of the group sparsity estimator. For this second subject, we also implemented the group sparsity method on an HR-EGG recorded data segment from the post-prandial segment of data. The results are presented in the supplemental materials (see S5, S6, and S7 Figs). As with the first subject, this method is able to reconstruct wave activity in all segments of the gastric surface and resolve the two nearby wave fronts that appear in the distal 2 segment of the gastric surface in the disordered simulation.

Only recently have computationally efficient approaches that combine sparsity constraints and linear state space dynamics been applied to the more richly studied EEG source localization problem [52]. As such, our approach, which combines sparsity with state space modeling, has the potential to be utilized in modern source localization problems for EEG research and beyond.

Previous studies [31] focused primarily on generic physical models of both the torso and the stomach. In this study, the torso and stomach models are taken directly from CT scans of a human subject, and as a result the relationship between the torso (electrode positions) and the stomach in geometry is more akin to a real subject recording. As a result of this, we also see that the methods are better able to reconstruct wavefronts in different regions of the stomach.

Table 1.1 indicates that for subject 1, the distal segments of the stomach showcase the strongest recovery of wave activity in the normative simulation. Further, Fig 1.7 showcases that the distal regions have comparatively superior reconstruction performance. This may in part be explained by the fact that for the normative simulation, in accordance with known physiology [35], the signal is stronger in the distal segments of the stomach. This may also be explained by the fact that the anatomical CT for subject 1 shows that the distal segment is closer physically to the abdominal surface. Specifically, by virtue of the denominator of eq (1.4), this implies that, absent of considerations of source amplitude, the stomach region closest to the abdominal array (distal 2) more strongly contributes to the HR-EGG.

For the abnormal initiation simulation, we are more able to consistently reconstruct wavefronts across all regions of the stomach, as shown by Table 1.1. This is likely due to the fact that the wave has consistent signal power, at the same magnitude of the antrum signal power of the normative simulation, across all regions.

For subject 2, the simulated signal activity for the normative simulation still has highest strength signal activity in the antrum. However, the stomach geometry is different from that of subject 1, in particular with more curvature through the proximal and distal segments of the stomach (see S8 and S9 Figs in the supplement).

S1 Table of the supplemental materials indicates that the proximal 2 segment showed stronger wave activity (75.3%) than the distal 1 segment (64.3%). This suggests that the larger amplitude in the distal 1 region as compared to the proximal 2 region was possibly counterbalanced by the increase in curvature of the stomach, giving rise to variations in the numerator of eq (1.4), as compared to subject 1.

We found that across noise levels and simulated conditions in subject 1, the group sparsity approach results in lower squared errors and higher correlation coefficients than the other methods explored. For the abnormal initiation scenario, in low SNR cases the LASSO slightly outperforms the Kalman smoother, and for the normal scenario this is reversed. For abnormal initiation scenario the assumptions about sparsity are perhaps more important than smoothness. However, because the group sparsity approach showed superior performance against all other models (in terms of both mean squared error and correlation coefficient) in all scenarios, it implies that the assumptions of both time smoothness coupled with spatial sparsity are critical. This is further evidenced by the uniqueness of the group sparsity method in separating the close wavefronts during the abnormal initiation, as shown in Fig 1.5 and Fig 1.8. It was due to these results that we focused solely on the group sparsity method for subject 2.

These results represent a critical step forward towards objective non-invasive inverse measures for gastric health. While Bayesian inference has been used in EEG and EKG inverse studies, our novel approach aggregates assumptions of spatial sparsity and temporal smoothness into one prior distribution and thus one penalty. Compared to the classic methods, this method shows significant and uniform improvement, thus compelling us to solely use this method when analyzing human subject data.

Human Data and Clinical Implications

In the human subject recording, we found that after applying our inverse procedure, not only can we identify wave propagation, but we are also able to determine region specific propagation patterns that are consistent with what is known about stomach anatomy and physiology. In the recording for subject 2 who is diagnosed with idiopathic gastroparesis we observe significant and strong retrograde propagation in the proximal regions, as evidenced by 92.1% detected wave activity from Table 1.2 as well as 100% retrograde activity found in the proximal 2 region (S7 Fig of supplemental materials). This differs from subject 1, who had robust wave detection and anterograde activity in all regions (Fig 1.9). This subject was also involved in a recent clinical study that used the HR-EGG to identify cutaneous spatial patterns [22]. The spatial patterns we found using our inverse method on the gastric surface are consistent with the spatial patterns found on cutaneous HR-EGG analyses from [22]. Specifically, in the inverse method we find anterograde activity in all segments, which aligns with the spatial histogram from cutaneous HR-EGG found in Fig GP-15 in the supplemental materials of [22]. The spatial abnormalities in subject 2 are consistent with findings of loss of ICC cells in idiopathic gastroparesis patients [53], which is known to contribute to gastric myoelectric spatial abnormalities. [12]. That there were more detected spatial abnormalities in an idiopathic gastroparesis subject as compared to a diabetic gastroparesis subject can perhaps be explained by findings of more severe ultra-structural changes in ICC cells and nerves idiopathic gastroparesis patients as compared to patients with diabetic gastroparesis [54].

Understanding the relationship between myoelectric activity in different parts of the stomach can allow for sub-typing of gastric disorders. For instance, antrum and pylorus coordination or lack thereof can help predict (and thus explain) gastric emptying of meals in humans [55]. As such, being able to non-invasively extract myoelectric patterns in stomach sub-types, and evaluate their coordination, can give rise to etiologies of certain GI disorders and suggest therapies. It was recently shown that spatial features from the cutaneous HR-EGG correlate with symptom severity [22]. As such, our approach to identify spatial slow wave abnormalities (such as abnormal initiations discussed here), in region-specific manners, may advance the potential to enable guided therapies, such as ablation [56] or gastric pacing [57, 58] to normalize the slow wave and ameliorate symptoms.

One existing therapy, high frequency gastric electrical stimulation, has been shown to improve symptoms by affecting central control of nausea and vomiting [59]. Moreover, features from invasive electrical recordings on the stomach surface predict which patients respond well to this therapy [15]. This suggests that if this information could be extracted non-invasively, new opportunities exist to phenotype such disorders and assess their response to interventions. In addition, recent efforts to directly modulate gastric electrical activity with an artificial pacemaker have the potential to improve gastric function [60, 61]. However, determining the stimulation location and parameters and confirming the restoration of normal electrical activity requires invasive measurements [62]. Our noninvasive approach could guide these types of targeted therapies for gastric disorders, as has been done successfully in cardiology with identifying and treating arrhythmias [63, 64].

Limitations and Future Research

The gastric slow wave is normally active at all times, but triggers more contractions when co-regulatory factors (such as stretch from food ingestion) are present. This initial work used a straight forward dynamic model which did not account for volume changes and region-specific deformations due to food or deformation due to contractions [65, 66]. Further, the increase in contractions due to eating may give rise to stronger electrophysiologic potentials, which was not modeled here. These aspects could be incorporated into both the forward model and the prior for future studies.

There are two further approaches to extend this model. For one, our forward model assumes a homogeneous space with the same conductivity to relate the gastric surface potentials to the recorded abdominal potentials. In reality, there are tissues with different conductivities (e.g. fat and muscle) between the stomach and abdominal surface. Using models that capture this information can be done in future work. Further, our model uses simple one-dimensional wave equation propagation models to represent the spatiotemporal relationship of the gastric electrical activity. Future work can take into consideration cellular compartment models with differential equations, as has been done in other EGG modeling works [67–69]. Validation of these methods using abdominal recordings from a larger group of asymptomatic human subjects as well as those with diagnosed disorders may further give credence to this approach. Lastly, selecting regularization coefficients in a data-dependent manner when using model-fitting procedures that leverage sparsity is a subject for future work [70, 71].

Conclusion

In this paper, we used CT images from human subjects to develop a basic dynamic dipole model of the electrical activity on the surface of the stomach (the gastric slow wave). We solved a forward model, then corrupted with additive Gaussian noise, to simulate cutaneous multi-electrode recordings. Using these simulated observations, we found the inverse solution by formulating the inverse problem as a MAP estimation problem to find a set of optimal weights on a set of spatial Fourier basis functions. Each method we explored leveraged different assumptions about smoothness (Kalman smoother), sparsity (LASSO), a combination of the two (group sparsity), and no assumptions at all (Tikhonov regularization). We found that in low to no noise environments, Tikhonov regularization is sufficient. However, in noisier environments, the assumptions around smoothness have the most impact and result in lower RMSE and higher correlation coefficients. Additionally, by incorporating a prior distribution for which the MAP estimate takes advantage of both smoothness and sparsity (the group sparsity approach), the results are even further improved. These results uniformly attained the highest performance, for both abnormal simulations as well as normal simulations.

Finally, we applied this approach to an asymptomatic human subject who had previously been imaged with CT. We found statistically significant results for wave activity, as well as region specific wave direction information that is consistent with current knowledge regarding normal gastric myoelectric function [11]. The presented methods may benefit from further studies and validation on mammalian subjects against invasive "gold-standard" methods. While further research is needed to verify this approach on more human subject data against a secondary measure of electrical activity on the stomach surface, these initial results show significant promise towards utilizing a non-invasive technique to localize electrical activity in different regions of the stomach, possibly even in ambulatory settings [30].

Acknowledgments

Chapter 1, in full, is a reprint of the material as it appears in PLOS ONE, October 2019. Alexis B. Allegra, Armen A. Gharibans, Gabriel E. Schamberg, David C. Kunkel, Todd P. Coleman, 2019. The dissertation author was the primary investigator and author of this paper.

Chapter 2

Automated Model Selection Procedures for The Source Localization of the Gastric Slow Wave

Introduction

The neuromuscular function of the gastrointestinal (GI) system involves smooth muscle cells which are controlled with rhythmically oscillating pacemaker cells - the interstitial cells of cajal (ICC) [11]. The spatio-temporal coordination of these cells enables the peristalsis which propels food through the GI tract [10, 11]. Generally, the gastric ICCs oscillate at 3 cycles per minute (0.05Hz) and in normal activity initiate a slow wave which propagates in an anterograde direction from the top of the greater curvature of the stomach towards the small intestines. Nuromuscular dysfunction make up more than half of disorders in the GI system. The two most common upper GI disorders are functional dyspepsia (FD) with a prevalence of 10% and gastroparesis (GP) 1.5-3% [3, 72, 73]. Additionally GP, delayed gastric emptying in the absence of mechanical obstruction, is present in 70% of Parkinsons patients [3] and 50% of diabetes patients [4]. Non-invasive diagnosis of GI abnormalities generally relies on either subjective symptom-based questionnaires and assessment or objective measures such as gastric emptying that do not consistently correlate with symptom severity [5]. Further while there are multiple medications are on the market that improve gastric emptying they do not always improve symptoms, or they improve symptoms but not gastric emptying time [7–9]

One approach to the disambiguation of disease etiology, tracking disease progression, and predicting treatment response is to non-invasively characterise the gastric slow wave. Electrogastrography (EGG) is a technique similar to that of electrocardiography for the heart, to assess gastric myoelectrical activity using cutaneous electrodes [17]. While it is easy to administer and non-invasive conventional EGG relies on a small number of electrodes and exclusively extracts spectral information [18]. Additionally it has been shown that spatial abnormalities can occur at normal frequencies and thus go undetected [19]. The high resolution electrogastrogram (HR-EGG) [21], is similar to an electroencephalogram (EEG) for the brain, multi-electrode arrays are placed on the abdominal surface in line with the stomach (often guided by CT or MRI scans).

These recordings allow for the extraction of abdominal wave propagation parameters at each time point. Furthermore the extracted propagation parameters have been shown to correlate with symptom severity in a population of GI patients that span a wide range of BMI, ages, and disease etiology [22]. However, the HR-EGG extracts spatial information relative to the cutaneous surface and the HR-EGG voltages measured are an average of the electrical sources on the gastric surface due to volume conduction. Additionally, it has been shown that anterograde or retrograde waves from one or more sources can arise at the same time in the distal stomach [12, 13, 23]. The HR-EGG cannot disambiguate between regions of the stomach (e.g. the pacemaker vs the greater curvature or distal stomach).

In order to address this limitation, in our previous work [74] we developed inverse methods to infer spatiotemporal electrical patterns on the surface of the stomach from multi-electrode recordings used in HR-EGG. Fundamentally the problem of non-invasively source localizing the gastric slow wave is considered ill-posed, as the number of potential sources to be recovered greatly exceeds the number of observations on the cutaneous surface, and there are infinitely many solutions which are equally consistent with the data. To address this we leveraged Bayesian inference in which a prior distribution is specified that enforces a unique solution to a regularized model fitting problem. The most robust method we found was MAP estimation with a group sparse prior that encourages sparsity as well as time smoothness in the spatial wave dynamics, which is consistent with physiologic findings [11]. With the group sparsity method, we found that we were able to disambiguate wave propagation direction in four separate regions of the stomach, and identify statistically significant wave activity in each region. This method, however, was not fully automated and thus could not be applied to large scale data collection.

Here we consider a fully automated approach for the group sparsity method that leverages the Pareto frontier to automate the model selection process. In addition, we consider an approach that separates the group sparsity (GS) methodology into two stages. The first stage enforces spatial sparsity by using the least absolute shrinkage operator (LASSO), the second stage enforces temporal smoothness with the Kalman smoother. We then leverage two model selection techniques, the Pareto frontier, and the penalized normalized negative log likelihood (PNNLL) to identify solutions of interest. For the Lasso-Kalman smoother (LKS) approach we still require manual intervention to identify the final solution in the PNNLL curve.

Both the GS and LKS find statistically significant wave activity in each of the gastric regions across seven human subject models for which HR-EGG recordings were available. Three of these subjects are healthy controls, and four are unhealthy, diagnosed gastroparesis with different underlying disease etiologies. Further these subjects range in BMI from from 21.8 to 31.5. Whereas the LKS approach is more computationally efficient and demonstrates larger correlation coefficients with the ground truth in simulation, the GS approach is less susceptible to false positives for spatial wave propagation and finds statistically significant decrease in wave activity in patients with diagnosed GI disorders as compared to healthy controls. In addition, a regression analysis finds that the correlation coefficient between the GS solution and ground truth is invariant to a wide range of gastric lengths, suggesting it is robust to a variety of stomach sizes and geometries. Altogether given these findings and the fact that the GS method is fully automated, this provides an important step towards the development of clinical non-invasive techniques to characterize the specifics of gastric neuromuscular abnormalities and provide specific avenues to explore treatment.

This paper is organized as follows, Section 2 describes the modeling and simulation required for the problem as a whole, including the 3D models, the dynamic simulation development, and the observational model. Section 2 presents MAP estimation and our Bayesian inference approach. The different model selection techniques (the Pareto frontier and the PNNLL) are discussed in Section 2. In Section 2 we present analysis methods for extracting wave information and determining statistical significance. We then describe the subject recordings. Section 2 provides group level results (simulation and subject recording for all subjects). Lastly, Section 2 and Section 2 provide discussion and conclusion, respectively.

Modeling and Simulation

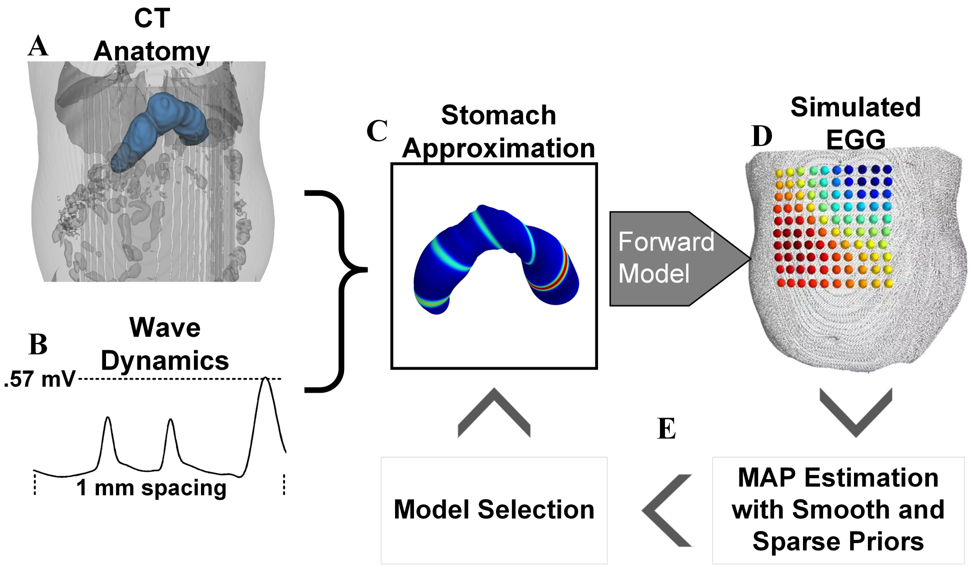

Figure 2.1: **General Process** A) Stomach models extracted from Subject CT B) 1-D wave equation generated wave dynamics specific to the subject anatomy C). The stomach model is approximated as rings in 3D space, 1mm apart D) A forward model is solved to generate a simulated EGG observation E) Apply a MAP estimation technique with model selection to identify the recovered sources.

In this study, we use the simulations and models previously developed [74] to explore the ability to identify optimal solutions to ill-conditioned inverse problems in a data-dependent manner. We first extract the three dimensional (3D) models for both the stomach and the abdomen from magnetic resonance imaging (MRI) or computed tomography (CT) scans. We use finite differences to solve a 1-dimensional (1D) wave equation that captures the electro-physiologic dynamics of the gastric slow wave (both normal and abnormal simulations). To map the dynamic electro-physiological simulations to the 3D stomach model, the 3D model is sliced along planes normal to a curve along the stomach surface (the organoaxial curve), in variance to our previous approach each slice is simplified to a circular ring in 3D space (fig. 2.2. Mapping the stomach simulation to the abdominal surface is done with a simplified forward model in which we assume the gastric surface and the abdominal surface exist in the same homogeneous volume, with constant conductivity. To the resulting simulated observation array on the abdominal surface we inject additive white Gaussian noise (AWGN) and then apply Bayesian inference techniques to solve the inverse problem. Finally, we apply model selection to identify the optimal solution from the set of possible solutions.

3D Static Models

As in our previous work [74] we use 3D Slicer, an open source medical imaging tool to extract stomach and abdominal models from MRI and CT scans of participating subjects [33]. 3D slicer provides the key ability to fit equi-spaced curves to arbitrary geometry. Four fiducial curves were drawn on each subjects gastric surface and the points forming the organoaxial curve were set to a 1mm inter-point spacing. Previously a fixed number of points (120) were used for the two subjects studied. The variability in stomach size and shape across a larger subject population necessitated the use of uniform point spacing on the organoaxial curve, with different numbers of points for each subject. As a result, the dynamic simulations were customized to each subject. Using these four fiducial lines, planes normal to the stomach, containing the organoaxial curve,

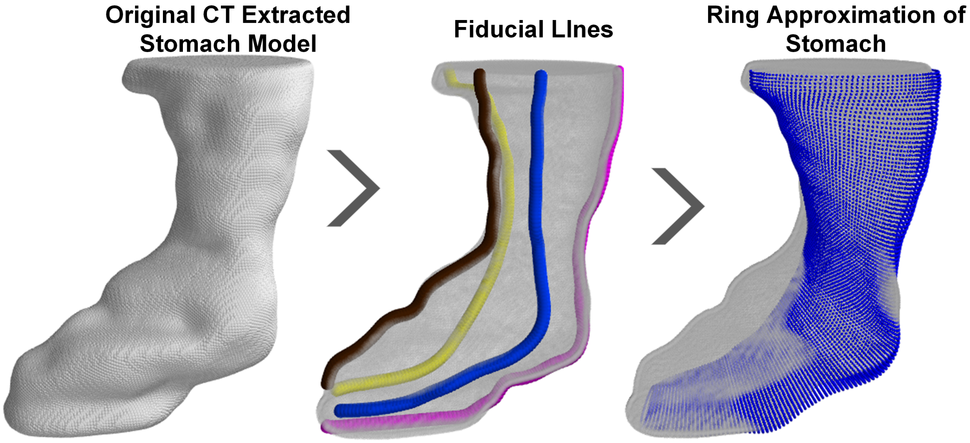

Figure 2.2: **Ring Approximation of the Stomach** Using four fiducial lines on the gastric surface the stomach is sliced along the planes normal to the organoaxial curve and rings of variable radius are computed at each point. These rings form the ring approximation of the gastric surface.

were derived. Circular rings were computed from the center point of each plane, whose radius varies with the geometry of the stomach (see Supplementary Materials for the 3D models of each of the 7 subjects studied). The 1-D wave equation solution was then mapped to each ring as a function of time sample to represent the electro-physiological behavior of a normative stomach activating in equi-potential rings.

1-D Dynamic Simulation

Similar to the heart, the gastric slow wave begins with activation of a group of pacemaker cells normally on the upper part of the greater curvature of the stomach [35]. The electrical signal from these cells spreads isotropically through activation of a network of interstitial cells of cajal (ICC). The ICCs initiate muscular contraction through the corpus and antrum with typically no more than 5 wavefronts occurring at any point in time on the stomach surface.

The gastric slow wave is characterized by its continuous nature and strong wave-like propagation patterns. As in our previous study, we used a finite difference approach with Mur's boundary condition to solve a 1-D wave equation [21]. We simulate a normal slow wave in which the wave activity begins in the proximal stomach (near the fundus) and propagates in an anterograde fashion to the distal stomach (near the antrum). Consistent with invasive findings [12], we also simulate the abnormal simulation in which the gastric wave is initiated near the distal stomach and propagates in both a retrograde and anterograde fashion.

In our previous study, we solved the wave equation on a grid of 100 points equispaced along the organoaxial curve surface. Here, each subjects simulation was still solved on the organoaxial curve but the number of points are dictated by the length of the organoaxial curve. Points were equispaced at 1 mm apart along the curve. Parameters for pulse width, speed and amplitude were chosen to be consistent with recent descriptions of healthy subjects [35–37]. Speed and amplitude are highest in the proximal region (6.0 mm/s, 0.57 mV), reduced in the central stomach (3.0 mm/s, 0.25 mV), and increased again in the distal stomach near the antrum

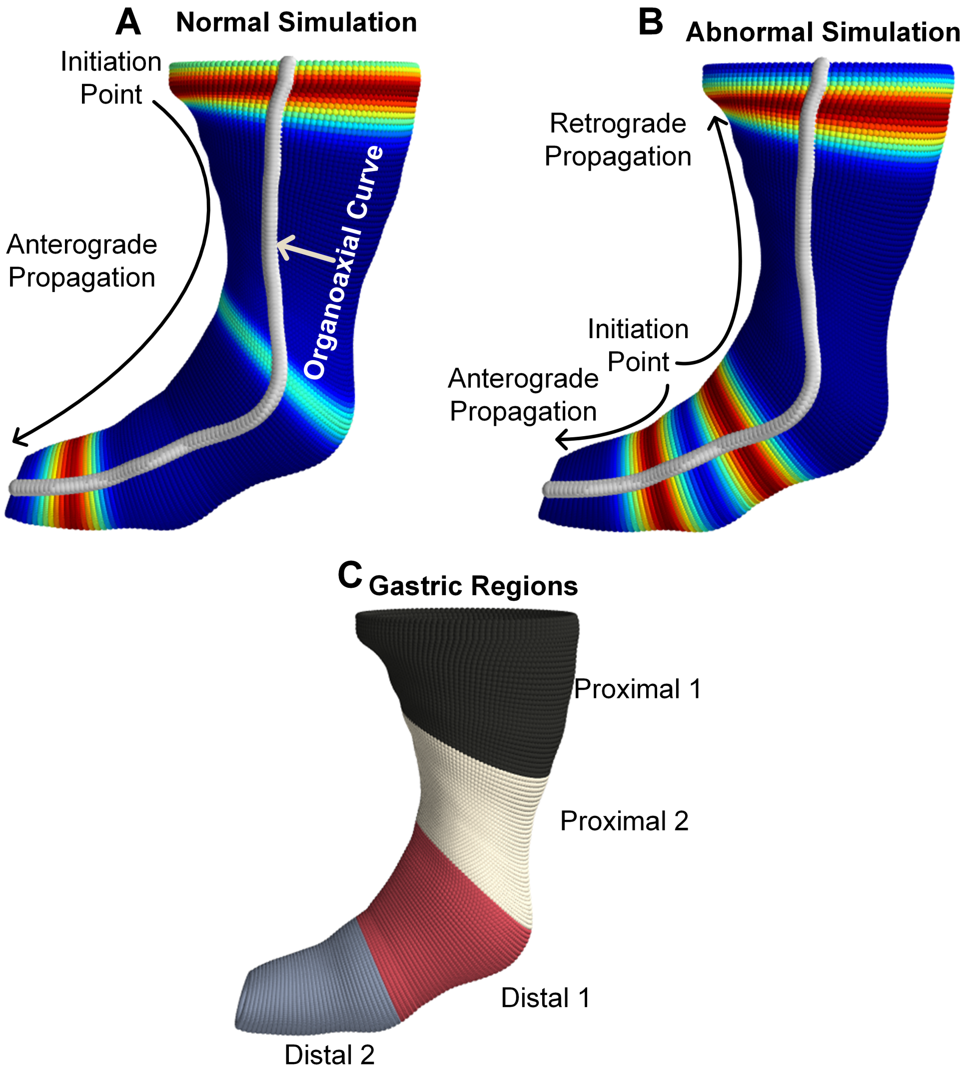

Figure 2.3: **Dynamic Simulation and Gastric Regions**A) Normal simulation mapped to the ring gastric approximation.]Initiation begins before the proximal 1 region and propagates in an anterograde fashion towards the distal regions. B) Abnormal simulation mapped to the ring approximation, the wave initiates in between the two distal segments and propagates in two directions, anterograde through the distal 1 segment and retrograde through the distal 2 and proximal segments. C) Separation of the gastric surface into four regions of interest

(5.9 mm/s, 0.52 mV). For the abnormal simulation the speed and amplitude of the wave remain constant (6.0 mm/s, 0.57 mV) across the entire gastric surface. As visualized in B) of Fig. 2.3 the abnormal wave initiates in the first distal region and splits with one part of the wave propagating in a retrograde fashion towards the proximal stomach and the other part propagating in an anterograde fashion towards the antrum.

Observation Generation

Using 3D Slicer [33] we placed fiducial markers on the 3D abdominal models according to the placement notes at the time of HR-EGG recording. For each subject, a 10 by 10 grid of abdominal fiducial points was generated, spaced 2 cm apart. The averaging effects of the electrodes were simulated by solving the forward model in a 1 cm radius region around each of the fiducial points selected and averaging the result to generate the simulated observation data $Y \in \mathbb{R}^{N \times T}$ where N is the number of electrodes and T is the number of time samples. For each subject, N is a 10 x 10 grid and T is 180 time samples, with a sampling rate of at 1 sample per second. The EGG signal at each electrode [39] is

$$y_n(t) = \sum_{i=1}^{D} A_{n,i} x_i(t) + N_n(t). \tag{2.1}$$

where $y_n(t)$ is the signal at each of the N electrodes, $A_{n,i}$ is the simplified forward model matrix, $x_i(t)$ is the surface potential at each of the D gastric source locations and instant in time, and $N_n(t)$ is AWGN of adjustable variance σ^2 to achieve 3 dB and 50 dB signal to noise ratios (SNR). The same σ^2 is used for each electrode to generate a per-electrode realization of AWGN [39].

The simplified current dipole [38] based forward model arises from the assumption that the gastric surface and the abdominal surface are in the same homogeneous volume of constant conductance. The forward model reduces to a linear attenuation constant which relies only on the position of the stomach sources and abdominal sensors.

$$A_{n,i} = \frac{cos\theta}{4\pi\sigma r_{n,i}^2}. \tag{2.2}$$

where θ is the angle between the organoaxially oriented current dipole and the observation point on the abdominal medium, σ is the constant tissue conductivity, and r is the straight line distance between the *i*th gastric source and the *n*th abdominal sensor [38].

Source Localization

Due to the ill-conditioned nature of this inverse problem, we leverage the electrophysiologic characteristics of the gastric slow wave: it contains bands of electrical activity that continuously propagate along an organoaxial curve in rings of equipotential [11]. The continuous spatial nature of this activity lends itself to representation by a set of spatial basis functions. We use a Fourier spatial basis and solve the problem only on the 1-dimensional organoaxial curve.

Basis Representation

As with the previous study [74], we represent the spatiotemporal activity of the surface potentials as a weighted combination of spatial Fourier basis functions. These functions are time invariant, but the coefficients on them evolve over time. The different sinusoids in the spatial basis represent different spatial frequencies (number of wavefronts per unit space) along the 1 dimensional organoaxial curve. A detailed description of the basis matrix formulation is in [74] equation 5 and 6.

With this basis representation the sources are modeled as:

$$\overrightarrow{x}(t) = H^T \overrightarrow{w}(t). \tag{2.3}$$

where H^T is the D x K basis matrix and $\overrightarrow{w}(t)$ is the vector containing the K time evolving weights. The measurement model becomes:

$$y_n(t) = \sum_{i=1}^{D} A_{n,i} \sum_{k=1}^{K} h_{d,k} w_k(t) + N_n(t) \tag{2.4}$$

where $h_{d,k}$ is the index into the basis matrix and $w_k(t)$ is the kth weight. (2.4) simplifies in matrix notation to:

$$\overrightarrow{Y}(t) = AH^T \overrightarrow{w}(t) + \overrightarrow{N}(t) \tag{2.5}$$

This formulation limits the problem to one of solving for the K weights instead of the total number of possible gastric sources.

MAP Estimation

The measurement model in (2.4) encodes the statistical model $p(Y|W)$. As in [74], we interpret the source localization problem as one of finding the Bayes optimal point estimate of the time series of weights. In other words, our goal is to maximize $p(W|Y)$ over W for any set of measurements Y. This Bayesian approach leverages both the measurement model $p(Y|W)$ as well as the prior distribution $p(W)$ to identify an optimal solution. Since the likelihood $p(Y|W)$ is governed by the forward model and an additive Gaussian noise model at the electrodes, the estimator is

$$\begin{aligned}\hat{W}_{MAP} = \underset{W \in \mathbb{R}^{K \times T}}{\arg\min} & \sum_{t=0}^{T-1} ||\overrightarrow{y}(t) - AH^T \overrightarrow{w}(t)||_2^2 \\ & + \lambda \text{pen}(W).\end{aligned} \tag{2.6}$$

where $\hat{W}_{MAP} = [\overrightarrow{w}(1), \overrightarrow{w}(2), \ldots, \overrightarrow{w}(T)]$ and $\text{pen}(W)$ corresponds to the negative log of the prior distribution on W. The source estimate at any time t is given by the maximum a posteriori (MAP) estimate: $\hat{\overrightarrow{x}}(t) = H^T \hat{\overrightarrow{w}}_{MAP}(t)$. In our previous study we found that a group sparsity regularization technique which encoded both spatial sparsity in the weights and time smoothness in the solutions yielded the best results (highest correlation coefficient) in the presence of variable levels of AWGN.

Group-Sparse Prior

In general, the group sparsity regularization technique promotes sparsity amongst groups of coefficients and imposes a penalty on the first differences of those coefficients. This results in a set of coefficients where only a sparse subset is non-zero at any point in time and this subset evolves smoothly over time. The penalty associated with this approach is:

$$\text{pen}(W) = \sum_{k=0}^{K-1} \left(\sum_{t=0}^{T-1} d_k(t)^2 \right)^{\frac{1}{2}} \tag{2.7}$$

where d represents the first differences in the time of weights:

$$\overrightarrow{d}(0) = \overrightarrow{w}(0) \tag{2.8}$$

$$\overrightarrow{d}(t) = \overrightarrow{w}(t) - \overrightarrow{w}(t-1), t = 1, \ldots, T-1. \tag{2.9}$$

This time evolving portion of the penalty is wrapped inside of an ℓ_1-norm and the penalty can be thought of as an ℓ_1-norm of an ℓ_2-norm of time differences. The sparsity-promoting ℓ_1-norm allows for a small number of non-zero weights and these non-zero weights will evolve smoothly in time. The estimated source potentials are thus composed of a small number of spatial frequency components which evolve continuously in time.

Previously, we found the group sparse prior [25] provided superior results when compared with techniques that leveraged either sparsity (LASSO) [41] or smoothness (Kalman Filter) [42] alone. On the flipside, it is computationally intensive and required manual selection of the MAP estimation hyper parameter (λ) to identify a solution. In the next two subsections, we describe an alternative spatially sparse and temporally smooth method to the group sparsity approach which we term the “LASSO-Kalman smoother” (LKS).

Active Set Identification for LASSO

Here we separated the problem into one of first finding active sets of sparse dominant weights by solving an ℓ_1 regularization problem with LASSO and then solving the problem again with the Kalman smoother on each one of these active sets to enforce time smoothness in the final solution. This approach allows for two data dependent techniques to be leveraged for hyper-parameter estimation: the Pareto frontier and the penalized negative normalized log likelihood (PNNLL) approach. To identify the active set of sparse dominant weights, we first solve the inference problem with the LASSO. The LASSO penalty for the MAP estimation is:

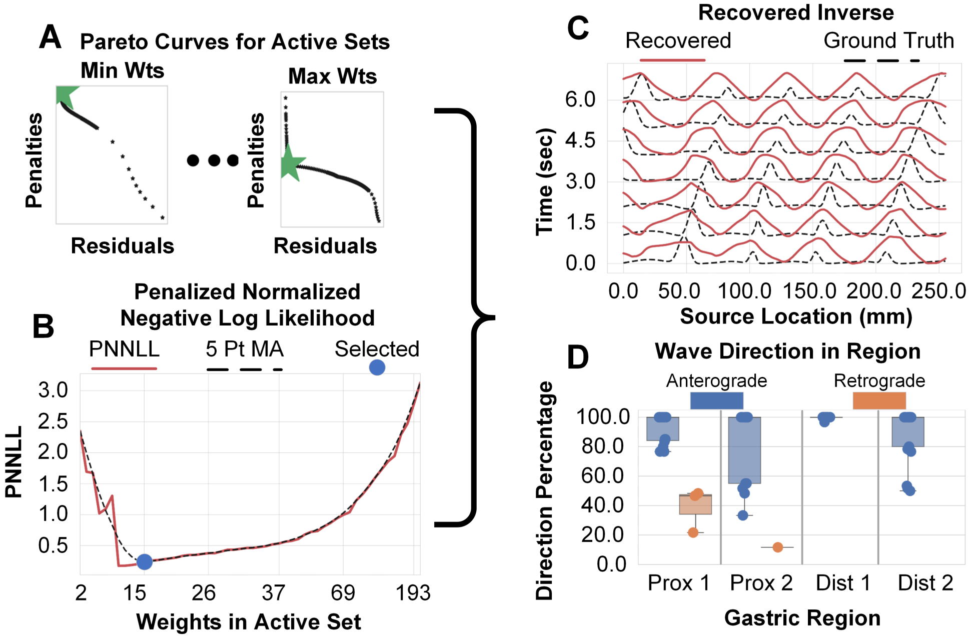

Figure 2.4: **Pareto Curve and PNNLL for Optimized Model Selection** A) The Pareto curve for the active sets with knee point identified B) The PNNLL computed from each knee point C). The recovered sources chosen from the transition point in the PNNLL D) The PGD analysis of the chosen solution.

$$\text{pen}(W) = \sum_{t=0}^{T-1} ||\vec{w}(t)||_1. \tag{2.10}$$

where the number of active weights increases with decreasing values of the hyper parameter λ. To identify different active sets from each value of λ, the energy in weights is computed using the norm of the value of the weights across time:

$$E_\lambda = ||\hat{W}_\lambda||_2^2. \tag{2.11}$$

Where $\hat{W}_\lambda$ is the solution to equation (2.6) with the penalty as (2.10), it is a K x T matrix. The weights whose energy is greater than zero form the active set for a given λ. Active sets are chosen such that the number of weights in the sets ranges from 1 weight to greater than 100 weights. We implement the LASSO with the scikit-learn Python package [44].

Kalman Smoother Operating on an Active Set

Once the groups of sparse weights are identified through LASSO, we reprocess the data with the Kalman Smoother using only those dominant weights found in each active set. The estimator is formulated as:

$$\begin{aligned} \hat{W}_{MAP} = \underset{W \in \mathbb{R}^{K \times T}}{\arg\min} & \sum_{t=0}^{T-1} ||\overrightarrow{y}(t) - A H_m^T \overrightarrow{w}(t)||_2^2 \\ & + \beta(||\overrightarrow{w}(0)||_2^2 + \sum_{t=0}^{T-1} ||\overrightarrow{w}(t) - \overrightarrow{w}(t-1)||_2^2). \end{aligned} \tag{2.12}$$

Here H_m^T is the active basis matrix whose rows correspond only to the weight indices in the active sets identified for each of the m LASSO λ's. At the end of the active set identification process and the Kalman smoothing process, there are m active sets by L Kalman solutions (for each of the L βs in the Kalman MAP estimation problem). We implement the Kalman smoother in Python with the pyKalman package [45].

Model Selection

To perform model selection, first we compute the Pareto frontier on the Kalman smoother solutions for each active set. This results in A possible solutions, where each A represents a solution that has an increasing number of weights (fig. 2.4, A). We then apply the penalized negative normalized log likelihood (PNNLL) procedure to choose the optimal active set and thus the optimal solution out of the entire set. We also apply the Pareto optimization technique to the group sparsity approach to compare the efficacy of the LKS approach.

Pareto Optimization

The Pareto frontier is a multi objective optimization approach in which we aim to find an acceptable solution from a set of potentially infinite solutions [75]. For a two objective minimization problem, the Pareto front will form a concave up curve where the optimal solution is at the point of greatest concave curvature [76]. Fig. 2.2 A shows examples of Pareto fronts. This L-shaped curve which is formed by plotting the log of the residual against the log of the penalty as indexed by the hyper parameter (the Kalman smoother β). In general, the residuals are monotonically increasing and the penalties are monotonically decreasing; the optimal point is the solution of maximum curvature and encompasses the tradeoff between these two metrics. To form this curve, we plot the log of the residual

$$R_m(t) = \sum_{t=0}^{T-1} ||\overrightarrow{y}(t) - AH_m^T \hat{\overrightarrow{w}}(t)||_2^2 \tag{2.13}$$

against the log of the penalty

$$P_m(t) = ||\hat{\overrightarrow{w}}(0)||_2^2 + \sum_{t=0}^{T-1} ||\hat{\overrightarrow{w}}(t) - \hat{\overrightarrow{w}}(t-1)||_2^2. \tag{2.14}$$

For group sparsity we plot the same residual (2.13) against the log of the group sparse penalty (2.7). For the LKS approach the residuals decrease and the penalties increase as a function of increasing hyper-parameter β, for the GS approach the opposite is true, residuals increase and penalties decrease with increasing hyper-parameter size.

To automatically identify the point of greatest curvature, we fit twice differentiable cubic splines to both the residual curve and the penalty curve. We treat these as parametric curves in t and use standard parametric calculus to compute the curvature as:

$$C_m(t) = \frac{R_m^{'}(t)P_m^{''}(t) - P_m^{'}(t)R_m{}''(t)}{(R_m'^2(t) + P_m'^2(t))^{\frac{3}{2}}}. \tag{2.15}$$

Where $R_m^{'}(t)$ and $P_m^{'}(t)$ represents the first derivative of the residual and penalty curve respectively and $R_m^{''}(t)$ and $P_m^{''}(t)$ represent the second derivatives. In order to find the greatest point of concave curvature, we apply a peak search algorithm to (2.15) and chose the maximum peak that occurred between the 30th and 95th percentile of values of β.

Penalized Negative Normalized Log Likelihood

On each of the solutions identified via the Pareto frontier, we implement a model selection approach that penalizes models which over-fit the data while avoiding the significant error reduction that arises from increasing from k weights in the solution to $k+1$. Here, we employ the minimum description length model selection approach that identifies the model fit for which the normalized negative log likelihood evaluated at the solution plus a penalty $\frac{k\log T}{2T}$ pertaining to the dimension k of the model is minimized [77]. Since the model fitting was performed using ℓ_1 regularization, we leverage recent findings that approximate the dimension of such solution as the number of non-zero coefficients (k) in the solution of the ℓ_1 regularized problem [78, 79]:

$$PNNLL[n] = \left(\sum_{t=0}^{T-1} ||\overrightarrow{y}(t) - AH_m^T \overrightarrow{w}(t)||_2^2 \right) + \frac{k\log T}{2T}. \tag{2.16}$$

The goal is to identify the active set where we find the smallest squared error plus the penalty on k. The result is a curve that has a local minimum or a point of inflection, Fig. 2.2 B shows an example PNNLL curve and the selected solution point. The point selection on the PNNLL curve is performed manually due to the variability in the curve formation under different simulation, recording, and noise conditions.

Analysis Methods

To evaluate the efficacy of these approaches we computed correlation coefficients (simulation only) and identified statistically significant wave propagation direction with a technique we previously leveraged [21, 22, 74] termed the phase gradient directionality (PGD). Additionally, we use stochastic dominance to compare the PGD results for the two methods when the observation arrays are noise alone. Finally, we estimate distributions of various metrics due to noise alone and computed p-values on these metrics when computed from data.

Phase Gradient Directionality

To extract wave propagation features of the slow wave from the recovered gastric surface electro-potentials, we applied a method from our previous work that was originally developed for physics and neuroscience communities [49] which has also been used to describe spatial patterns of GI activity with cutaneous multi-electrode recordings [21]. The PGD, a ratio between the norm of spatially averaged velocities and the spatial average of the norm of velocities, is a measure of how aligned wave velocities are at different spatial positions, with values falling between 0 (unaligned) and 1 (planar waves) [49]. A detailed derivation and description of the PGD can be found in [30, 74].

A byproduct of this processing is the extraction of wave direction from the sign of spatially averaged recovered source velocitiesOne interpretation of the PGD is as a measure of how “close” the activity is to being a plane wave. In order to accurately identify those samples for which we have statistically significant plane wave activity, we only consider those direction values for which $PGD_r(t) > 0.75$ for one second or longer (see [21, Fig 2]).

Stochastic Dominance

We next aimed to compare the GS and LKS methods to one another when noise was provided as input. In order to determine which method more consistently specifies PGD values that are near 0, we used the procedure of stochastic dominance [80] to compare the probability distributions for the percentage of time for which PGD ≥ 0.75 from the two methods. Stochastic dominance provides a partial order over probability distributions and allows for specifying when one distribution can be interpreted as describing a generative model that is "less noisy" than the other. Each probability distribution was represented from an empirical cumulative distribution computed from multiple simulations with statistically independent noise inputs during each simulation iteration.

Consider two random variables X and Y. Let X be a random variable pertaining to the percentage of time that PGD ≥ 0.75 when the original observation array was AWGN and the inverse method was GS with Pareto. Let Y be a random variable pertaining to the percentage of time that PGD ≥ 0.75 when the original observation array was AWGN and the inverse method was LKS. Each of these random variables has an associated probability distribution, P_X and P_Y, respectively. Stochastic dominance ($P_X \leq_{sd} P_Y$) holds if there exists a pair of random variables X and Y where X has distribution P_X, Y has distribution P_Y, and $X \leq Y$ with probability 1. $P_X \leq P_Y$ if and only if the cumulative distribution functions (CDFs) obey the following relationship [81]:

$$F_X(u) \geq F_Y(u), \qquad \text{for all } u \tag{2.17}$$

$F_X(u)$ and $F_Y(u)$ are the CDFs for the respective X and Y random variables.

Null Hypothesis Significance Testing

In this study, we test two hypotheses for the metrics of interest (correlation coefficient and percent of samples where PGD ≥ 0.75). We seek to understand if the metrics we compute from the processed data are statistically significant. We compute p-values and compare with a $\alpha = 0.05$, a confidence level of 95%.

To perform this computation, we applied the two methods (GS and LKS) to each subject's observation array which contained a large number (T = 3600) time samples of AWGN. We estimated the underlying distribution by combining the region specific correlation coefficients of the electropotential estimates from all 7 models. As such, we develop distribution estimates for the proximal1, proximal2, distal1, and distal2 regions (supplement Fig. S-43 and S-44). We created a second set of region specific distributions (supplement Fig. S-54 and S-46) from the percent of samples where PGD ≥ 0.75 to provide a statistical measure for the subject recording data.

Human Subject Data

For simulated data, the results from the algorithm can be completely characterized due to the knowledge of the ground truth which generated the observation array. However, when applying these inference methods to recorded subject data, no such ground truth is available. In our previous work we found statistically significant wave activity across all regions of the gastric surface for two subjects. Here, we extend the subject population to 7 subjects with varying underlying disease states (3 healthy controls, and 4 with gastroparesis). We collected 100 channel EGG recordings on 7 subjects for whom either CT or MRI was available. All subjects provided written consent to participate in the subject and were part of an ongoing study at the University of California, San Diego, whose institutional review board as provided ethical approval (IRB number 141069 "A pilot trial to evaluate the utility of passive, skin-mounted electrodes to monitor the electrical activity of the human digestive system."). The data was collected from a 10 x 10 electrode array connected to a 256 channel GTec g.HIamp system. The recording protocol was for each subject to begin the recording after having fasted for several hours. We recorded 90 minutes in total: 30 minutes of recording before each subject ate a standardized small meal and 60 minutes of recording afterwards. The resulting data was processed by first performing artifact rejection [30, 74], followed by filtering to between 0.015 Hz and 0.25 Hz to isolate the 0.04-0.06 Hz frequency range of interest. Finally, it was down-sampled from the original rate of 256 Hz to a sampling rate of 1 Hz. The data segments processed and presented here are 1200 time samples (20 minutes), starting from when the subject completed eating their meal.

Results

For each of the 7 subjects, we generated a simulated multi-electrode cutaneous EGG observation array that was derived from both abnormal and normal initiation scenarios. We injected AWGN with two different levels of noise variance in terms of signal to noise ratio (3 dB SNR, and 50 dB SNR) into each generated array. For each of these noisy observation states, we solved the inverse problem with both the group sparsity method and the LKS approach. We then applied the different approaches for data dependent model selection.

For the group sparsity inverse solution, we use the Pareto frontier approach only. For the LKS inverse, we first use the Pareto frontier approach on the Kalman smoother solutions from each active set, and then use the PNNLL approach to identify the best active set and thus the best overall solution. To smooth the PNNLL for solution identification, a 5 point moving average filter is applied to the curve to facilitate smoothness and identification of a local minimum. For all simulation data, we compare the results with Pearson's correlation coefficient. We also determine statistical significance by comparing the measured test statistics (correlation coefficient and percentage of samples for which PGD ≥ 0.75) to the distributions under the null hypothesis (estimated using simulations with AWGN noise inputs). Presented here are the group level results (averages across all subjects) for the 7 subjects analyzed. The Supplemental Materials contain the individual subject results.

Simulation Data

Fig. 2.5 shows the average correlation coefficient across all subjects for both methods in the high noise (3dB SNR, part A) and low noise (50dB SNR, part B) cases. Both approaches show improvement in the proximal 1 and distal 2 sections for the normal simulation. These regions are also where the normal simulation increases in signal level. In the central gastric regions, the LKS method outperforms GS in terms of correlation coefficient. Further, in the low noise setting, LKS outperforms GS in terms of correlation coefficient for all subjects in the gastric regions.

Fig. 2.6 shows the same as Fig. 2.5 for the abnormal simulation data. Both approaches show higher average correlation coefficient than the normal simulation. In the abnormal simulation, the 3.0 dB SNR case performs similarly to the 50 dB SNR case.

Fig. 2.7 shows the average correlation coefficient for each subject (across all gastric regions) plotted against the length of the organoaxial curve. In order to isolate the relationship between correlation coefficient and gastric length, only the 50 dB SNR simulations are presented. While both approaches show a small negative slope, the GS approach shows no negative trend in the normal simulation and a smaller negative trend than LKS in the abnormal simulation. The LKS for the normal simulation does show higher correlation coefficients than GS for smaller gastric lengths. In general an increase in CC for smaller gastric lengths is expected, since smaller gastric lengths have fewer parameters to estimate and thus estimation performance improves.

Table 2.1 presents the average correlation coefficient across all subjects for the different simulation type as a function of region and method. We also form an estimate of the noise alone distributions for each region and method in order to determine statistical significance (see the supplement Fig. S-43 and S-44 for the correlation coefficient distribution estimates). As also

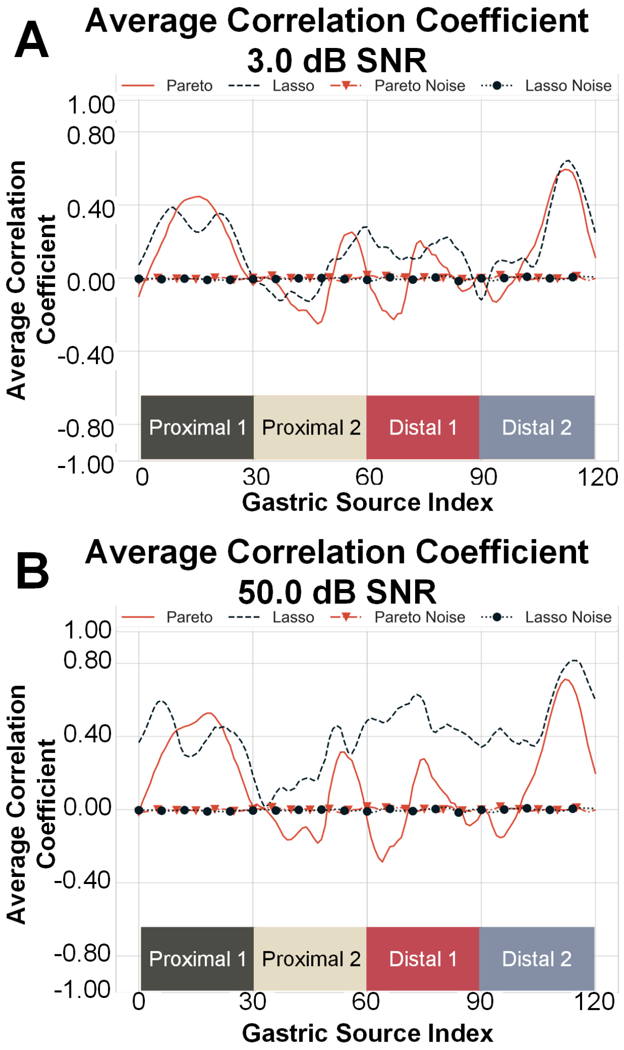

Figure 2.5: **Normal Simulation Average Correlation Coefficient** A) The average CC for all subjects both Group Sparsity with Pareto and Lasso Kalman for the 3.0 dB SNR normal simulation. Also shown is the correlation coefficient due to noise alone. B) The same as A but for the 50 dB SNR normal simulation.

indicated by Fig. 2.5, the correlation coefficients for the proximal 2 and distal 1 segments are lower and the p-values in this region exceed 0.05 for both GS and LKS in the proximal 2 segment and for the GS method alone in the distal 1 segment. For the abnormal simulation, the average GS correlation coefficients are higher than that of LKS; however, for the normal simulation the LKS method has higher correlation in the proximal 2 and distal 1 gastric segments.

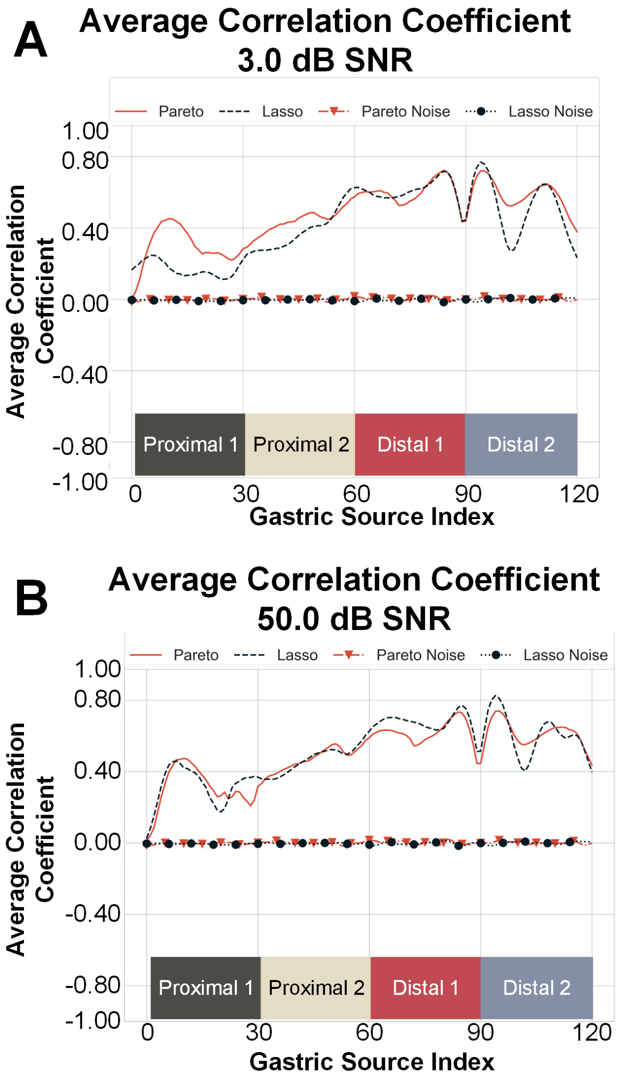

Figure 2.6: **Abnormal Simulation Average Correlation Coefficient** A) The average CC for all subjects both Group Sparsity with Pareto and Lasso Kalman for the 3.0 dB SNR abnormal simulation. Also shown is the correlation coefficient due to noise alone. B) The same as A but for the 50 dB SNR abnormal simulation.

Fig. 2.8 shows box plots for the percentage of samples, in a given 60 second time segment, for which PGD ≥ 0.75. It displays these percentages in terms of retrograde and anterograde directions. For example if in a given 60 second time segment we found 30 samples for which PGD ≥ 0.75, 20 of which were anterograde and 10 of which were retrograde, the anterograde and retrograde percentages would be 33.33% and 16.67% respectively. Both approaches show

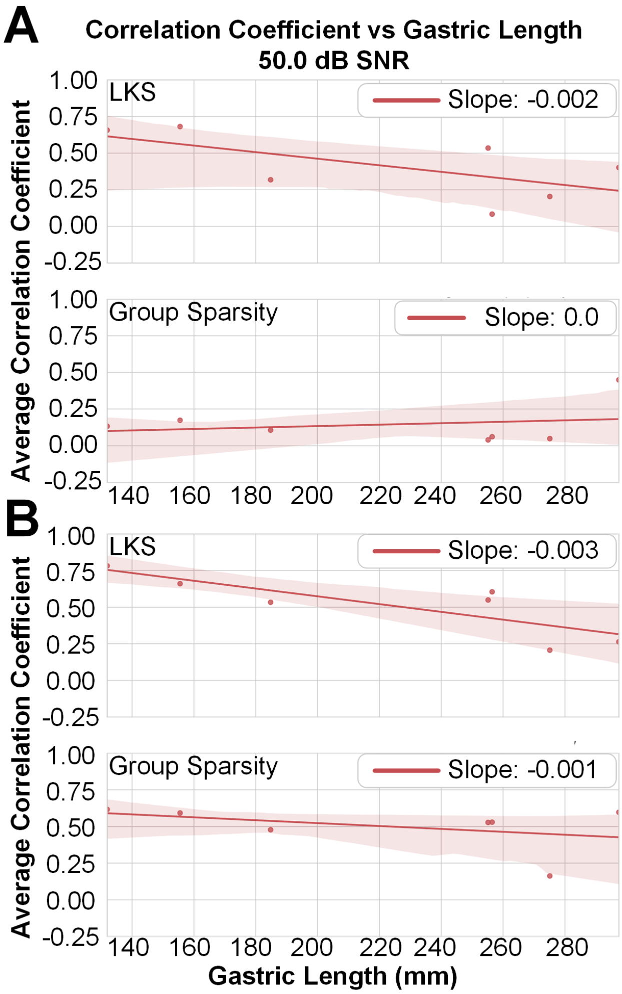

Figure 2.7: **Correlation Coefficient vs Gastric Length** Each subject's average correlation coefficient across all time samples and gastric sources for the 50 dB SNR simulations A). Normal (predominantly anterograde wave propagation) B) Abnormal (retrograde propagation in the proximal 1, proximal 2 and distal 1 gastric sections, anterograde in the distal 2 section)

recovery of the simulated wave patterns. Specifically in part A and D of Fig. 2.8, higher levels of anterograde activity are found across all gastric regions (which is consistent with the normal simulation). Moreover, parts B and E of Fig. 2.8 show higher levels of anterograde activity in just the distal 2 segment; everywhere else is predominantly retrograde (which is also consistent with the abnormal simulation). Also shown are the PGD direction percentage values due to noise alone (Fig. 2.8 C and F). As expected, i) there is no directional difference in terms of the percentages,

Table 2.1: Average Correlation Coefficient and P Values for 3.0 dB SNR Simulation Data

	Proximal 1		**Proximal 2**		**Distal 1**		**Distal 2**	
Methods	**GS**	**LKS**	**GS**	**LKS**	**GS**	**LKS**	**GS**	**LKS**
Abnormal	**0.28**	0.167	**0.432**	0.37	**0.617**	0.611	**0.602**	0.518
Normal	**0.292**	0.263	-0.02	**0.005**	0.053	**0.143**	**0.281**	0.25
Noise	-0.004	-0.002	0.001	-0.005	-0.001	-0.005	-0.005	0
Abnormal P-Value	0	0	0	0	0	0	0	0
Normal P-Value	0	0	**0.732**	**0.364**	**0.102**	0	0	0
Noise P-Value	**0.582**	**0.471**	**0.530**	**0.529**	**0.548**	**0.517**	**0.587**	**0.436**

Higher correlation coefficients and P values ≥ 0.05 have been highlighted in bold.

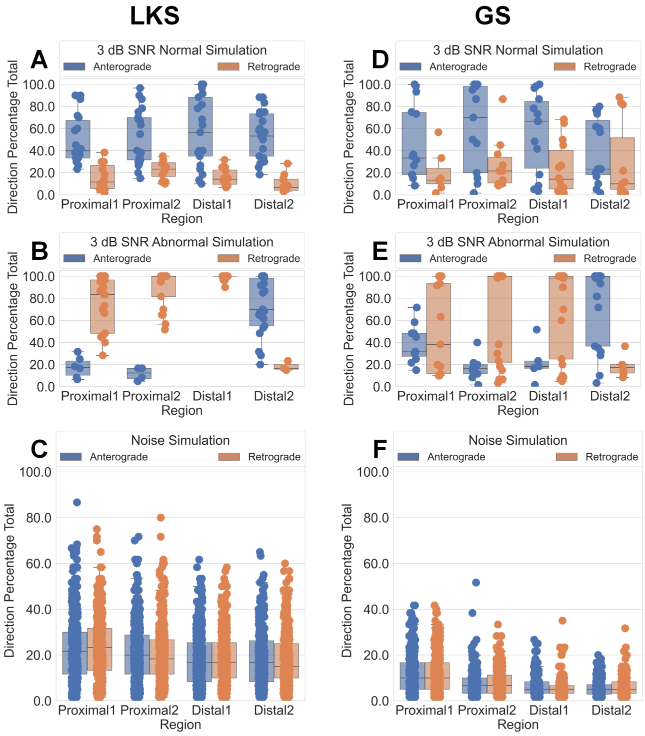

Figure 2.8: **Percentage of PGD Values Exceeding** 0.75 **in Each Direction** The percentage of PGD values exceeding 0.75 in the anterograde and retrograde directions for A) LKS normal simulation at 3dB SNR; B) LKS abnormal simulation at 3 dB SNR; C) LKS simulation with AWGN noise as observations; D) GS normal simulation at 3dB SNR; E) GS abnormal simulation at 3 dB SNR; F) GS simulation with AWGN noise as observations

and ii) the mean directional percentages in each region are significantly lower than those of the simulations in where there is a known direction ground truth. Lastly, the GS method finds lower numbers of samples for which PGD ≥ 0.75 than LKS for the noise alone simulation, indicating that GS is more robust to noise.

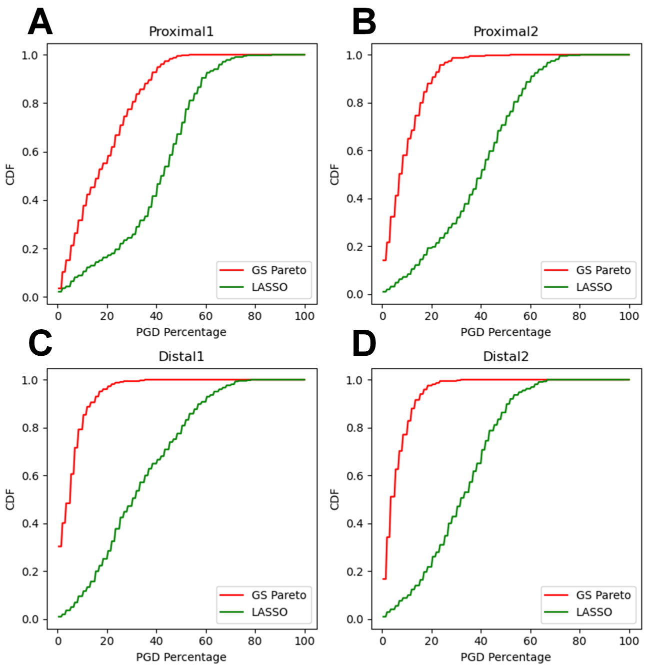

Figure 2.9: **Stochastic Dominance** The CDFs due to noise alone for both LKS and GS A) Proximal 1 region, B) Proximal 2 region, C) Distal 1 region, D) Distal 2 region

To further compare robustness of both methods to noise, as described in Section 2, we estimated the distribution of the percentage of samples whose PGD exceeds 0.75. The empirical CDFs (derived from the PDFs in Fig. S-45 and S-46) are shown in Fig. 2.9. In all scenarios, $F_{GS}(u) \leq F_{KS}(u)$ for all u between 0 and 1. As discussed in Section 2, this is a sufficient condition for stochastic dominance. As such, $P_{noise,GS} \leq_{SD} P_{noise,LKS}$ and when applied to noise alone, the GS method produces smaller numbers of samples for which PGD ≥ 0.75.

Table 2.2 shows the average PGD percentages for the 3.0 dB SNR simulation by method, region and underlying simulation type. As in Table 2.1 for correlation coefficients, we estimated distributions for the PGD values due to noise alone and used these to compute p-values. As expected, the noise alone simulations exhibit the highest p-values and as also found with the correlation coefficient, the highest p-values computed from recovered simulation data is with the LKS approach for the normal simulation in the proximal 1 and proximal 2 gastric regions.

Table 2.2: PGD Percentages for 3.0 dB SNR Simulation Data By Region

		Group Sparsity		**LKS**	
Region	**Data Source**	**PGD %**	**P-Value**	**PGD %**	**P-Value**
Proximal1	Normal	37.063	**0.051**	56.825	**0.163**
	Abnormal	51.984	0.01	80.635	0.01
	Noise	18.456	**0.218**	39.378	**0.501**
Proximal2	Normal	51.111	0	64.365	**0.07**
	Abnormal	71.111	0	91.984	0.001
	Noise	9.911	**0.252**	38.074	**0.501**
Distal1	Normal	54.365	0	66.587	0.03
	Abnormal	76.349	0	99.127	0
	Noise	7.287	**0.273**	32.687	**0.5**
Distal2	Normal	43.968	0	59.841	0.033
	Abnormal	81.032	0	75.159	0.002
	Noise	6.838	**0.274**	31.816	**0.5**

The GS approach has low p-value (< 0.02) in all gastric regions, for both normal and abnormal simulation.

Recorded Subject Data

For the recorded subject data, there is no ground truth against which to compare the recovered source results. We use PGD and p-values based on the estimated noise alone PGD distributions to derive confidence in our output results. Table 2.3 shows the average PGD percentages and the p-values for each approach in each region for the healthy and unhealthy subjects. With both approaches, we find time samples for which PGD > 0.75 in all regions of the gastric surface, for both healthy and unhealthy individuals. The p-values on the recorded subject data for the LKS approach are > 0.05 for all regions. The GS approach by contrast only shows $p > 0.05$ for the unhealthy individuals in the proximal sections. Due to the poor statistical significance (high p-values) results for the LKS approach, we limit the subject data PGD results to the GS approach in Fig. 2.10 and Fig. 2.11, as well as in the supplemental figures.

Fig. 2.10 shows the box plots of the PGD results for the recorded subject data, separated by method and subject classification (healthy vs unhealthy). Higher levels of anterograde activity

Table 2.3: PGD Percentages for Recorded Subject Data By Region

		Group Sparsity		LKS	
Region	**Data Source**	**PGD %**	**P-Value**	**PGD %**	**P-Value**
Proximal1	Healthy	56.638	0.005	55.137	**0.188**
	Unhealthy	22.884	**0.163**	47.479	**0.325**
Proximal2	Healthy	43.775	0	50.662	**0.24**
	Unhealthy	17.795	**0.095**	40.429	**0.448**
Distal1	Healthy	50.716	0	39.787	**0.347**
	Unhealthy	21.843	0.015	25.829	**0.648**
Distal2	Healthy	48.391	0	51.066	**0.104**
	Unhealthy	25.377	0.003	48.562	**0.136**

Solutions where $P \geq 0.05$ have been highlighted in bold.

are found in the healthy subjects. The unhealthy subjects show lower levels of wave activity in general and little to no statistical significance between the directions was found.

Fig. 2.11 shows the percentage of plane wave activity ($\text{PGD} \geq 0.75$) between the unhealthy subjects, the healthy controls, and noise alone. P-values between the groups, computed with the Kruskal-Wallis H test, show statistically significant differences ($p = 0.0$) in all regions. Healthy controls show higher levels of wave activity (regardless of direction) in all regions of the stomach. Unhealthy subjects show higher levels of wave activity than noise alone.

Discussion

While group sparsity is a more computationally complex approach, the application of the Pareto frontier model selection procedure to the GS approach lends itself to a fully automated method for source-localizing the gastric slow wave, requiring no human intervention to identify a solution. By contrast, LKS still requires human intervention to perform model selection. In addition, GS is superior to the LKS method with respect to noise: it finds fewer noise samples for which PGD exceeds a threshold. Further, when taking into account anatomical differences, the GS method is less susceptible to increasing length of the organoaxial curve (with respect to the correlation coefficient in simulated data). Further, the wave activity percentages found with the

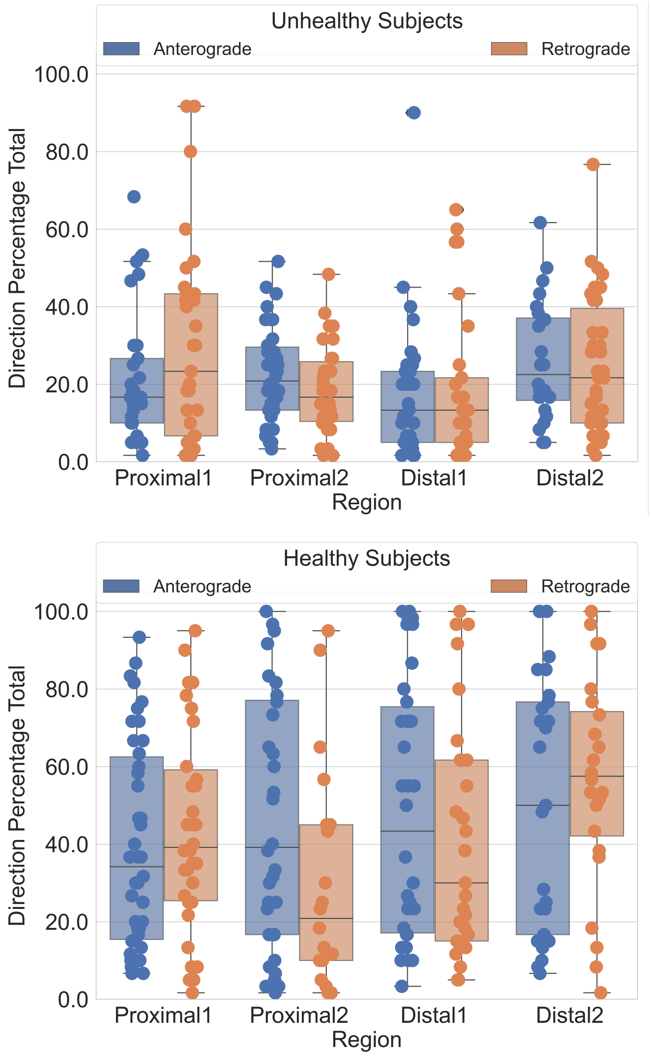

Figure 2.10: **Subject Recording Histograms** Group Sparsity PGD results for different regions for healthy and unhealthy subjects.

GS method, across all gastric regions, showed statistically significant increases in healthy human controls as compared to patients with diagnosed gastric disorders. Finally these results showed robust source localization of the gastric slow wave in subjects with BMI up to 31.5 kg/m2.

Simulation Data

Both approaches we explored were able to recover wave activity where PGD ≥ 0.75 with correlation coefficients greater than that of a noise alone simulation. Moreover, across all seven

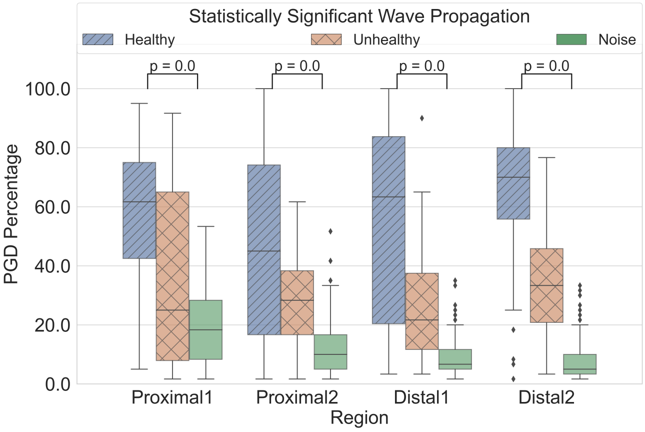

Figure 2.11: **Wave Activity** Percentage of statistically significant wave activity across healthy subject, unhealthy subjects, and noise alone.

subject models we are able to disambiguate between gastric regions. As showcased in Fig 2.8, we recovered the wave patterns we simulated in each of the gastric regions for both a low noise (50 dB SNR) case and a more realistic (3 dB SNR) example. The LKS method, while more computationally efficient than GS, struggled in the more proximal regions, resulting in lower correlation coefficients and higher p-values. Both methods had low correlation coefficients and high p-values for the normal simulation in the proximal 2 region. There were two regions, in the normal simulation, where the LKS approach out performed the GS approach, Proximal 2 and Distal1. This dip in correlation coefficient and increase in p-value may be due the the changing amplitude of the normal simulation (0.57 mV in the Proximal 1 and Distal 2 segments and 0.24 mV in the Proximal 2 and Distal 1 segments). Based on Fig. 2.7, we find that gastric length has a more pronounced impact on the LKS method as there is a stronger negative slope when plotting average correlation coefficient against the organoaxial curve length. The GS approach is flat or slightly negative and thus appears to be more robust to anatomical differences between subjects.

Recorded Subject Data

Based on the low p-values shown in Table 2.3 and the interpretation of the PGD as a measure of plane wave propagation, the wave activity identified by the GS approach is unlikely to be due to chance. The higher p-values from the LKS method in a controlled noise setting bring into question the validity of the findings in the human subject data. One explanation is that the separation of the methods, first enforcing sparsity and then smoothness, places too much wave like structure on the underlying data such that even with noise alone, a larger than anticipated number of samples have wave activity where PGD ≥ 0.75. The GS approach found statistically significant plane wave activity in each gastric region for healthy controls, and likewise in the distal gastric regions for the patients with GI disorders (see Table 2.3). In the healthy controls, we find more wave activity of both retrograde and anterograde directions. Subject 5 in particular shows dominant anterograde activity in all regions of the stomach (supplement figure S-36). Subject 6, also a healthy control, however shows dominant retrograde activity in all regions except for proximal 2 (supplement figure S-42). By contrast, in the unhealthy subjects, no direction dominates another. This matches our expectations for functional dyspepsia and gastroparesis, which has been shown both invasively and non-invasively [12, 22] to exhibit disordered gastric propagation patterns. We also identified more statistically significant wave activity (regardless of direction) in healthy controls vs unhealthy subjects. Importantly, we found more wave activity in the unhealthy subjects than the noise alone simulations. Still, without a secondary invasive measure (such as high resolution antro-duodenal manometry) with which to compare our inverse results on recorded subject data, we rely on p-values as confidence measures.

Future Work

With the rise of customizable, stretchable electrode arrays [82] which enable ambulatory, long time duration recordings [30], this fully automated technique for characterizing the gastric slow wave may be able to provide continuous monitoring and feedback in the future. As they can be fabricated into arbitrary patterns, stretchable electrode arrays can be “tuned” in size (electrode diameter) and density (number of electrodes per unit area) to support the optimal trade off, in a subject-specific fashion, between electrode impedance and spatial resolution. More work is needed to fully explore the limits of employing such approaches.

Future work is needed to provide “ground truth” information to compare to our estimates from human subject recordings. Simultaneous cutaneous and serosal multi-electrode recordings have not been established due to the obvious challenges involved with surgery. As an approximation to the ground truth, recent studies have succeeded in acquiring simultaneous cutaneous and mucosal recordings (the latter of which can be acquired concurrently with endoscopy) [83, 84]. Although these simultaneous recordings are nascent, if they eventually are performed in a large patient cohort, they can be employed in tandem with our methods to establish comparisons between our estimates and the ground truth derived from mucosal recordings.

Conclusion

There is a significant need for more non-invasive diagnostic tools for the clinical evaluation and diagnosis of GI issues. Here we have applied two Bayesian inference techniques to a selection of 7 subjects (3 healthy controls and 4 subjects with diagnosed GI disorders). We found that both of our methods were able to disambiguate between gastric wave activity in different regions of the stomach and compute wave direction. Furthermore, our approaches use a data dependent method for model selection to determine the optimal hyperparameters. Ultimately, we found that the group sparsity approach, while more computationally intensive, was more robust to variations in gastric length and found statistically significant metrics of interest in all regions as compared to our other method. The fact that this was robust to varying physiology (gastric length and subject BMI) is further suggestive that this approach could be of significant future clinical utility.

Acknowledgments

Chapter 2, in full, has been submitted for publication to IEEE Transactions on Biomedical Engineering, 2021. Alexis B. Allegra, David C. Kunkel, and Todd P. Coleman The dissertation author was the primary investigator and author of this paper.

Chapter 3

Biopotential Electrode Array Optimization for Source Localization of the Gastric Slow Wave

Introduction

10 percent of initial patient primary care visits are due to gastrointestinal (GI) complaints. While physical blockages or gastric infections are straightforward to diagnose, neuromuscular dysfunction, which comprises more than half of all GI disorders, is more complicated to diagnose and treat. The most prevalent neuromuscular disorders in the upper GI tract are gastroparesis (GP) and functional dyspepsia (FD) [3, 72, 73]. GP is characterized by delayed gastric emptying in the absence of a mechanical blockage and is found in 70% of Parkinson's patients [3] and 50 % of diabetes patients [4]. Further, the diagnoses process often involves non-invasive but subjective symptom based questionnaires, or highly invasive objective measures. While some common procedures can capture motor aspects of gastric function, these features do not always correlate with symptoms or treatment response [7–9]. On the other hand, gastric slow wave recordings from multi-electrode arrays placed on the stomach surface during open-abdominal surgery showcase abnormal spatial propagation patterns of subjects with gastroparesis [12].

GI neuromuscular function begins with the activation of rhythmically oscillating pacemaker cells termed the interstitial cells of cajal (ICC) [11] which control smooth muscle cells. The spatiotemporal coordination of the ICCs comprise the slow wave and enables the peristalsis which moves food through the GI tract. In general, gastric ICCs oscillate at 3 cycles per minute (0.05 Hz). Normal activity is characterized by a slow wave which propagates in an anterograde fashion from the top of the greater curvature towards the small intestines.

One method for non-invasively characterizing the gastric slow wave is through the use of the high resolution electrogastrogram (HR-EGG), a developed method used in a fashion similar to that of the EEG for the brain [21]. Multi-electrode arrays are placed on the abdominal surface in line with the antrum of the stomach (often guided by CT, MRI, or ultrasound), and the electrical signals emanating from the gastric surface are recorded. The multi-electrode array utilized for HR-EGG contains standard off the shelf electrodes which limits our ability to control the diameter of electrodes for varying electrode density and spatial resolution to optimize the received signal to noise ratio of the gastric slow wave.

While the HR-EGG has been recently shown to correlate with symptom severity [22], because of volume conduction, it only captures spatial information relative to the cutaneous surface, as such it is unable to disambiguate between different regions on the gastric surface. In our previous work, we have shown that by performing Bayesian Inference based source localization on the recordings taken for HR-EGG, we can not only extract spatial wave dynamics, but further we can do so in an region specific manner. [74]. Specifically we use maximum a posteriori (MAP) estimation procedure with a group sparse prior model which encourages sparsity in the number of spatial weights while simultaneously enforcing smoothness in the temporal evolution of these weights. This spatially sparse and smooth in time model is consistent with physiologic findings [11].

In our previous studies we limited ourselves purely to recordings of 100 channels, in which the electrodes were 3M red dot with an effective diameter of 8.6 mm. In simulation we were able to recover the sources with high correlation coefficient [74] and in the recorded subject data we found wave activity metrics of interest in all gastric regions across multiple subjects [85] with varying disease states. However the 100 channel array requires large amplifiers that are only rational in a clinical environment. In order to perform ambulatory measurements or longer recordings for which we can also successfully source localize the gastric slow wave, we need to understand the limitations of the electrode array (both number of electrodes and electrode diameter).

Flexible, customizable, stretchable, electrode arrays are a promising technology for gastric recording. They are non-invasive, comfortable and critically can be made in different electrode densities, diameters, and materials. We have recently demonstrated flexible electrode arrays (FEA) made of silver-silver chloride (AgAgCl) that can acquire the gastric slow wave signal [82]. No longer limited to available off the shelf components, FEAs can be built with arbitrary electrode diameters, thus allowing for simulations and modeling to inform the geometry of the electrode array for optimizing performance.

To explore different array configurations, we chose a 10 cm by 10 cm area on a 3D model of a subject's abdominal surface positioned over the gastric antrum. We model electrodes of varying sizes and compute both a normative (predominantly anterograde activity) simulation as well as an abnormal initiation (initiation beginning in the distal stomach and bifurcating into both anterograde and retrograde wave activity) simulation. We model the noise variance reduction due to the increased electrode size and add additive white Gaussian noise (AWGN) of varying noise variance to the simulated observation arrays. We then use electrical impedance spectroscopy (EIS) data collected on AgAgCl electrodes of varying sizes to measure the complex impedance as a function of frequency [86]. From this set of data we extrapolate an impedance model for AgAgCl electrodes of any size. Using Ohm's law, we model the RMS noise voltage, and again we add AWGN of varying noise variance (based on the RMS noise voltage computed) to the observation array. On each of these models (Noise Variance and EIS), we perform our group sparsity based source localization and compare the results. In order to determine the optimal array, for each array configuration, we use the noise variance model and compute the mutual information between the gastric sources and the simulated surface electrode recordings. We identify the optimal array by maximizing the mutual information.

This paper is organized as follows, Section 3 describes the time evolving 3D gastric model, the Flexible Electronic Arrays, Electrical Impedance Spectroscopy and the noise models. Section 3 discusses our approach to source localization with MAP estimation and the Group Sparsity prior. We discuss Fisher information and mutual information in section 3. In Section 3 we present analysis methods for extracting wave information and determining statistical significance. Section 3 provides the results of the two subject models used for both the EIS and noise variance models. Lastly, Section 3 and Section 3 provide discussion and conclusion, respectively.

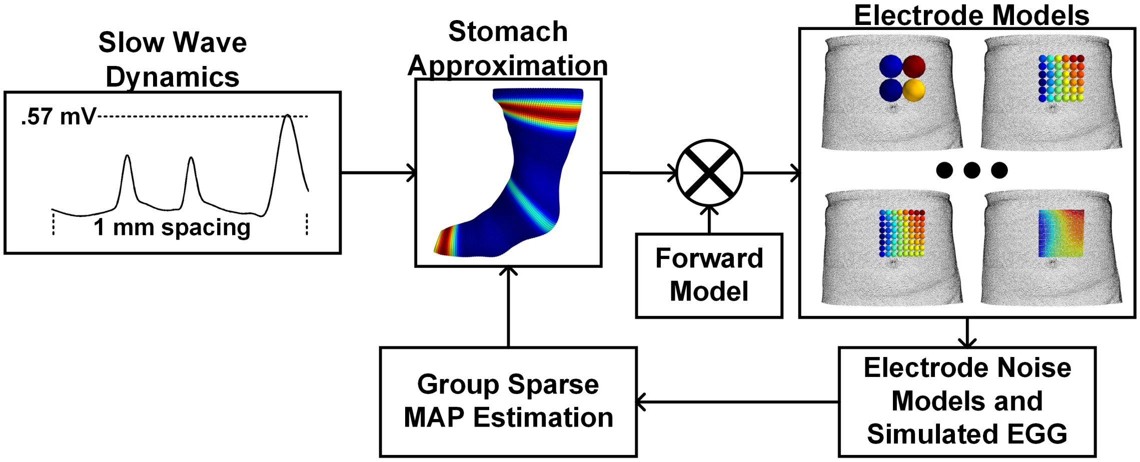

Figure 3.1: **General process of source localizing the gastric slow wave with different electrode configurations and noise models**

Modeling and Simulation

Here we use dynamic simulations and 3D gastric models previously developed and then expanded [74, 85] to compare different electrode noise models.

Time Evolving 3D Gastric Models

In previous publications [74], we have described the model development process used here in detail. We here provide a succinct description of the model we employ. Our time evolving gastric electro-physiologic model begins with extraction of a 3-Dimensional (3D) models of the gastric and abdominal surfaces from subject abdominal CTs or MRIs [33]. In order to map the dynamic electro-potential simulation to a variety of gastric surfaces, we utilized a simplified circular model of the stomach. Specifically, we first draw four fiducial curves on the cardinal sides of the 3D model [85]. We denote the organoaxial curve as the one that is closest to the abdominal surface. We determine the number of points on the organoaxial curve such that the inter-point spacing is 1 mm, and interpolate the other three curves such that they contain the same number of points as the organoaxial curve. With these four curves defined, we use the center of

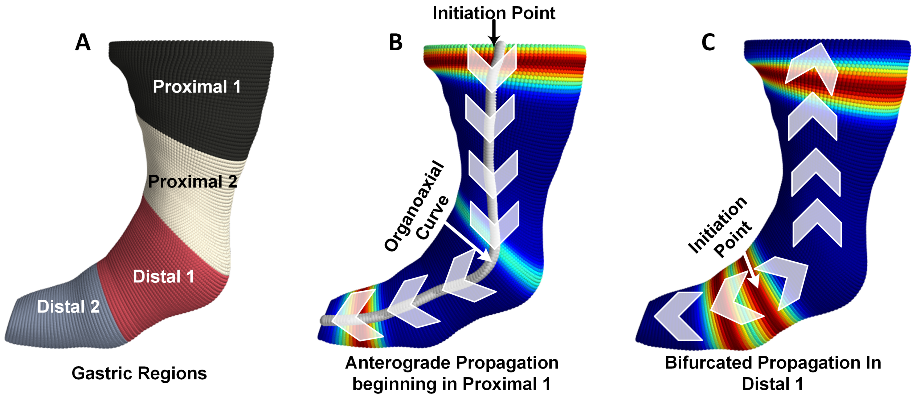

Figure 3.2: **3D Modeling and Simulation** A) The gastric surface divided into four regions. B) Normal simulation with exclusively anterograde wave propagation. C) Abnormal simulation with bifurcated propagation.

mass of the fiducial curves to compute circular rings whose radius varies with the geometry of the stomach. These circles are normal to the stomach geometry and the organoaxial curve.

Each of these rings represents the bands of equal potential on the gastric surface. On this set of rings, we map a time evolving simulation derived from invasive recording descriptions [11].

Similar to the pacemaker activity of the heart, the gastric slow wave is initiated by a group of pacemaker cells typically found on the upper portion of the greater curvature of the stomach. These cells trigger the activation of a network of interstitial cells of cajal (ICC). The activation of the ICCs spread isotropically along the gastric surface and initiate muscular contractions in the stomach corpus and antrum which underlie the stomach's peristalsis. Based upon preliminary findings in patients without underlying disease or symptoms, no more than five wavefronts occur at any point in time on the gastric surface [35]. The gastric slow wave is continuous in nature and under normal activity, it exhibits strong wave-like propagation patterns. It begins with high amplitude and speed, reduces and slows in the central region of the stomach, and increases again in speed and amplitude through the antrum [35–37]. Our simulation uses a finite difference approach to solve a 1-D wave equation with Mur's boundary condition to avoid wave reflections. The simulation for normal activity begins in the proximal stomach (closer to the esophagus) and propagates in an anterograde fashion to the distal stomach (closer to the duodenum). Our abnormal simulation models abnormal initiation based on preliminary findings from serosal recordings [12], the wave initiates in the first distal region and propagates in a retrograde fashion toward the esophagus and in an anterograde fashion toward the duodenum (fig 3.2 parts B and C).

Dynamic Simulated EGG Observations

The main goal of this study is to understand the effect of different electrode diameters and densities (number of electrodes per unit area) on our ability to source localize the simulated gastric slow wave. The abdominal 3D model is composed of many points in 3D space. We first model the electrode centers on the abdominal surface and then we process the 3D model to identify the points. To enable arbitrary placement of electrode centers, we used 3D slicer [33] to draw 6 vertical fiducial curves and 6 horizontal fiducial curves each containing 6 points. This defined a baseline grid of 36 points. Each of the curves was then interpolated up to a maximum of 65 points which resulted in a grid of 1024 electrode centers. In order to maximize the 10 cm x 10 cm surface area used, the electrode diameters were determined by the spacing between these electrode points. Each electrode is defined by the center and the number of points on the abdominal surface that represent the area the electrode covers.

The simulated electrode grids begin with 4 electrodes, each with a diameter of 50 mm, and increases to an electrode array with 1024 electrodes with 3.125 mm diameter each.

On each of the simulated electrode arrays, we solve our simplified current dipole [38] based forward model which assumes that the gastric surface and the abdominal surface exist in the same homogeneous volume of constant conductance.

$$A_{n,i} = \frac{cos\theta}{4\pi\sigma r_{n,i}^2}. \tag{3.1}$$

Where the angle between the organoaxially oriented current dipole and the abdominal surface is represented by θ, the constant conductance is σ, and r is the Euclidean distance between the ith current dipole source on the gastric surface and the nth abdominal sensor [38].

The EGG signal at each of the electrodes [39] is modeled by:

$$Y_m(t) = \sum_{i=1}^{D} A_{m,i} x_i(t) + N_m(t). \tag{3.2}$$

$Y_m(t)$ is the time signal at each of the M electrodes, $A_{m,i}$ is the matrix representing the forward model (3.1), $x_i(t)$ is the electrical surface potential at each one of the D gastric sources. $N_m(t)$ is the 0 mean AWGN whose variance is determined by the noise model under investigation. Once the noise variance is computed either through the EIS model or the noise variance reduction model, the same σ^2 is used to generate noise realizations for each electrode [39].

Strechable Ag/AgCl Electrode Arrays

Conventional HR-EGG arrays rely on the manual placement of individual off-the-shelf electrodes on the abdominal surface. Conventional electrodes are of a few fixed sizes and thus present challenges in adapting the size of individual electrodes within arrays to optimize reconstruction performance. In addition, with manually placed individual electrodes, human error can result in imprecise inter-distances across the entire array. Further, attempting to deploy such arrays in long-term ambulatory settings can present irritation or fluctuating signal quality from pre-gelled off-the-shelf electrodes drying out over the course of recordings.

Recently established stretchable adhesive-integrated multi-electrode arrays [82] have been shown to enables continuous, comfortable, and customizable monitoring. While these arrays can be constructed of many materials, the use of silver-silver chloride (Ag/AgCl) combined with conformal contact to human skin results in a class of stretchable electronics that attain a high signal to noise ratio (SNR) at frequencies of interest for gastric monitoring (0.05 Hz). To characterize the complex impedance characteristics of these arrays, we performed potentiostatic eletrochemical impedance spectroscopy (PEIS) on a wafer of Ag/AgCl electrodes and performed model-fitting to determine the best parameter describing the observed exponential relationship between electrode diameter and impedance [86].

To perform this characterization, a petri dish was modified to support a metal header pin that made contact with a standard electrophysiologic 0.9% NaCl solution in the dish. The Ag/AgCl wafer with electrodes and measurement leads was placed inside the petri dish and the negative lead was connected to the header pin, while the positive lead was connected to each of the individual measurement leads (fig 3.3, A). The complex impedance was measured across from 0.01 Hz to 5 Hz with linearly spaced points. We extracted the complex impedance values at 0.05 Hz and performed an exponential curve fit to extrapolate complex impedance values at any electrode diameter. These complex impedance values were then used to compute the root mean squared voltage (Vrms) of a noise signal.

Electrical Impedance Spectroscopy Electrode Model

In order to model the Vrms of noise based only on the electrode diameter, we used Ohms law:

$$V_{RMS} = I|Z|. \tag{3.3}$$

V_{RMS} is the RMS voltage of the noise signal, I is the background current on the abdominal surface, and $|Z|$ is the magnitude impedance of the specific electrode diameter. To model I, we fixed the expected signal to noise ratio at the electrode array to be 3dB and computed the average signal power across the electrode array due to the noise free observations:

$$S_m = 10log(\frac{||\overrightarrow{y_m}||^2}{T}). \tag{3.4}$$

$\overrightarrow{y_m}$ is the time signal vector at each of the M electrodes. S_m is the signal power of each of the M electrodes. We use the average of S_m ($\overline{S_m}$) as the baseline signal power for the entire electrode

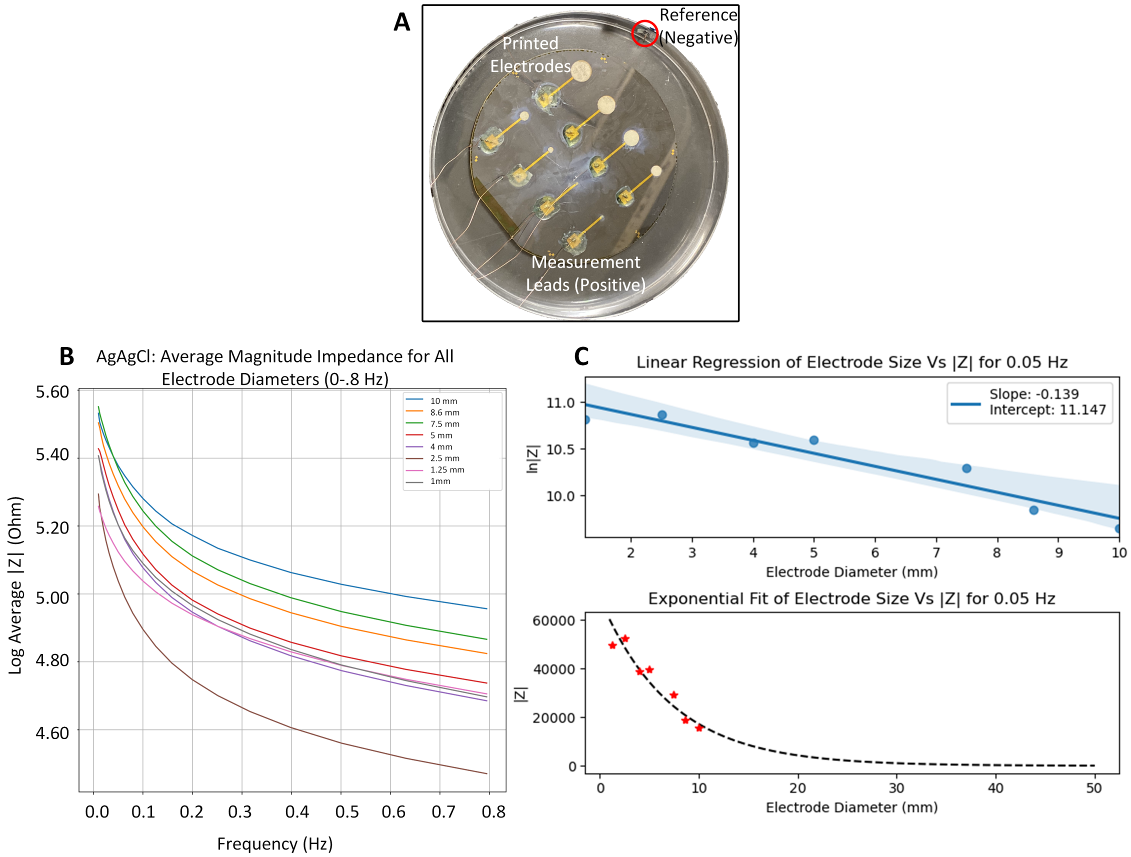

Figure 3.3: **EIS Measurement Setup and Curve Fitting**A) Wafer with electrodes of different diameters. B) Frequency vs log average $|Z|$ for each electrode in the wafer C) linear and exponential regression for $|Z|$ at F = 0.05 Hz

array. We then compute the noise power as:

$$S_{noise} = 10^{\frac{\overline{S_m}-3}{10}} \tag{3.5}$$

We compute a random sample of length T for the AWGN noise process, where each entry is $N(0, \sigma^2)$ where $\sigma^2 = \sqrt{S_{noise}}$. The noise V_{RMS} is root mean square measurement of the realization. Finally we compute current as:

$$I_{electrode} = \frac{V_{RMS}}{|Z|} \tag{3.6}$$

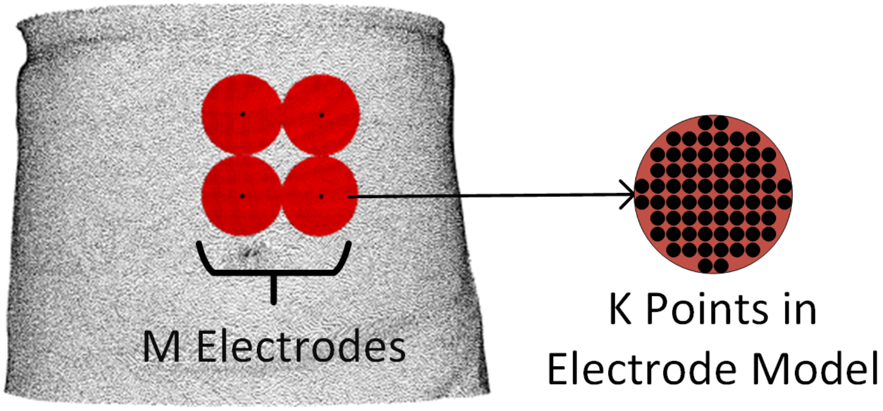

Figure 3.4: **Electrode Abdominal Models** Each electrode model for the noise variance reduction simulation contains K points around the central M electrode positions.

For each of the different diameter electrode models, we compute the current based on 3dB SNR and 10mm electrode diameter and then calculate the noise variance using the extrapolated impedance for the electrode diameter of interest and this baseline current. Realizations of 0 mean AWGN with this noise variance is then added to each simulated noise-free electrode observation in the array.

Noise Variance Reduction Electrode Model

The noise variance reduction model relies on the fact that electrode models of differing diameters are composed of increasing numbers of points on the abdominal surface. Because each point contains statistically independent additive noise, the variance of the noise pertaining to the averaging effect of the electrode reduces by L, the number of points in the individual electrode model. To formulate this, we computed the baseline noise variance from our previously used electrode models (100 channels of 1 cm diameter electrodes). We assumed a baseline SNR of 3dB as this is close to observed SNRs in subject recordings [30]. For each of the different electrode diameters, we divided this baseline σ^2 by the number of points in the electrode model. AWGN of this noise variance is then added to the observed electrode array as above.

MAP Estimation with a Group Sparse Prior

Even though the problem of source localizing the gastric slow wave is ill posed, we take advantage of the electrophysological properties of the stomach as we have done previously [74]. There are two key properties we leverage, (1) at any point in time there are a small number of bands of electrical activity on the gastric surface and (2) these bands move continuously in time. Because the electrical activity occurs in bands of equipotential, we represent the each band by a single point along the organoaxial curve. Additionally due to the continuous nature of the wave propagation, we encode the gastric activity as weights on a Fourier basis matrix H:

$$\begin{aligned} \overrightarrow{x}(t) &= H^T \overrightarrow{w}(t) \\ (H)_{k,i} &= \cos\left(\pi i \frac{k}{K}\right) \\ (H)_{k+\frac{K}{2},i} &= \sin\left(\pi i \frac{k}{K}\right) \end{aligned} \tag{3.7}$$

where $i = 0, \ldots, D-1$ is the spatial index at each of the gastric sources on the organoaxial curve and k/K for $k = 1, \ldots, K/2$ is the spatial frequency component [74]. With this representation the general signal model becomes:

$$\overrightarrow{y}(t) = AH^T \overrightarrow{w}(t) + \overrightarrow{N}(t) \tag{3.8}$$

Finally our localization problem is distilled to one of finding the optimal Bayes point estimate on the time evolving weights. To accomplish this we use a Maximum A Posteriori (MAP) approach which leverages both the measurement model $P(Y|W)$ as well as a prior distribution $P(W)$ on the weights. Our weight estimator is:

$$\begin{aligned}\hat{W}_{MAP} = \underset{W \in \mathbb{R}^{K \times T}}{\arg\min} \sum_{t=0}^{T-1} ||\overrightarrow{y}(t) - AH^T \overrightarrow{w}(t)||_2^2 \\ + \lambda \text{pen}(W).\end{aligned} \tag{3.9}$$

$\hat{W}_{MAP} = [\overrightarrow{w}(1), \overrightarrow{w}(2), \ldots, \overrightarrow{w}(T)]$ is the weight estimate and $\text{pen}(W)$ is the negative log of the prior distribution on W. The source estimate at any time t is: $\hat{\overrightarrow{x}}(t) = H^T \hat{\overrightarrow{w}}_{MAP}(t)$. In our previous studies we have identified a group sparse regularization technique whose prior encodes both spatial sparsity in the weights while also enforcing time smoothness yields the best results.

Group Sparse Prior

Our previously developed [74] group sparsity regularization technique in general is one that encourages sparsity amongst groups of weights and enforces a penalty on the first differences of those weights (similar to a Kalman Smoother). The resulting set is composed of a sparse subset of weights which are non-zero at any point in time, further those non-zero weights evolve smoothly in time. The group sparse penalty is as follows:

$$\text{pen}(W) = \sum_{k=0}^{K-1} \left(\sum_{t=0}^{T-1} d_k(t)^2 \right)^{\frac{1}{2}} \tag{3.10}$$

where d represents the first differences in the time of weights:

$$\overrightarrow{d}(0) = \overrightarrow{w}(0) \tag{3.11}$$

$$\overrightarrow{d}(t) = \overrightarrow{w}(t) - \overrightarrow{w}(t-1), t = 1, \ldots, T-1. \tag{3.12}$$

Conceptually this penalty is ℓ_2-norm of time differences which promotes time smoothness, wrapped in an ℓ_1-norm which promotes spatial sparsity. As a result, the source potential estimates are comprised of a small number of continuously time evolving spatial frequency components.

In the implementation for this study, we solve the group sparse prior over multiple λs and identify the optimal solution based on our underlying knowledge of the ground truth simulation.

Theoretical Limitations

Fisher Information

While MAP estimation is a powerful technique for identifying solutions to ill-posed problems, it is still a point estimation paradigm and thus does not quantify the uncertainty in our estimates [87]. In order to evaluate which electrode arrays allow for improvements in estimation, we take advantage of our forward model and utilize standard theoretical methods to quantify uncertainty in estimation. The curvature of the log likelihood function, captured by the Fisher information, is a frequentist approach to quantifying uncertainty.

For a frequentist statistical model of Y with density given by $f(y;\theta)$, the Fisher information can allow for describing the average curvature of the log likelihood $LL(\theta) \triangleq \log f(Y;\theta)$

$$I_y(\theta) = -LL''(\theta) \tag{3.13}$$

Where $I_y(\theta)$ is the Fisher information and $-LL''(\theta)$ is the second derivative of the negative log likelihood. $\theta \in \mathbb{R}$ is a real valued parameter. Typically this would be computed via a Taylor series approximation, however for Gaussian problems, the log likelihood is twice differentiable in closed form and the approximation is exact.

We can rewrite (3.8) by considering a the gastric source model at a single point in time $H^T \overrightarrow{w}(t_0)$ and treating it as a deterministic variable θ. The relationship between the gastric sources and a simulated electrode array of any size can be described as:

$$\overrightarrow{y} = A\overrightarrow{\theta} + N \tag{3.14}$$

Where A, the linear forward model, is fixed and non-random of size $D \times M$, θ is our non-random but uncertain parameter and N is Gaussian with mean 0 and variance σ^2. For this signal model in which there are D gastric sources and M electrodes, the covariance matrix is constant.

If we consider that each electrode is modeled by a group of K points around the central electrode point the linear Gaussian signal model becomes:

$$\begin{aligned} \overrightarrow{V} &= \frac{1}{K}\sum_{k=0}^{K-1} A_k \overrightarrow{\theta} + N_k \\ &= B\overrightarrow{\theta} + \overrightarrow{W} \end{aligned} \tag{3.15}$$

$$\overrightarrow{\mu}_v = B\overrightarrow{\theta} \tag{3.16}$$

$$\Sigma = \frac{1}{K}\begin{bmatrix} \sigma^2 & 0 & \dots & 0 \\ 0 & \sigma^2 & \dots & 0 \\ \vdots & \vdots & \ddots & \vdots \\ 0 & 0 & \dots & \sigma^2 \end{bmatrix} \tag{3.17}$$

Because the model is linear and Gaussian, the Fisher information reduces to a a $D \times D$ square matrix [88, 89]:

$$I(\theta) = B^T \Sigma^{-1} B \tag{3.18}$$

In order to perform optimal experiment to design and select the optimal electrode array, we map the Fisher information to a single comparative value by computing its trace [90]. One justification for this, for instance, is that for the linear Gaussian model (which coincides with our model), the performance of the minimum variance unbiased estimator is given by the trace of the inverse of the Fisher information matrix [89]. As such, minimizing estimator variance is equivalent to maximizing the trace of the Fisher information matrix [91].

Analysis Methods

Phase Gradient Directionality

We partition the organo-axial curve into 4 regions, where any $\mathcal{R}$ is one of proximal 1, proximal 2, distal distal 2, as shown in Fig 3.2 To measure how close the recovered source activity in any region is to being a plane wave (which occurs for each region in both the normal and abnormal simulations), we use a measure that we have applied on cutaneous multi-electrode recordings recordings [21, 22] as well as the gastric source potentials from source-localizing the slow wave [74]. This method, termed the phase gradient directionality (PGD), is given by.

$$PGD_{\mathcal{R}}(t) = \frac{\|\frac{1}{|\mathcal{R}|}\sum_{i\in\mathcal{R}} \nabla_\eta \phi(\eta_i, t)\|}{\frac{1}{|\mathcal{R}|}\sum_{i\in\mathcal{R}} \|\nabla_\eta \phi(\eta_i, t)\|}, \quad t = 1, \ldots, T \tag{3.19}$$

where $\nabla_\eta \phi$ is the spatial gradient of the instantaneous phase computed via Hilbert transform from the recovered gastric sources. Fundamentally the PGD is a measure of alignment between waves at different spatial positions. The values for the PGD fall between 0 (for unaligned waves) and 1 (for plane waves) [49]. As such, the PGD provides a comparative measure between the recovered wave patterns and a pure plane wave. One output of the PGD method is the sign of the spatially averaged recovered wave velocities, which provides a measure of the recovered source's traveling direction (anterograde or retrograde). Because the PGD can vary between 0 and 1, to identify statistically significant wave activity we use a detection threshold of $PGD_{\mathcal{R}}(t) > 0.75$ for at least one second to control false discovery rate [92].

Null Hypothesis Significance Testing

In order to determine if the metrics we compute (percent of samples where PGD ≥ 0.75 PGD and correlation coefficient) are statistically significant, we compute p-values and compare them with $\alpha = 0.05$, a confidence level of 95%. To accomplish this, we performed the group sparsity inverse method to an observation array containing only a large number of samples (T = 3600) of noise alone. We combine the results from both subjects for each of the abdominal array types and regions of interest. From this, we estimated the distribution under the null hypothesis for our metrics of interest in each region, for each abdominal electrode pattern. The histograms and estimated distributions are presented in the supplement figures S-9 and S-10.

Results

In this section, we present the results for the normal simulation. Analogous results for the abnormal simulation, histograms used to compute p-values, and all findings for the second subject (which mirror those of the first), can be found in the Supplemental Materials.

Fig 3.5 shows the median CC and median MAE as a function of electrode diameter for both noise models and both subjects. In both noise models, the largest diameter simulation with the fewest number of sensors has the lowest correlation coefficient performance. As the number of electrodes increases (for which the noise variance on each electrode increases) the CC improves before the noise overwhelms the increase in spatial density (around electrode diameter 15 mm). There is a corresponding rise in the MAE measure at the same point.

Table 3.1 shows the average correlation coefficients in a region for a given diameter. Based on our null hypothesis testing, we derive estimates of the distributions due to noise alone for the correlation coefficient metric and compute p-values. The diameters with the highest correlation coefficients are in bold and the P-values that are greater than 0.05, e.g. they fall below the 95% confidence interval, are marked in red. In general, the electrode array with high

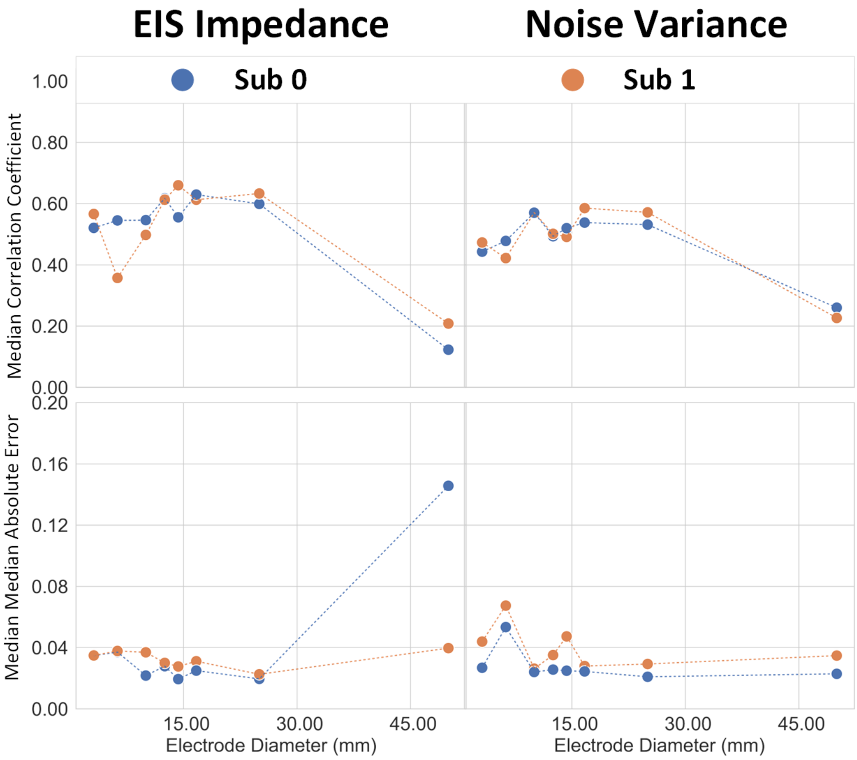

Figure 3.5: **CC and MAE for the Electrode Noise Models**

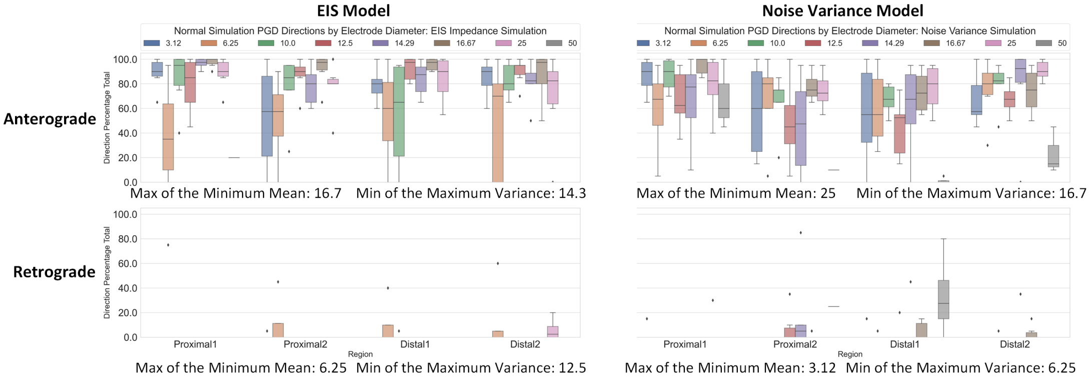

Figure 3.6: **PGD results for both Electrode Noise Models** Normal simulation for both subjects. Percent of time PGD ≥ 0.75 for at least 1 second separated by gastric region

correlation coefficient pertain to electrodes with higher diameters (16.66 mm). For the variance reduction model, the highest correlation coefficients occur with an electrode diameter of 10mm in the proximal 2 and distal 1 regions.

Table 3.1: Average CC and P-Values For both Models, all Diameters, Normal Simulation, Subject 0

Diam(mm)	**Proximal1**		**Proximal2**		**Distal1**		**Distal2**	
EIS	**CC**	**P**	**CC**	**P**	**CC**	**P**	**CC**	**P**
3.12	0.640	0.000	0.338	0.019	0.450	0.005	0.535	0.000
6.25	0.650	0.000	0.400	0.007	0.467	0.003	0.565	0.000
10	0.672	0.000	0.438	0.004	0.448	0.005	0.579	0.000
12.5	0.692	0.000	0.450	0.003	0.518	0.001	**0.662**	0.000
14.29	0.687	0.000	0.447	0.003	0.460	0.004	0.574	0.000
16.67	**0.721**	0.000	0.450	0.003	**0.546**	0.001	0.593	0.000
25	0.717	0.000	**0.452**	0.003	0.507	0.002	0.580	0.000
50	0.225	0.080	0.036	0.417	0.003	0.498	0.148	0.174
VAR								
3.12	0.640	0.000	0.307	0.030	0.342	0.020	0.514	0.000
6.25	0.569	0.000	0.400	0.007	0.287	0.042	0.519	0.000
10	0.689	0.000	**0.420**	0.005	**0.507**	0.001	0.556	0.000
12.5	0.660	0.000	0.328	0.022	0.347	0.019	0.520	0.000
14.29	0.658	0.000	0.322	0.024	0.443	0.004	0.566	0.000
16.67	**0.695**	0.000	0.353	0.015	0.439	0.004	**0.580**	0.000
25	0.682	0.000	0.389	0.009	0.425	0.005	0.527	0.000
50	0.442	0.001	0.045	0.388	-0.003	0.511	0.447	0.002

Diameters with high average correlation coefficient are highlighted in bold, high P-values are highlighted in red

Fig 3.6 presents the results from the PGD analysis for each electrode configuration for the normal simulation. As expected in each simulation type, the wave direction is predominantly anterograde. However, in the largest electrode diameter (50 mm), essentially no wave activity is recovered in the EIS model and comparatively little in the noise variance model. The percentage of wave activity recovered increases in the middle electrode models and then decreases again as the noise variance increases and the electrode diameter decreases. The Noise Variance electrode model and the EIS model both show that electrodes in the middle of the range strike the best balance between spatial resolution and noise reduction.

Table 3.2 shows the average PGD percentage (percent of time samples for which PGD ≥ 0.75 for more than 1 second) for each region, noise model, and diameter. This table shows the results from the noise models side by side with the majority of the high PGD percentages

Table 3.2: PGD Percentages For both Models, all Diameters, Normal Simulation, Subject 0

Diam.	**Prox1 PGD**		**Prox2 PGD**		**Distal1 PGD**		**Distal2 PGD**	
(mm)	**EIS**	**Var**	**EIS**	**Var**	**EIS**	**Var**	**EIS**	**Var**
3.12	80.00	93.33	20.00	57.50	73.33	48.33	75.00	66.67
6.25	73.33	77.50	68.33	75.00	73.33	65.00	83.33	83.33
10	96.67	91.67	68.33	71.67	48.33	66.67	90.00	83.33
12.5	93.33	73.33	78.33	51.67	85.00	40.00	95.00	68.33
14.29	**98.33**	88.33	80.00	60.00	80.00	61.67	90.00	**95.00**
16.67	96.67	95.00	**96.67**	**78.33**	**96.67**	**76.67**	**100.00**	90.00
25	93.33	**96.67**	86.67	68.33	73.33	61.67	93.33	85.00
50	20	68.33	N/A	N/A	N/A	45	N/A	23.33

Solutions where the percentage of time PGD ≥ 0.75 is the highest in any column are highlighted in bold.

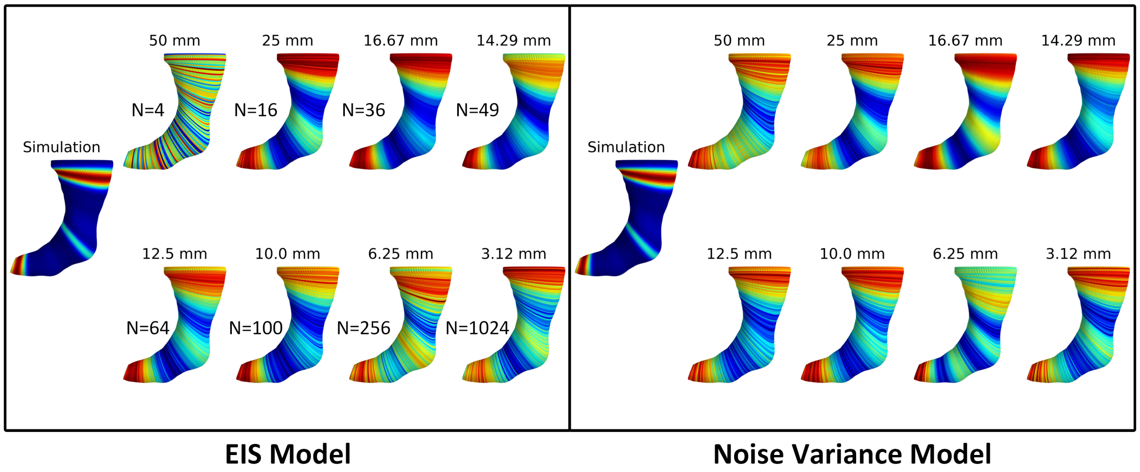

Figure 3.7: **Recovered Sources for both Noise Models** Normal simulation for subject 0, T = 12 seconds

occurring when the electrode diameter is 14.29 mm or 16.67 mm.

Fig 3.7 shows the 3D models of the gastric surface with the recovered sources mapped to the surface. Also shown is the ground truth simulation. Both the noise variance and EIS models show good recovery of the ground truth simulation. They also both show that the electrode models in the middle of the simulated group have the best recovery performance. In particular, electrode arrays with electrode diameters between 25mm and 14.3mm appear to most accurately recreate the ground truth. Larger arrays show higher noise content and smaller arrays show smearing or

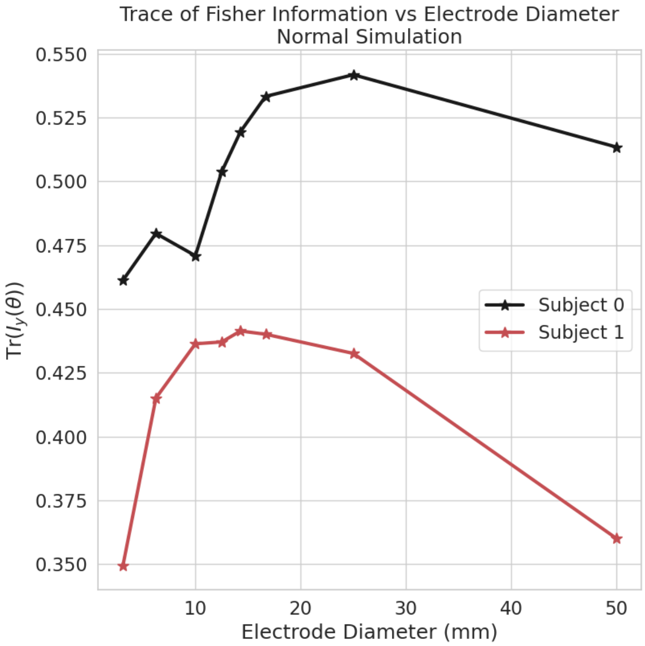

Figure 3.8: **Fisher Information vs Electrode Diameter**

widening of the recovered bands of sources.

Fig 3.8 presents the trace of the Fisher information as a function of electrode diameter. As expected, when the diameter is very high, with small numbers of electrodes the information content is low. As the number of electrodes increases, the information increases to a peak near an electrode diameter of 14.29mm for subject 1 and 25 mm for subject 0. As the electrode diameter decreases past these points, the amount of noise in the electrode reduces the available information.

Discussion

In general, our results indicate that the theoretical noise variance model matches the model created from the EIS impedance measurement. Fundamentally there is a tradeoff between electrode size and spatial resolution: too many electrodes results in too much noise and too few electrodes results in too little spatial resolution despite very low noise variance. In both models, electrodes around 16.67 mm show significant promise. Additionally, because these arrays only require 16 electrodes they are well suited to ambulatory settings and portable amplifiers [30,93,94]

Most of the electrode arrays modeled were able to recover source activity on the gastric surface. The largest electrodes (50 mm, with 4 electrodes in the array) were significantly worse at distinguishing region specific wave characteristics. This is unsurprising, given the findings from the Fisher information plot (Fig 3.8) which clearly show low information content at both high diameters (lowest noise, lowest spatial resolution), and extremely small diameters (highest noise, highest spatial resolution). Clearly too many small electrodes result in resulting in poor correlation coefficient and PGD percentages, due to noise overcoming any potential improvements in spatial resolution. On the flipside, when there are too few large electrodes, while the noise content is minimized, there is not enough spatial resolution to distinguish individual bands of gastric activity. Further, extremely dense arrays are not realistic to produce both in terms of fabrication capability and amplifier density.

Future Work

With the results of this study in mind a logical next step is to build flexible arrays of 16 or 36 channels and perform measurements on a variety of subjects to compare the outcomes.

Conclusion

In this study, we have compared an electrode noise model based on EIS measurements to that of a linear Gaussian Noise Variance model. We find that when source localizing the gastric slow wave, the theoretical noise variance model matches the trends observed with the EIS model. Both indicate that a smaller number of large electrodes produce better (higher correlation coefficient) results than a large number of small electrodes. Further, these simulated experiments agree with the theoretical results derived from the Fisher information matrix. This is a promising result for ambulatory recordings using customizable flexible arrays coupled with portable bio potential amplifiers.

Acknowledgments

Chapter 3, in full, has been prepared for publication. Alexis B. Allegra., Jonas F. Kurniawan; David C. Kunkel; Timothy Pham; Andrew K.L. Nguyen; Nathan L.J. Sit Boris Tjhia, Andrew J. Shin and Todd P. Coleman. The dissertation author was the primary investigator and author of this paper.

Appendix A

Chapter 1 Supplemental Materials

Other Inverse Methods

Below are the time/space plots of the reconstructed electrical potentials on the surface of the stomach for ridge regression, LASSO, and the Kalman smoother.

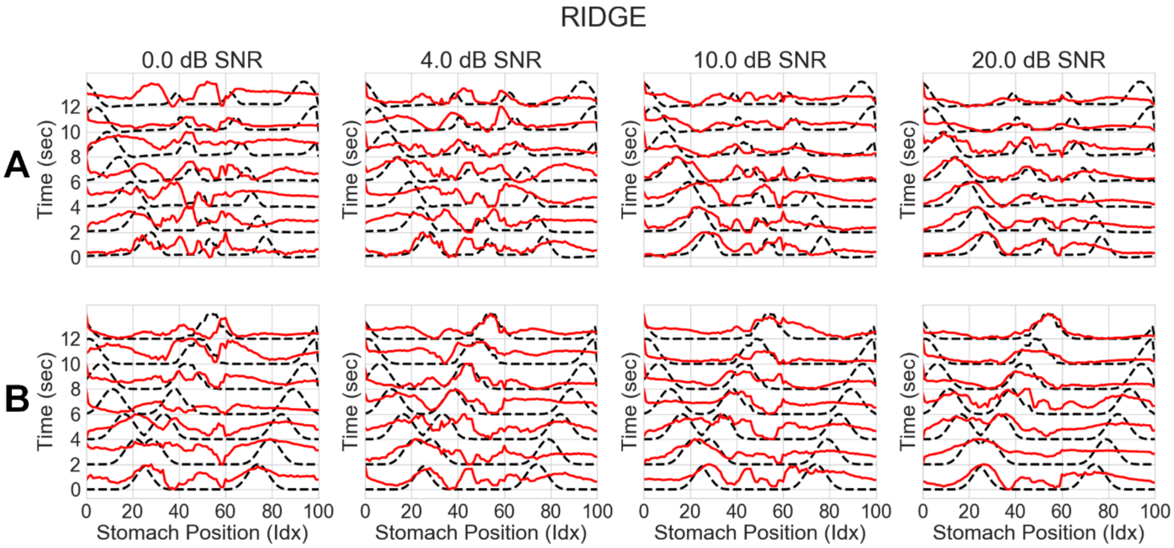

Fig A. Tikhonov Ridge Regression Inverse Solution on a Stomach Surface Line Across Noise Levels A) Ridge regression results (electrical potentials) against the ground truth for normal initiation simulation. B) Ridge regression results (electrical potentials) against the ground truth for abnormal initiation. In both normal and abnormal simulations, ridge regression is not able to fully reconstruct the ground truth wave pattern even under unrealistically strong signal conditions.

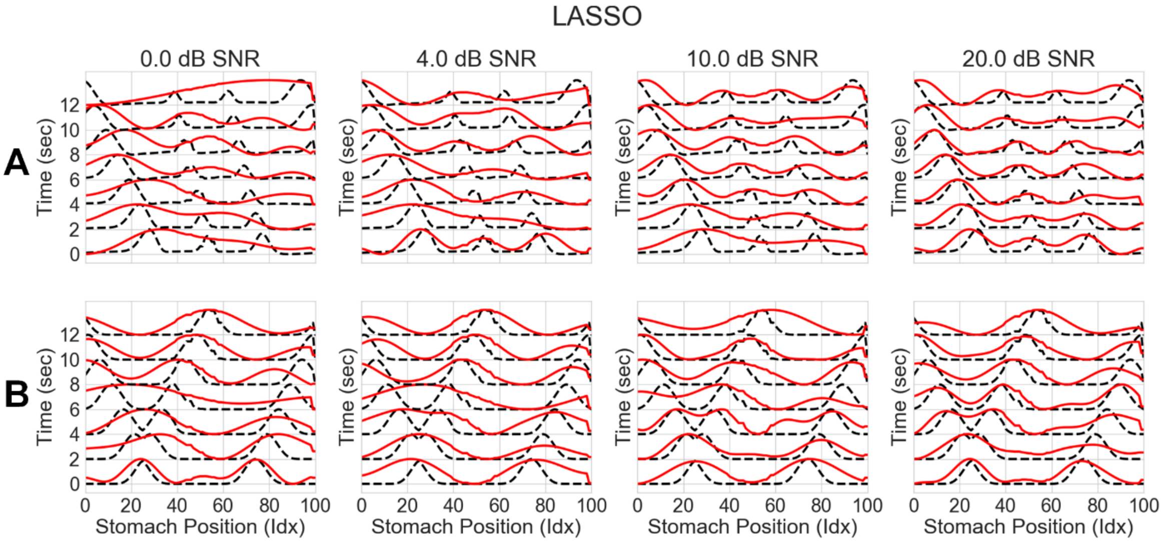

Fig B. LASSO Inverse Solution on a Stomach Surface Line Across Noise Levels A) LASSO results (electrical potentials) against the ground truth for normal initiation simulation. B) LASSO results (electrical potentials) against the ground truth for abnormal initiation. In both normal and abnormal simulations LASSO is only able to reconstruct the ground truth wave pattern where the signal is the strongest in the distal portions of the stomach. Even for these, it does not perform well in the presence of noise.

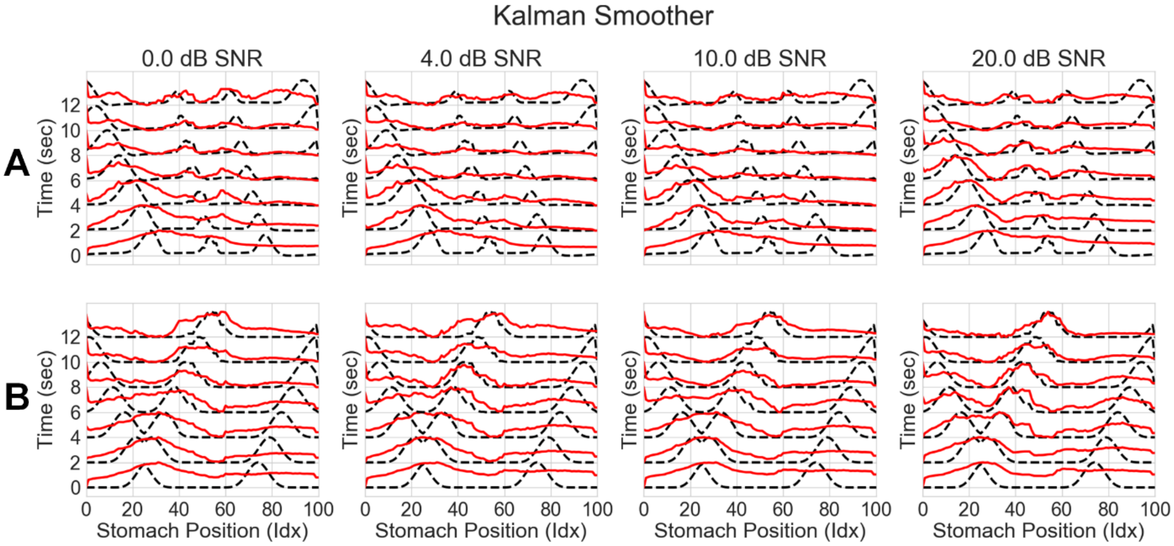

Fig C. Kalman Smoother Inverse Solution on a Stomach Surface Line Across Noise Levels A) Kalman smoother results (electrical potentials) against the ground truth for normal initiation simulation. B) Kalman smoother results (electrical potentials) against the ground truth for abnormal initiation. In both normal and abnormal simulations the Kalman smoother tracks the ground truth simulation fairly well after the first time point

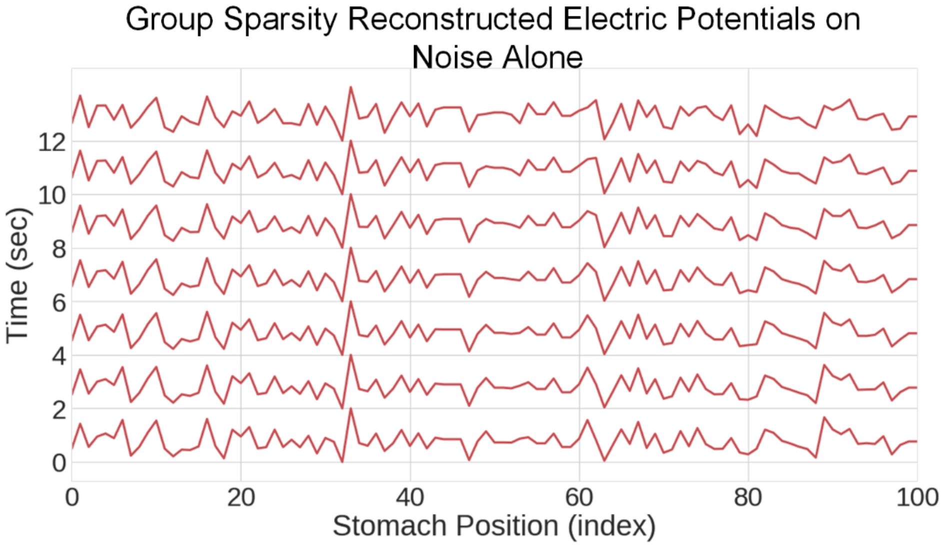

Fig D. Group Sparsity Inverse Solution on the Stomach Surface due to Noise Only The group sparsity inverse reconstructed potentials due to a noise only simulation; no wave activity.

Second Human Subject Results

For basic validation of these methods, we include results from a second human subject who had the same clinical description of motor function (GES at 30% at 4 hours) as the first human subject reported upon in the main manuscript. Below we report the reconstructed potentials for both the simulated waves (Fig E) as well as the actual recording (Fig F), and the histograms of wave direction (anterograde or retrograde) as a function of time and stomach region (Fig G).

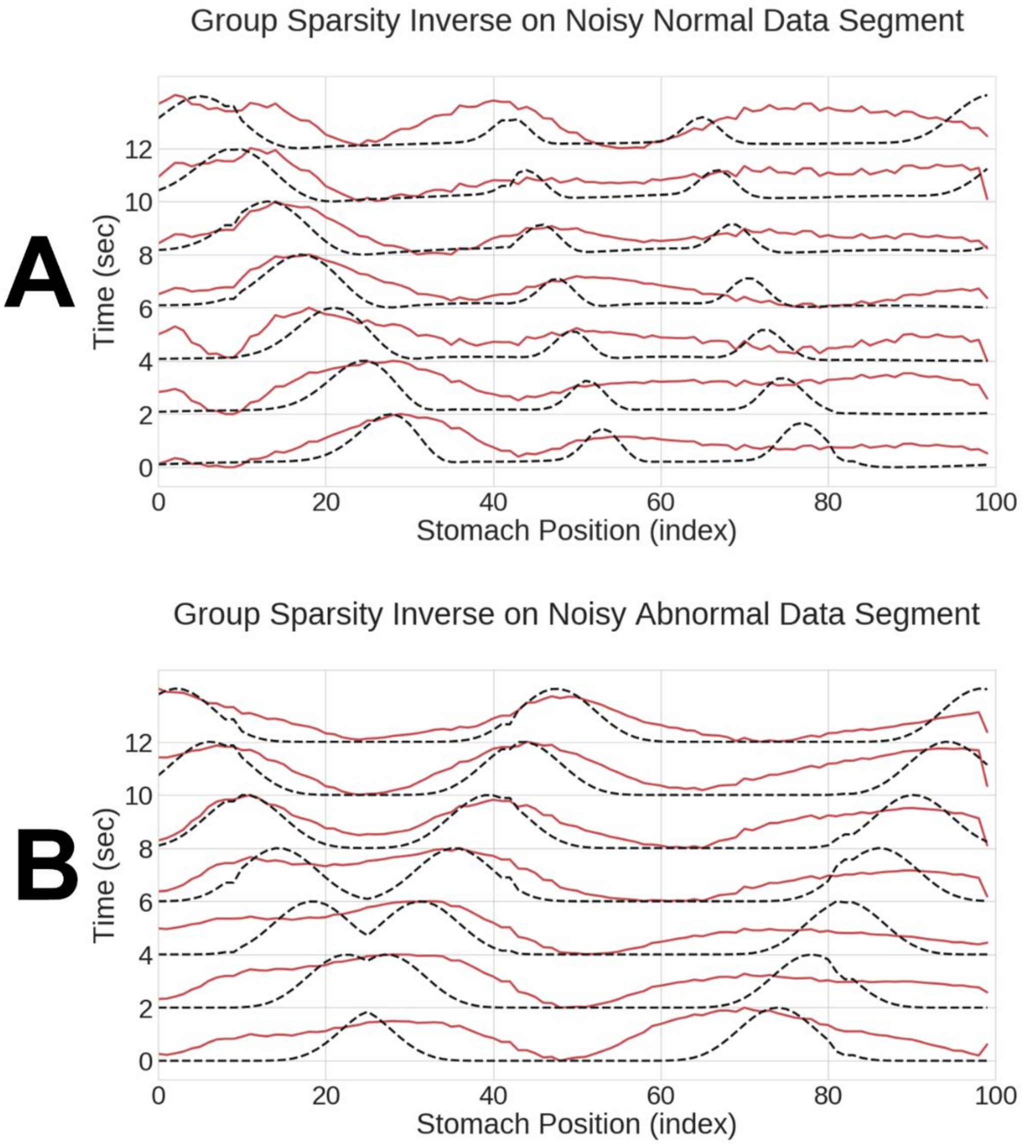

Fig E. Subject 2 Simulation Reconstructed Potentials The time and space reconstructed electrical potentials from the group sparsity inverse for the second subject. (A) is the reconstructed potentials for the normal simulation. (B) is the reconstructed potentials for the abnormal initiation simulation.

Along with the first subject reported in the main manuscript, this subject also was also involved in a recent clinical study that used the HR-EGG to identify cutaneous spatial patterns [1]. Commensurate with what occurred with subject 1, the spatial patterns we found using our inverse method on the cutaneous surface are consistent with the spatial patterns found on cutaneous HR-

EGG analyses from [1]. Specifically, in the inverse method we find strong retrograde activity in both proximal segments, which aligns with the spatial histogram from cutaneous HR-EGG found in Fig GP-8 in the supplemental materials of [1].

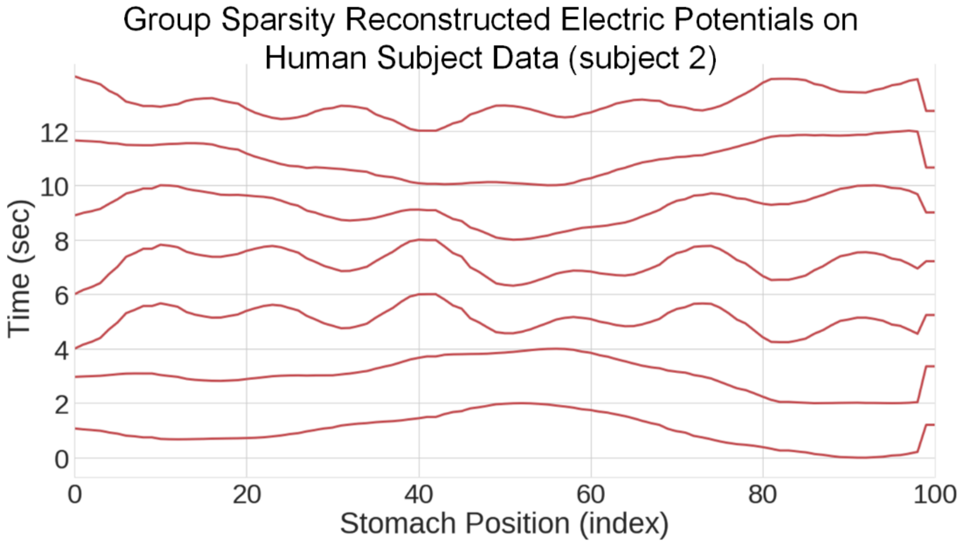

Fig F. Subject 2 Recording Reconstructed Potentials The time and space reconstructed electrical potentials from the second subject recording using the group sparsity inverse

Table A. Percentage of Time that PGD > 0.5 for Inverse Results Via Simulation Type and Region (Subject 2)

Data Source	Proximal 1	Proximal 2	Distal 1	Distal 2
Normal Simulation	48.3	75.3	64.3	84.7
Abnormal Simulation	52.7	97.3	95.3	92.3

In human subject 2, all areas of the stomach showed wave propagation, with the second distal section show-casing the highest percentage 84.7% of wave propagation in the normative data set. Strong activity is also present in the proximal 2 segment 75.3%.

Also, of note is that the distal 1 segment shows less activity than that of the proximal 2 segment for this subject. This may be due to the curvature of this particular stomach, as is seen in Fig G, versus that of subject 1 (Fig 9).

Differences in stomach geometry and stomach region proximity to the cutaneous surface are likely explanations for the percentages shown in Table 2.

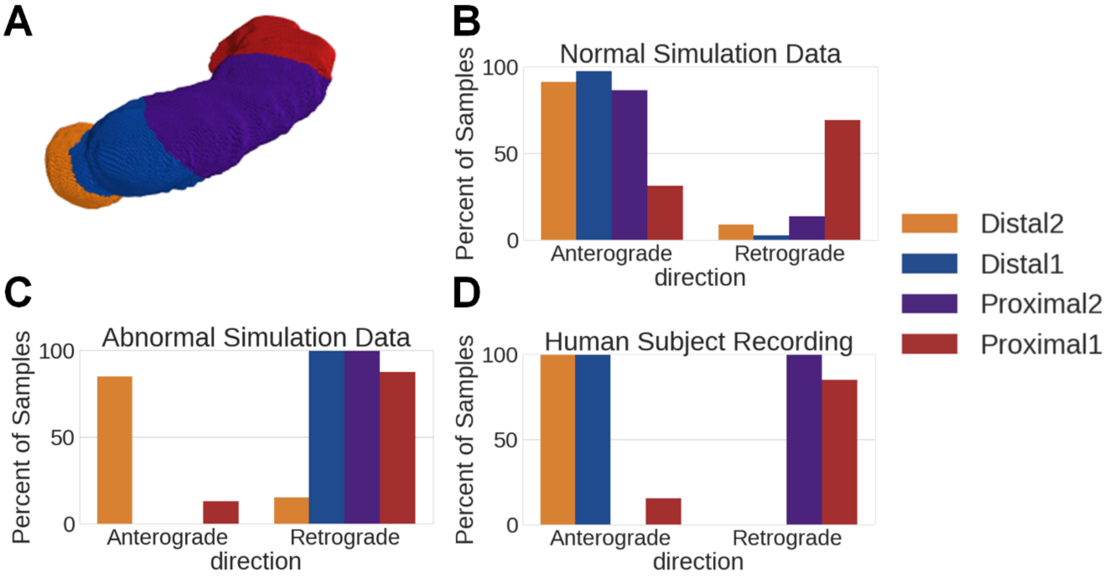

Fig G. Subject 2 Direction Histograms (A) the second subject stomach geometry mapped into 4 regions. (B) the direction histogram indicating entirely anterograde direction for the normal simulation. (C) the direction histogram for the abnormal simulation. (D) the direction histogram for the recorded subject data

In terms of geometry, each stomach and abdominal CT represent different geometric relationships between the abdominal surface and the gastric surface. The level of curvature in different stomach regions, and the effect that has on the propagation of electrical activity to the electrodes on the abdominal surface, can play a role. Further, eq 4 pertaining to the forward model contains a cos θ in the numerator, where θ is the angle between the current dipole (oriented organoaxially) and the observation point on the abdominal surface. As such, if we have strong curvature, cos θ can go through significant changes throughout that region and so the superposition principle can result in the cutaneous electrode array containing interference between nearby dipole sources. Altogether, this would result in a reduction in signal to noise ratio and thus a reduction in the fidelity during reconstruction. Notice that subject 2 has a significant amount of curvature, in comparison to subject 1, with most curvature occurring in the two proximal regions. We surmise that the lower PGD percentage in the distal 1 segment, as compared to that of the proximal 2 segment, is due in part to the more extreme curvature in the proximal segments.

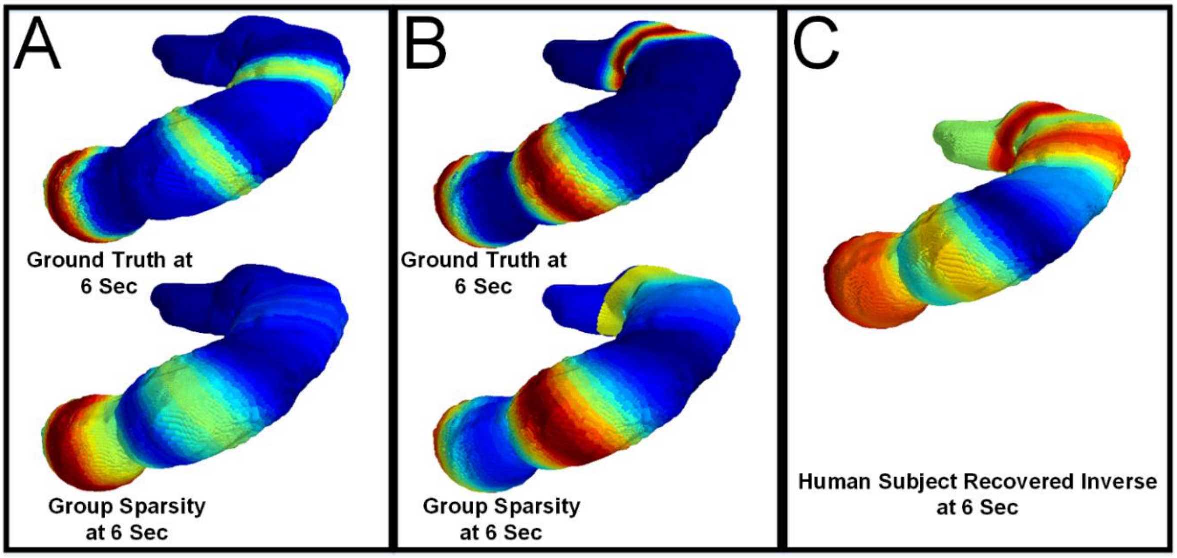

Fig H. Subject 2 3D Model Reconstructed Potentials (A) the second subject stomach ground truth normative simulation and reconstructed potentials at the same time point (6 seconds). (B) the second subject stomach ground truth disordered simulation and reconstructed potentials at the same time point. (C) the second subject reconstructed potentials from the recorded data

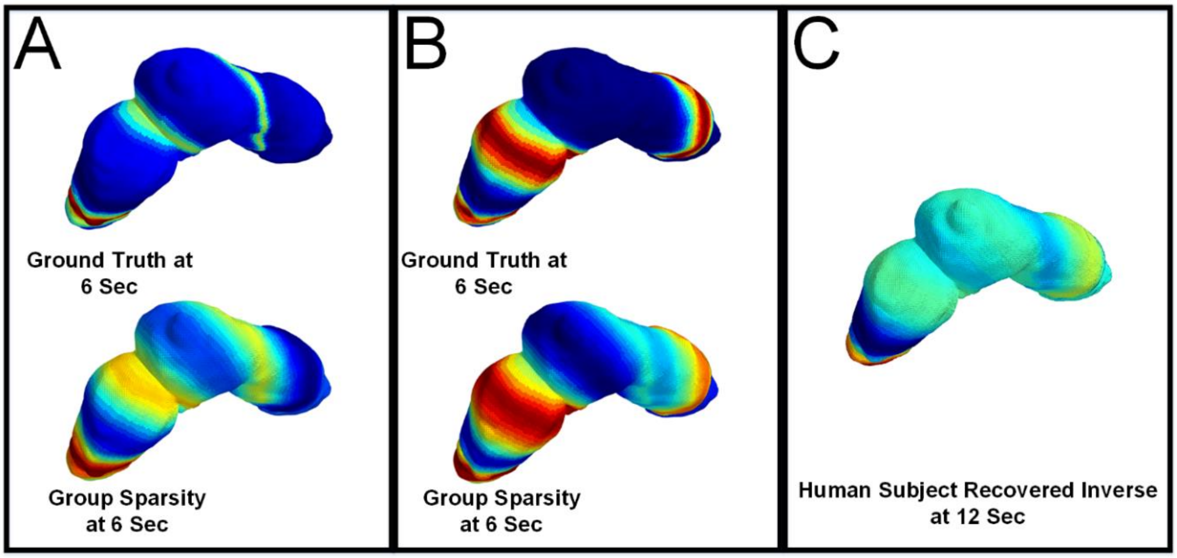

Fig I. Subject 1 3D Model Reconstructed Potentials (A) the first subject stomach ground truth normative simulation and reconstructed potentials at the same time point (6 seconds). (B) the first subject stomach ground truth disordered simulation and reconstructed potentials at the same time point (6 seconds). (C) the second subject reconstructed potentials from the recorded data

Figs H and I show the localization results on the stomach geometry of the two human subjects.

References

1. Gharibans AA, Coleman TP, Mousa H, Kunkel DC. Spatial Patterns From High-Resolution Electrogastrography Correlate With Severity of Symptoms in Patients With Functional Dyspepsia and Gastroparesis. Clinical Gastroenterology and Hepatology. 2019;.

Appendix B

Chapter 2 Supplemental Materials

Overview

In this set of supplementary materials, we present the results for each of the individual subjects. For each subject we provide:

- The 3D models (abdominal and gastric)
- The 3 dB SNR simulation results (normal and abnormal)
- The results due to noise alone
- A spectrogram of a single channel of the recorded observation
- The results from processing the recorded data

We also showcase the histograms and distribution estimates for the noise alone simulations for correlation coefficient and PGD percentages. These are used to compute the p-values in the primary document.

For each subject, regardless of disease state, we find a dominant frequency in the 0.04-0.06 Hz frequency band in the spectrogram. In general, the signal level is highest in the immediate post prandial time of the recording (the first 200 seconds).

While the Pareto frontier for some subjects recorded data appears similar to the Pareto frontier due to noise alone, as Fig. 10 in the primary document shows, the noise alone results in very small amounts of statistically significant wave activity compared to that of subjects with diagnosed GI disorders. This does vary on a subject-by-subject basis: subject 0 for example has very little statistically significant wave activity found in the recording with only 1 time segment showing more than 20% of the samples (12 seconds) with PGD > 0.75. Across all four gastric regions and 1200 time samples processed, there are 80 total time segments of 60 seconds each.

Table S-1 Overview of wave activity for recorded subject results on a per subject basis

Subject	**Health State**	**Number of Segments where PGD > 0.75 for more than 12 seconds**	**Total Number of Segments with PGD > 0.75**	**Percent of Strong Segments**
Subject 0	Non-Diabetic GP	1	7	14.3
Subject 1	Healthy	18	43	41.9
Subject 2	Severe Idiopathic GP	63	80	77.8
Subject 3	Early Diabetes GP	4	24	16.7
Subject 4	Diabetic GP	43	70	61.4
Subject 5	Healthy	62	68	91.2
Subject 6	Healthy	72	78	92.3

As Table S-I shows, there is variability between healthy and unhealthy subjects, as seen in the main document Fig. 10. Healthy subjects have more time segments in which PGD > 0.75, but one of the healthy subjects (subject 1) exhibits relatively little wave activity with only 43 of the segments exhibiting strong activity. Two of the subjects with GI disorders show wave activity throughout the majority of the recording (Subject 2 and Subject 4). However, these two subjects only exhibit wave activity in 77.8 % and 61.4% of the segments, in comparison to the two strongest healthy controls with 91.2% and 92.3% (Subject 5 and Subject 6). For validation of why different subjects exhibit such different amounts of wave activity, more study is required.

Subject 0 – Unhealthy: Non-Diabetic Gastroparesis

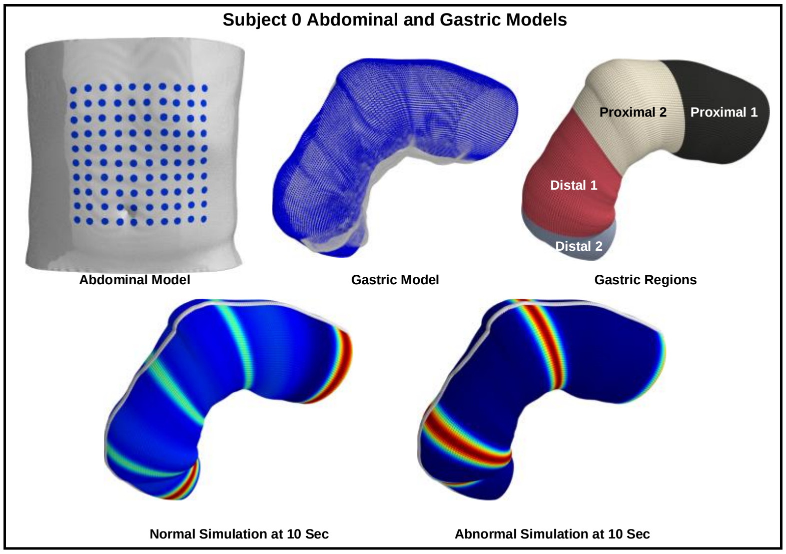

Fig. S-1 Subject 0 Abdominal and Gastric Surface 3D Models

Simulation Results

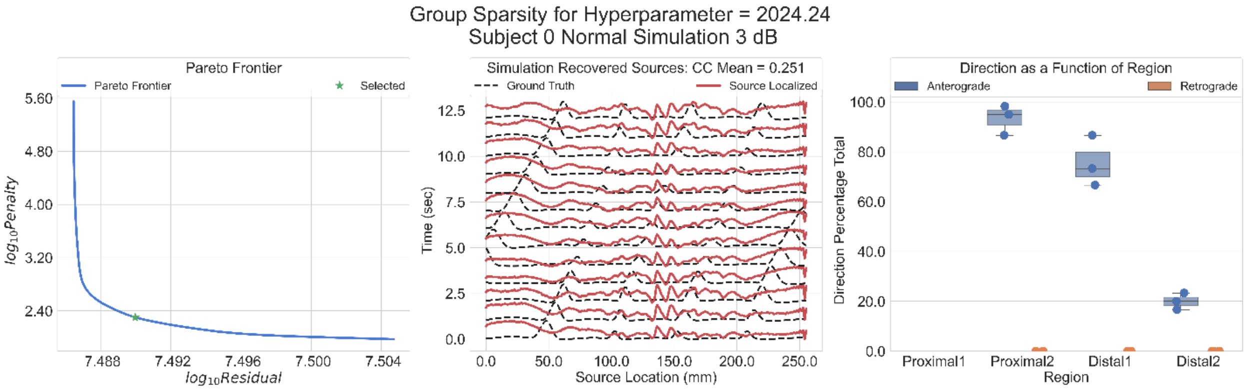

Fig. S-2 ***Subject 0 3.0 dB SNR Normal Simulation Results*** *– From left to right the pareto frontier with solution point selected, the recovered sources and the ground truth simulation, the directions computed from the recovered sources as a function of region. The average correlation coefficient across all time and all sources is 0.251*

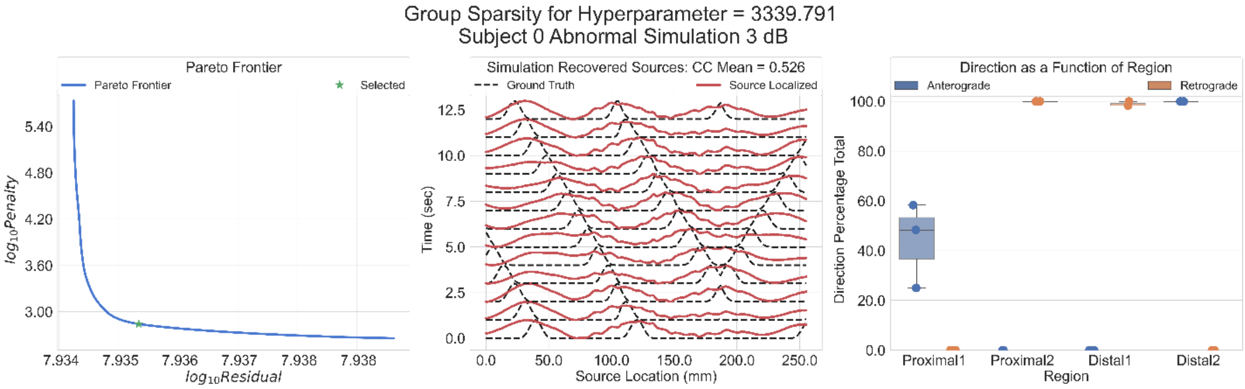

Fig. S-3 ***Subject 0 3.0 dB SNR Abnormal Simulation Results*** *– From left to right the pareto frontier with solution point selected, the recovered sources and the ground truth simulation, the directions computed from the recovered sources as a function of region. The average correlation coefficient across all time and all sources is 0.526*

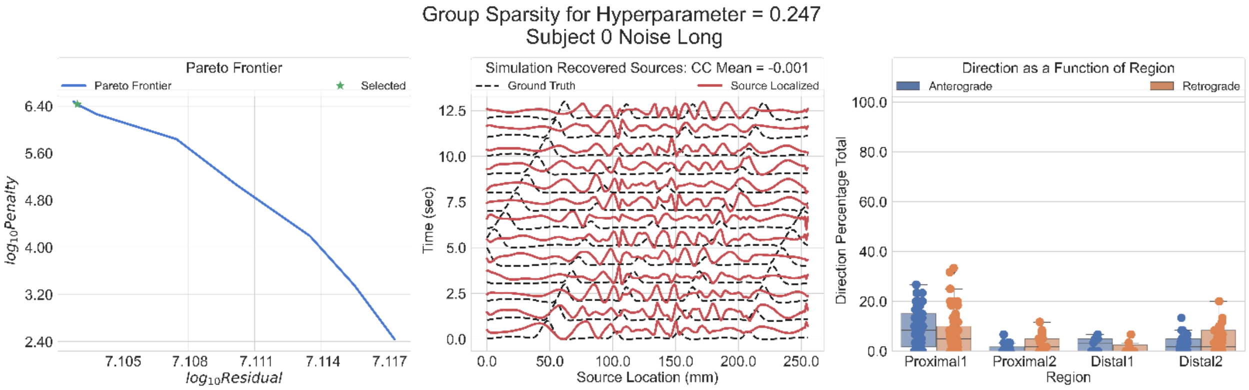

Fig. S-4 ***Subject 0 Noise Alone Observation Results*** *– From left to right, the pareto frontier with solution point identified, the recovered "sources" and the ground truth normal simulation that we compare against, the directions computed from the PGD of the recovered sources. The average correlation coefficient across all time and all spatial sources is -0.001*

Recording Results

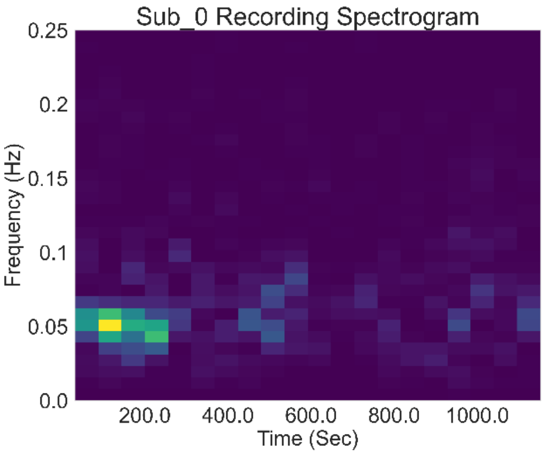

Fig. S-5 ***Recorded Data Spectrogram -*** *Spectrogram of a single channel of the HR-EGG recorded data for subject 0*

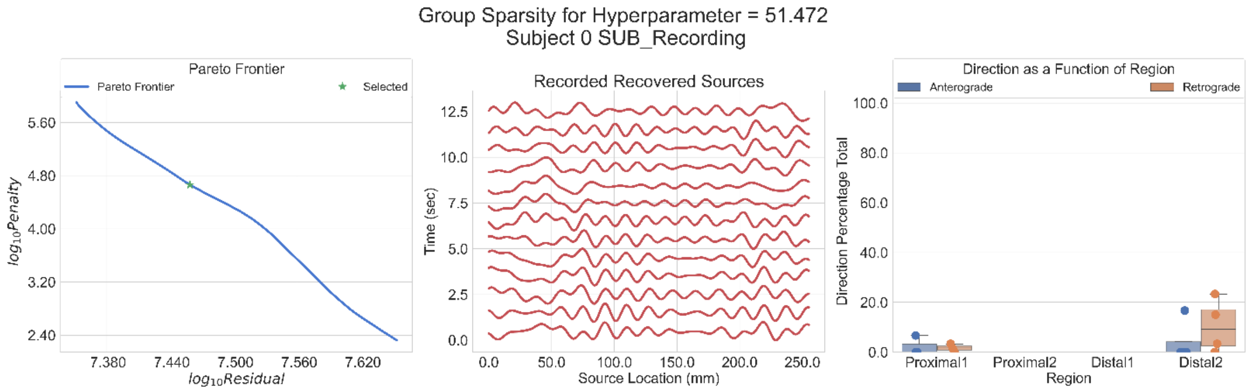

Fig. S-6 ***Subject 0 Recorded Data Results****– From left to right the pareto frontier with solution point selected, the recovered sources and the ground truth simulation, the directions computed from the recovered sources as a function of region*

Subject 1 – Healthy Control

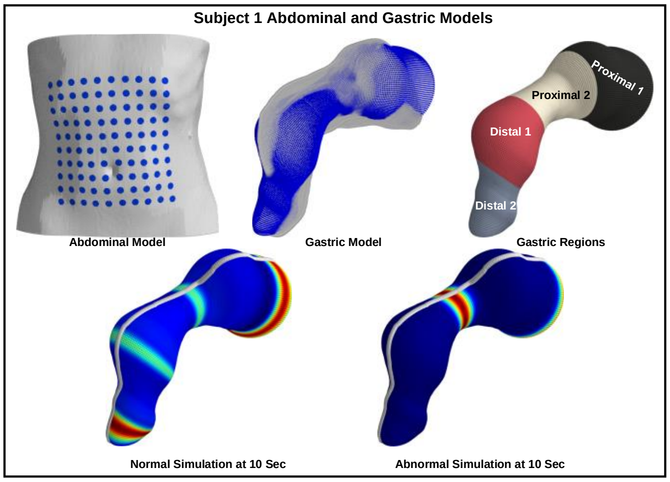

Fig. S-7 Subject 1 Abdominal and Gastric Surface 3D Models

Simulation Results

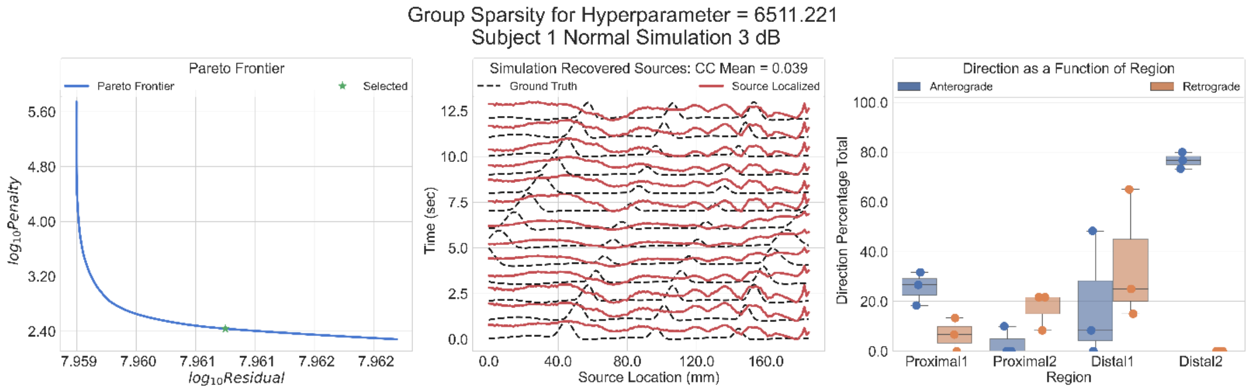

Fig. S-8 ***Subject 1 3.0 dB SNR Normal Simulation Results*** *– From left to right the pareto frontier with solution point selected, the recovered sources and the ground truth simulation, the directions computed from the recovered sources as a function of region. The average correlation coefficient across all time and all sources is 0.145*

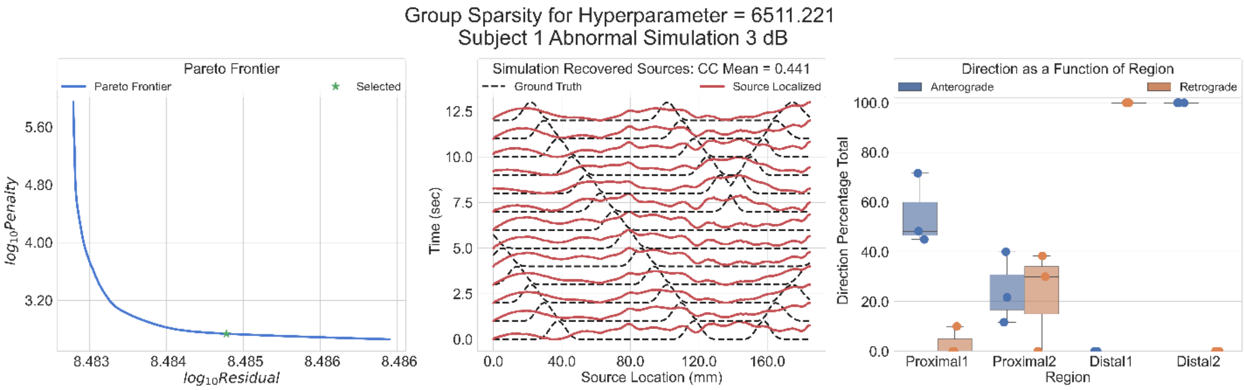

Fig. S-9 ***Subject 1 3.0 dB SNR Abnormal Simulation Results*** *– From left to right the pareto frontier with solution point selected, the recovered sources and the ground truth simulation, the directions computed from the recovered sources as a function of region. The average correlation coefficient across all time and all sources is 0.373*

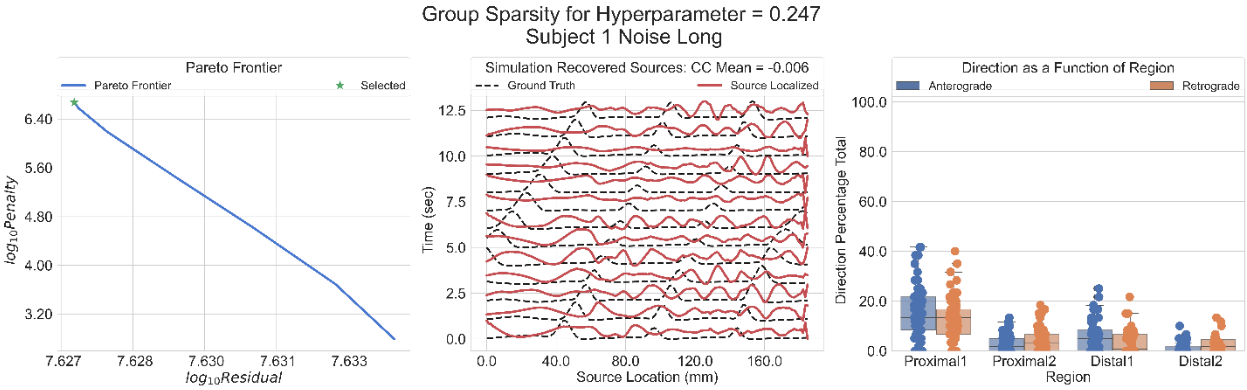

Fig. S-10 ***Subject 1 Noise Alone Observation Results*** *– From left to right, the pareto frontier with solution point identified, the recovered "sources" and the ground truth normal simulation that we compare against, the directions computed from the PGD of the recovered sources. The average correlation coefficient across all time and all spatial sources is -0.006*

Recording Results

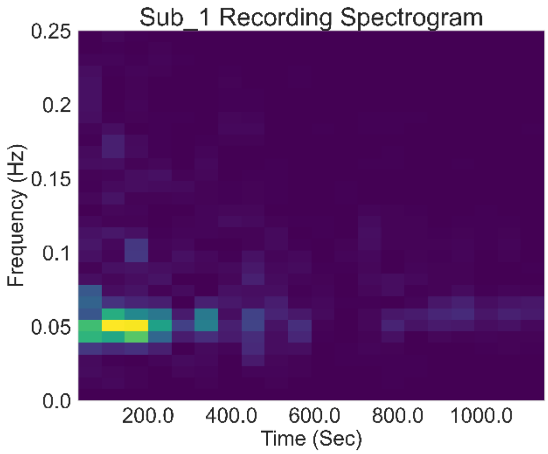

Fig. S-11 ***Recorded Data Spectrogram -*** *Spectrogram of a single channel of the HR-EGG recorded data for subject 1*

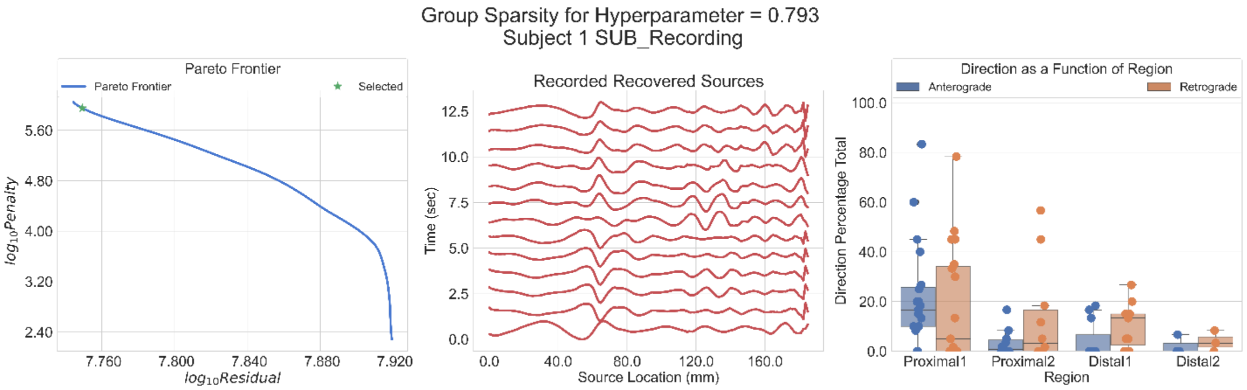

Fig. S-12 ***Subject 1 Recorded Data Results****– From left to right the pareto frontier with solution point selected, the recovered sources and the ground truth simulation, the directions computed from the recovered sources as a function of region.*

Subject 2 – Unhealthy: Severe Idiopathic Gastroparesis

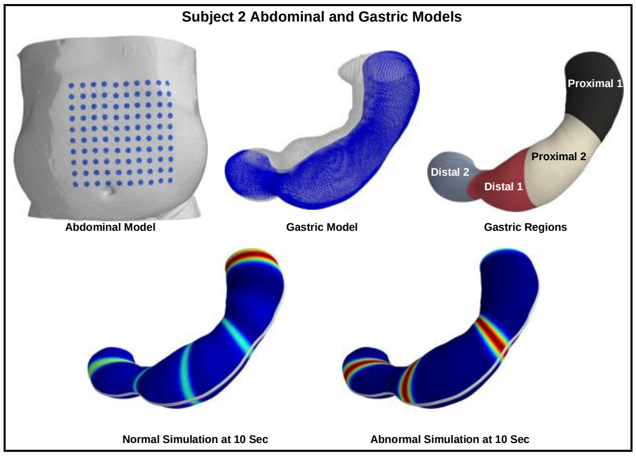

Fig. S-13 Subject 2 Abdominal and Gastric 3D Models

Simulation Results

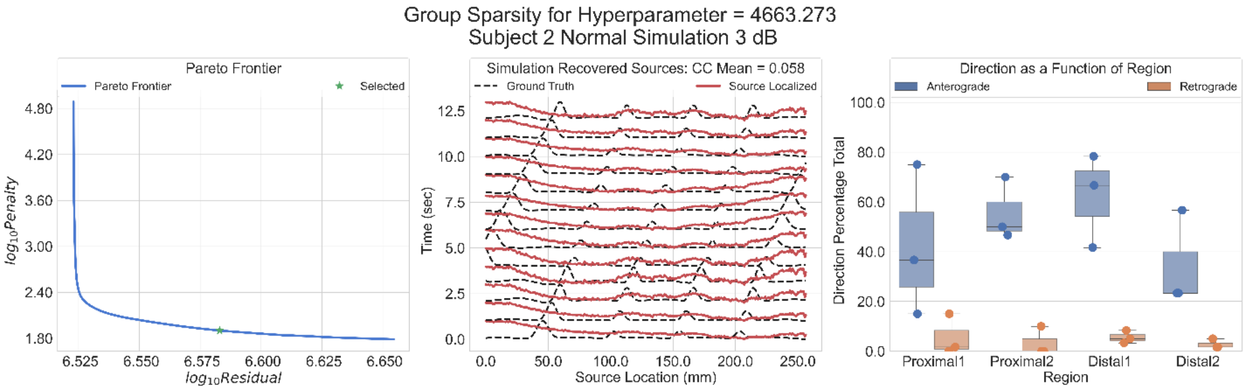

Fig. S-14 ***Subject 2 3.0 dB SNR Normal Simulation Results*** *– From left to right the pareto frontier with solution point selected, the recovered sources and the ground truth simulation, the directions computed from the recovered sources as a function of region. The average correlation coefficient across all time and all sources is 0.075*

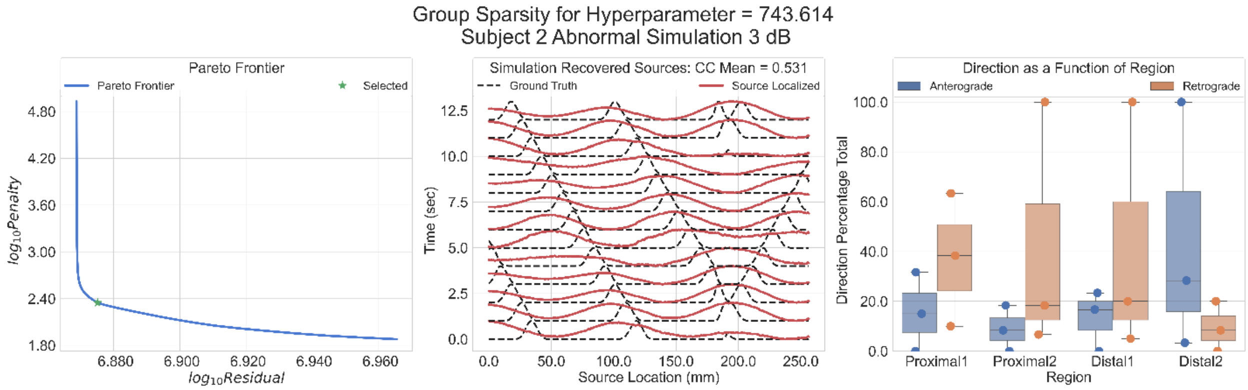

Fig. S-15 ***Subject 2 3.0 dB SNR Abnormal Simulation Results*** *– From left to right the pareto frontier with solution point selected, the recovered sources and the ground truth simulation, the directions computed from the recovered sources as a function of region. The average correlation coefficient across all time and all sources is 0.531*

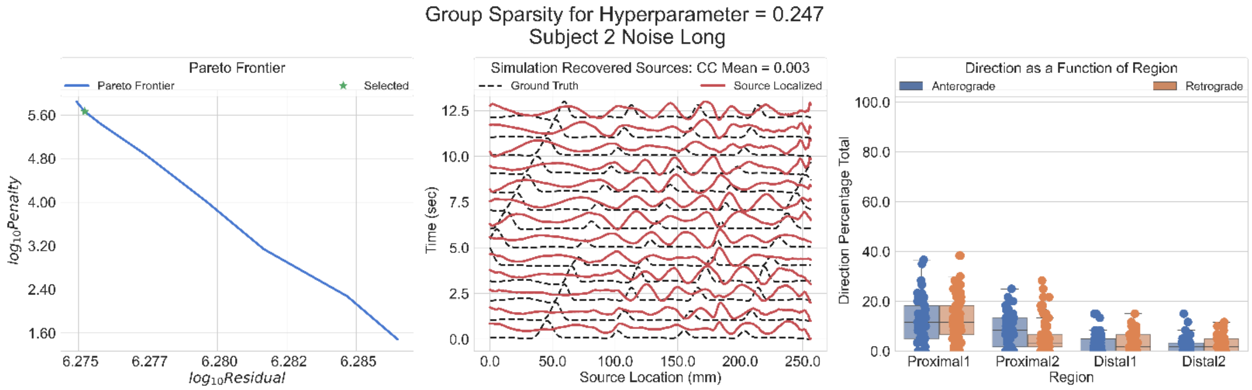

Fig. S-16 ***Subject 2 Noise Alone Observation Results*** *– From left to right, the pareto frontier with solution point identified, the recovered "sources" and the ground truth normal simulation that we compare against, the directions computed from the PGD of the recovered sources. The average correlation coefficient across all time and all spatial sources is 0.003*

Recorded Data Results

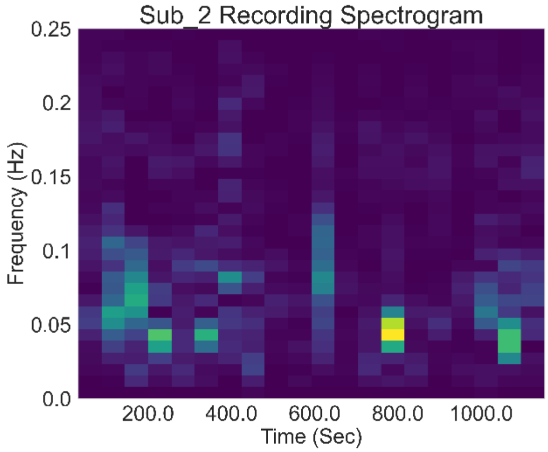

Fig. S-17 ***Recorded Data Spectrogram*** *- Spectrogram of a single channel of the HR-EGG recorded data for subject 2*

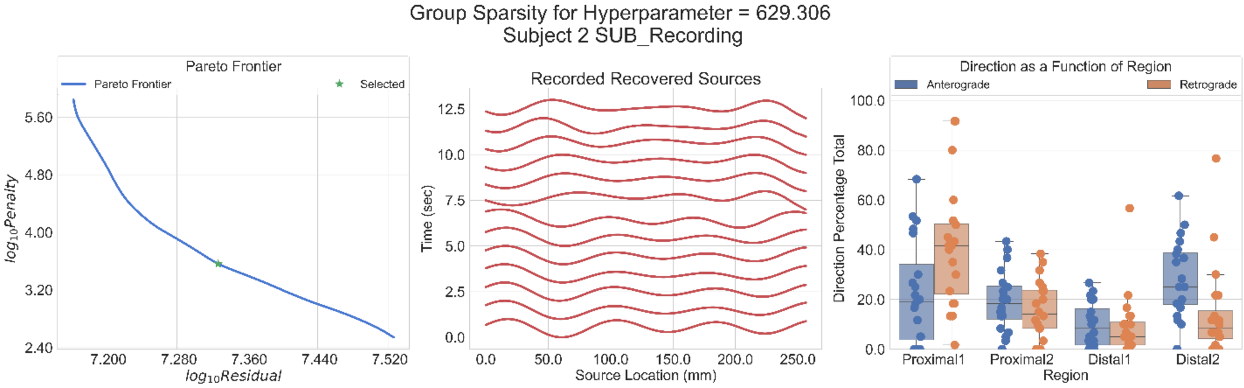

Fig. S-18 ***Subject 2 Recorded Data Results****– From left to right the pareto frontier with solution point selected, the recovered sources and the ground truth simulation, the directions computed from the recovered sources as a function of region.*

Subject 3 – Unhealthy: Early Diabetes

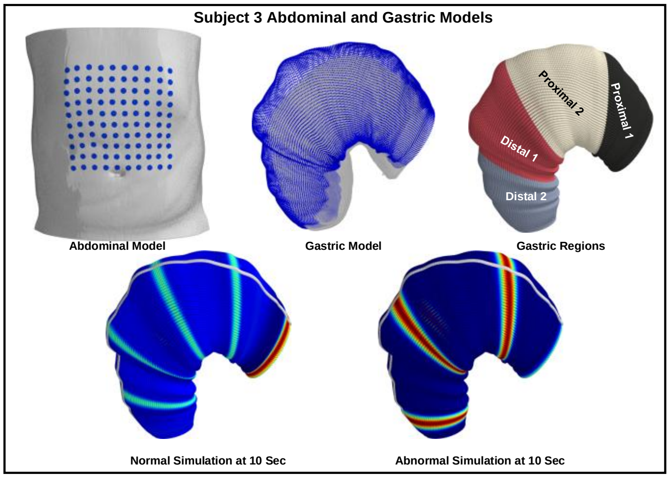

Fig. S-19 Subject 3 Abdominal and Gastric 3D Models

Subject Simulation Results

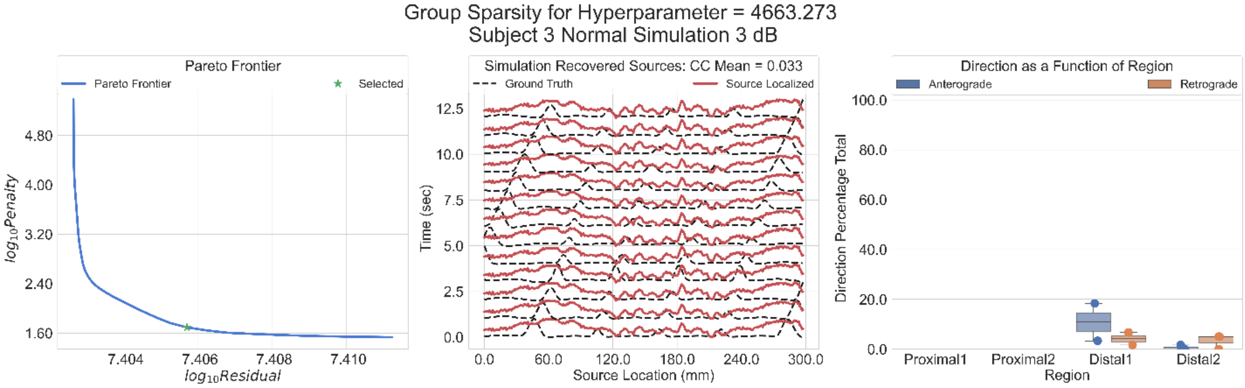

Fig. S-20 ***Subject 3 3.0 dB SNR Normal Simulation Results*** *– From left to right the pareto frontier with solution point selected, the recovered sources and the ground truth simulation, the directions computed from the recovered sources as a function of region. The average correlation coefficient across all time and all sources is 0.033*

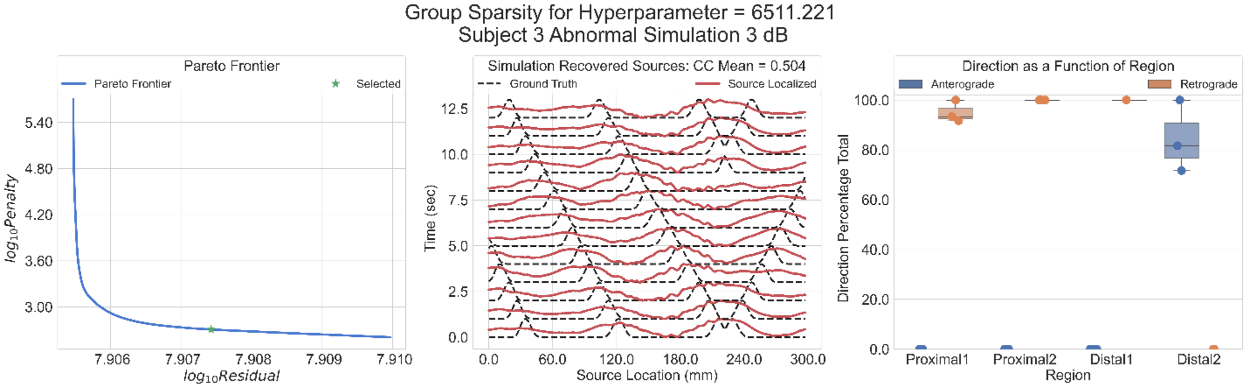

Fig. S-21 ***Subject 3 3.0 dB SNR Abnormal Simulation Results*** *– From left to right the pareto frontier with solution point selected, the recovered sources and the ground truth simulation, the directions computed from the recovered sources as a function of region. The average correlation coefficient across all time and all sources is 0.504*

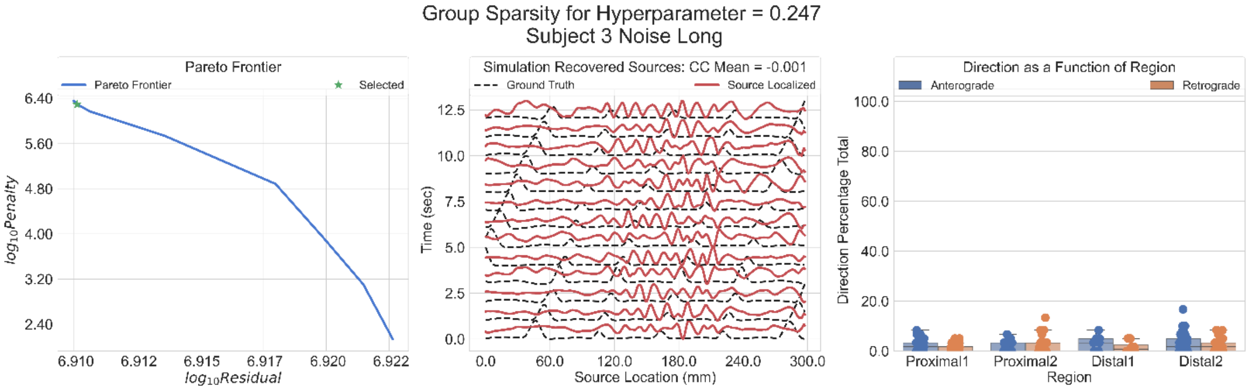

Fig. S-22 ***Subject 3 Noise Alone Observation Results –*** *From left to right, the pareto frontier with solution point identified, the recovered "sources" and the ground truth normal simulation that we compare against, the directions computed from the PGD of the recovered sources. The average correlation coefficient across all time and all spatial sources is -0.001*

Recorded Data Results

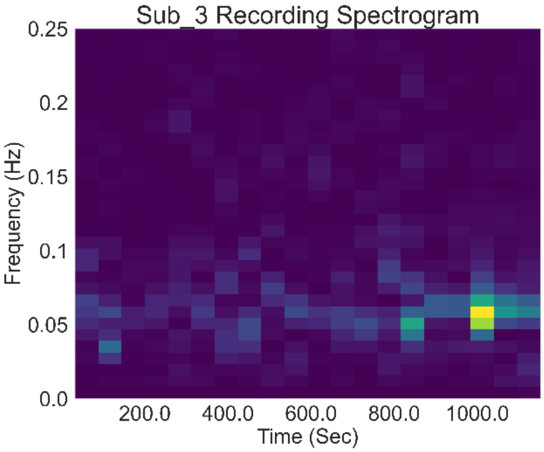

Fig. S-23 ***Recorded Data Spectrogram*** *- Spectrogram of a single channel of the HR-EGG recorded data for subject 3*

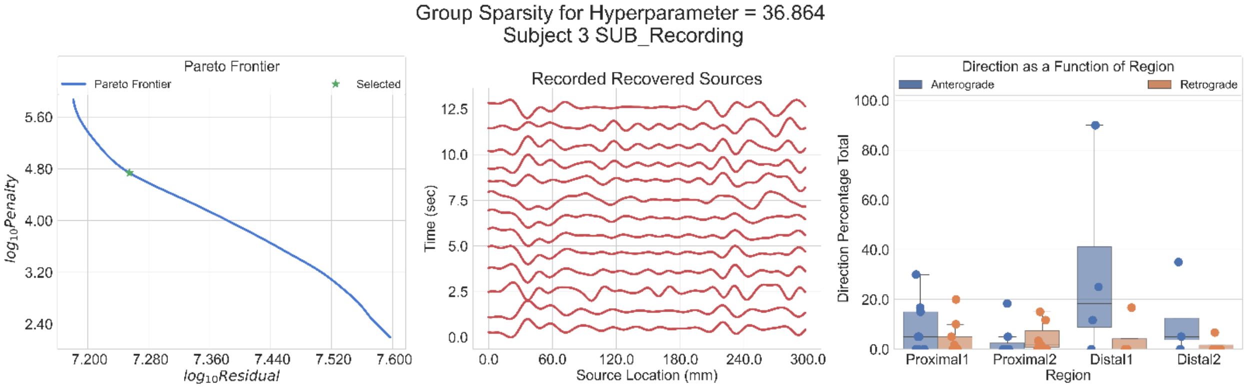

Fig. S-24 ***Subject 3 Recorded Data Results****– From left to right the pareto frontier with solution point selected, the recovered sources and the ground truth simulation, the directions computed from the recovered sources as a function of region.*

Subject 4 – Unhealthy: Diabetic Gastroparesis

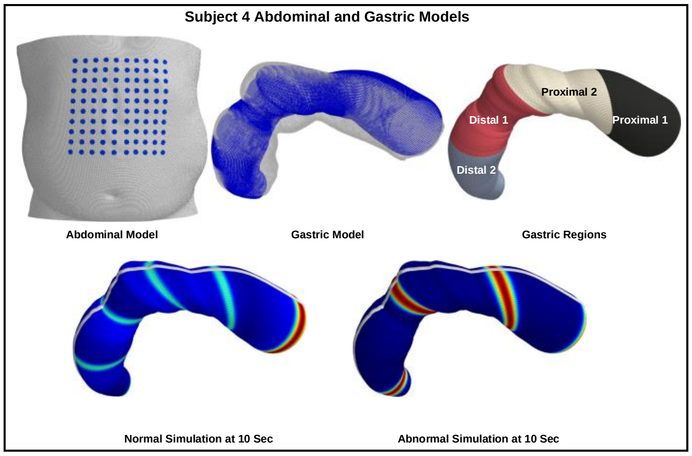

Fig. S-25 Subject 4 Abdominal and Gastric 3D Models

Subject Simulation Results

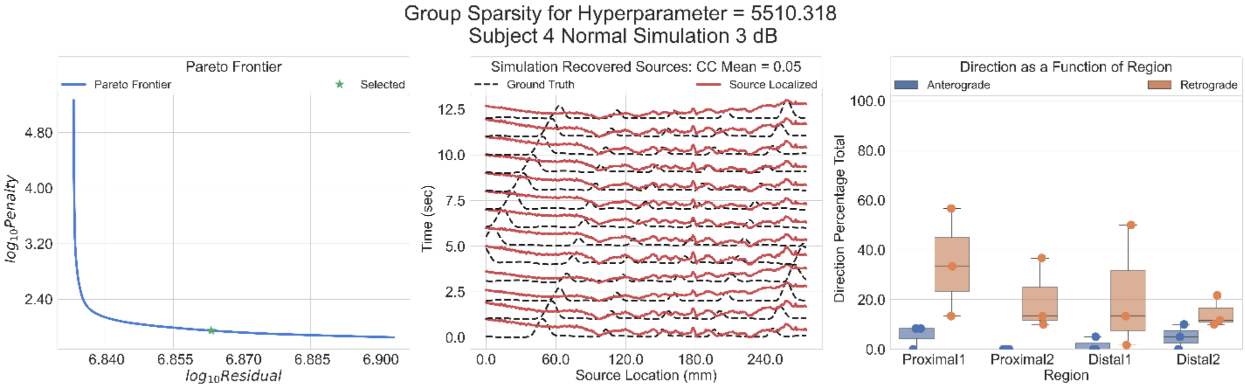
Group Sparsity for Hyperparameter = 5510.318
Subject 4 Normal Simulation 3 dB

Fig. S-26 ***Subject 4 3.0 dB SNR Normal Simulation Results*** *– From left to right the pareto frontier with solution point selected, the recovered sources and the ground truth simulation, the directions computed from the recovered sources as a function of region. The average correlation coefficient across all time and all sources is 0.05*

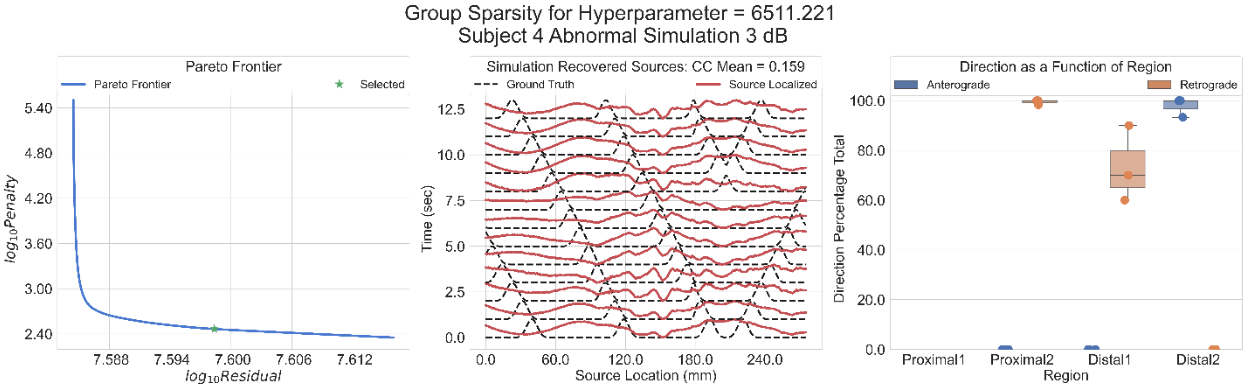
Group Sparsity for Hyperparameter = 6511.221
Subject 4 Abnormal Simulation 3 dB

Fig. S-27 ***Subject 4 3.0 dB SNR Abnormal Simulation Results*** *– From left to right the pareto frontier with solution point selected, the recovered sources and the ground truth simulation, the directions computed from the recovered sources as a function of region. The average correlation coefficient across all time and all sources is 0.159*

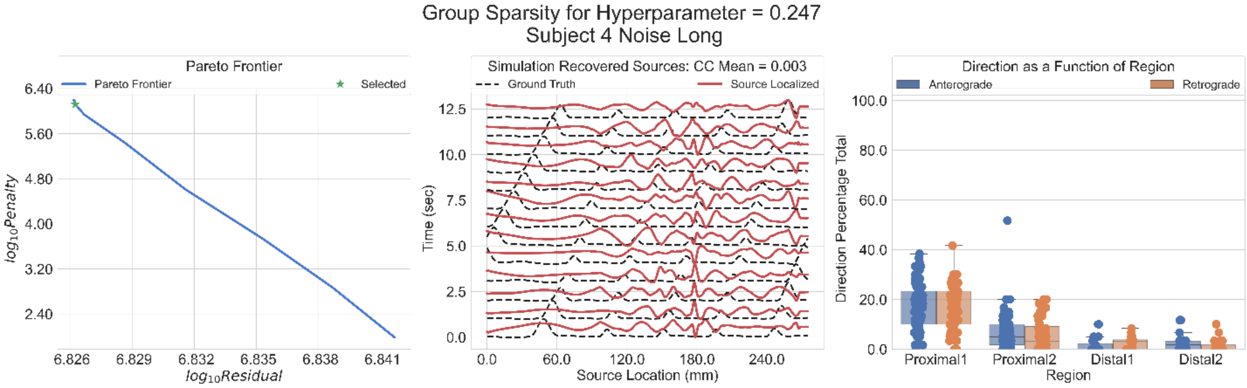
Group Sparsity for Hyperparameter = 0.247
Subject 4 Noise Long

Fig. S-28 ***Subject 4 Noise Alone Observation Results –*** *From left to right, the pareto frontier with solution point identified, the recovered "sources" and the ground truth normal simulation that we compare against, the directions computed from the PGD of the recovered sources. The average correlation coefficient across all time and all spatial sources is 0.003*

Recorded Data Results

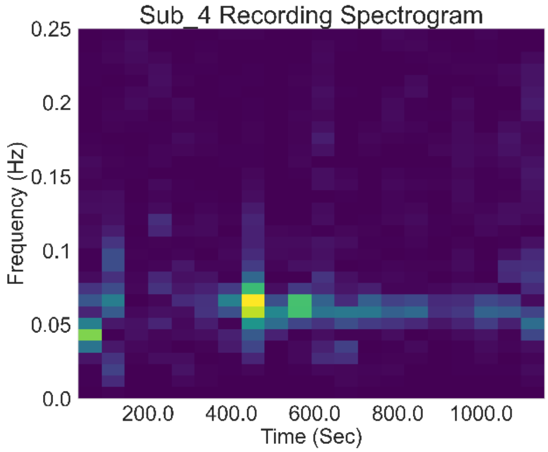

Fig. S-29 ***Recorded Data Spectrogram*** *- Spectrogram of a single channel of the HR-EGG recorded data for subject 4*

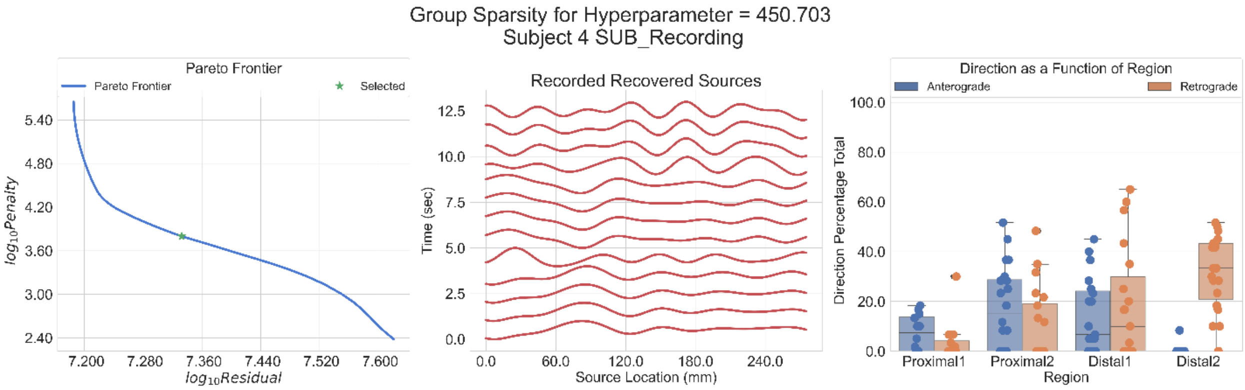

Fig. S-30 ***Subject 4 Recorded Data Results****– From left to right the pareto frontier with solution point selected, the recovered sources and the ground truth simulation, the directions computed from the recovered sources as a function of region.*

Subject 5 – Healthy Control

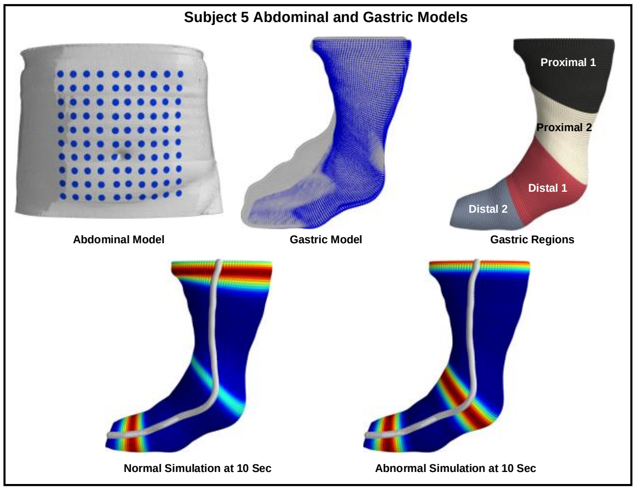

Fig. S-31 Subject 5 Abdominal and Gastric 3D Models

Subject Simulation Results

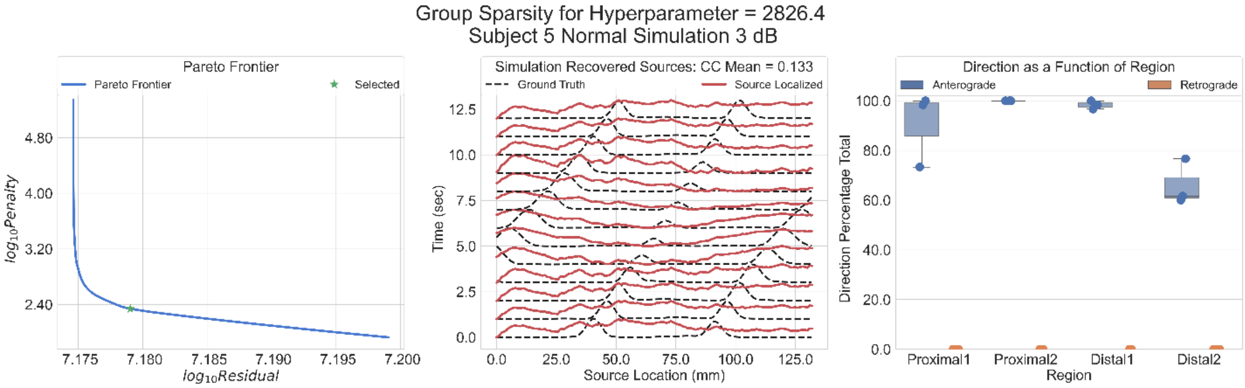

Fig. S-32 ***Subject 5 3.0 dB SNR Normal Simulation Results*** *– From left to right the pareto frontier with solution point selected, the recovered sources and the ground truth simulation, the directions computed from the recovered sources as a function of region. The average correlation coefficient across all time and all sources is 0.133*

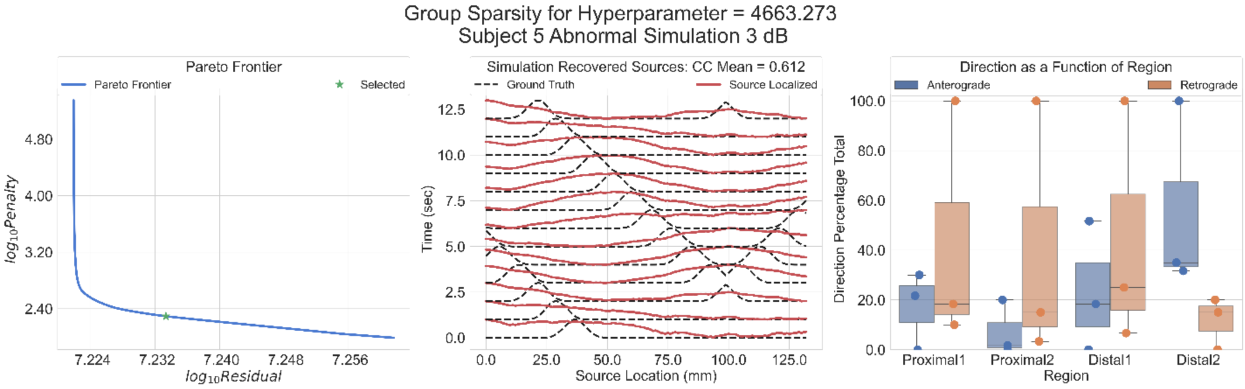

Fig. S-33 ***Subject 5 3.0 dB SNR Abnormal Simulation Results*** *– From left to right the pareto frontier with solution point selected, the recovered sources and the ground truth simulation, the directions computed from the recovered sources as a function of region. The average correlation coefficient across all time and all sources is 0.612*

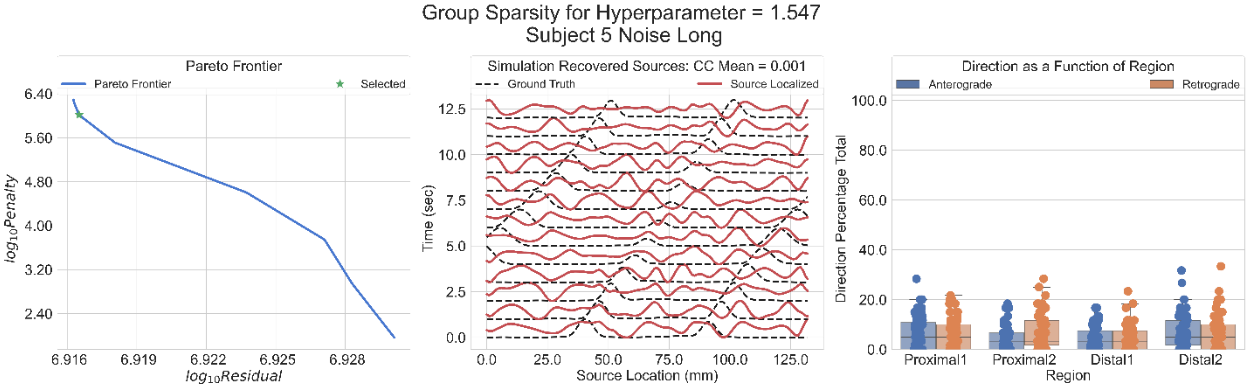

Fig. S-34 ***Subject 5 Noise Alone Observation Results –*** *From left to right, the pareto frontier with solution point identified, the recovered "sources" and the ground truth normal simulation that we compare against, the directions computed from the PGD of the recovered sources. The average correlation coefficient across all time and all spatial sources is 0.001*

Recorded Data Results

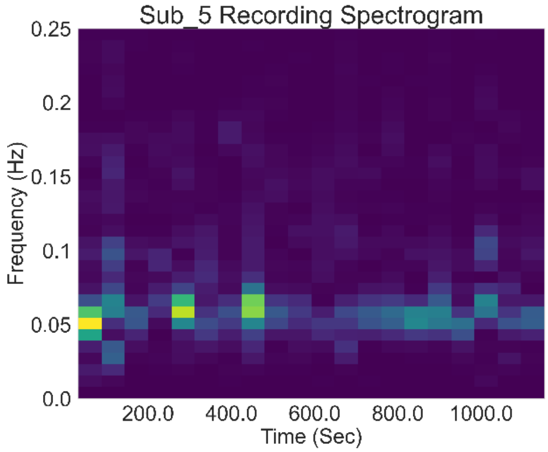

Fig. S-35 ***Recorded Data Spectrogram*** *- Spectrogram of a single channel of the HR-EGG recorded data for subject 5*

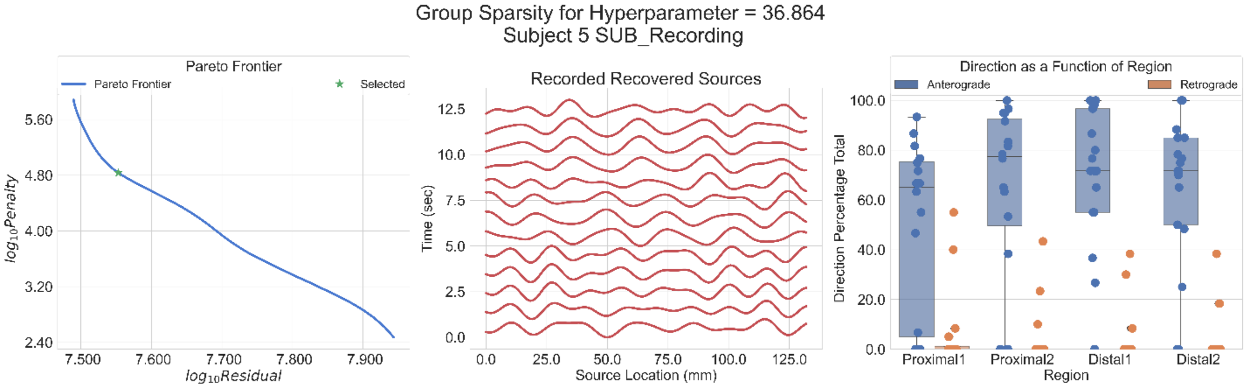

Fig. S-36 ***Subject 5 Recorded Data Results****– From left to right the pareto frontier with solution point selected, the recovered sources and the ground truth simulation, the directions computed from the recovered sources as a function of region.*

Subject 6 – Healthy Control

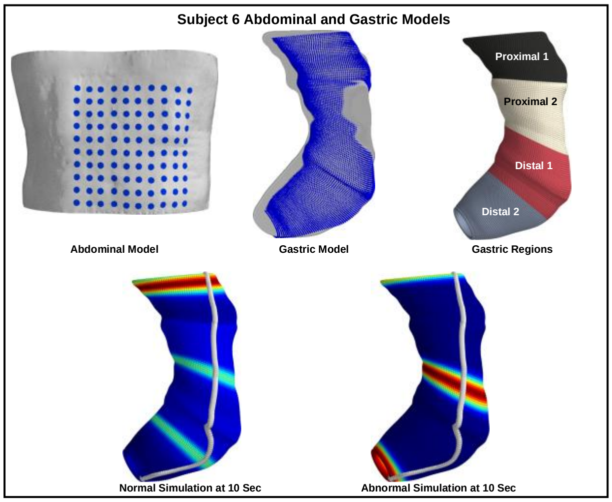

Fig. S-37 Subject 6 Abdominal and Gastric 3D Models

Subject Simulation Results

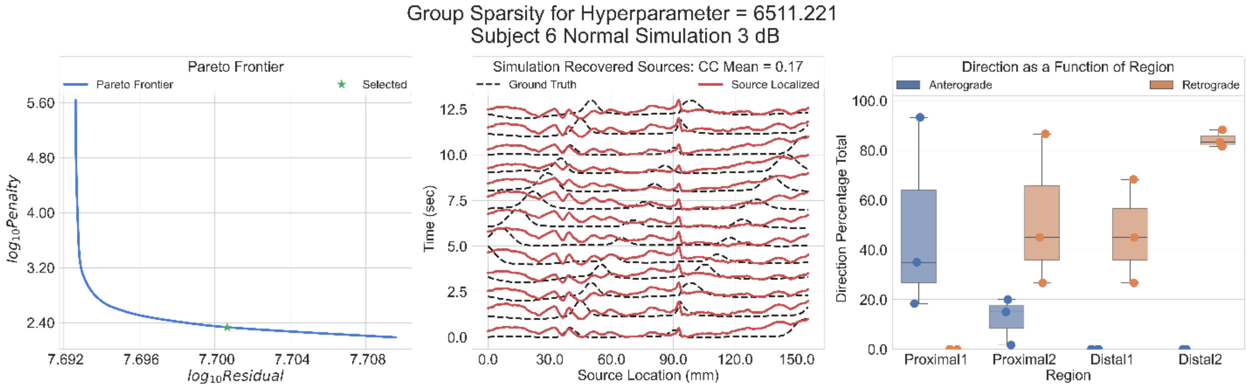

Fig. S-38 ***Subject 6 3.0 dB SNR Normal Simulation Results*** *– From left to right the pareto frontier with solution point selected, the recovered sources and the ground truth simulation, the directions computed from the recovered sources as a function of region. The average correlation coefficient across all time and all sources is 0.17*

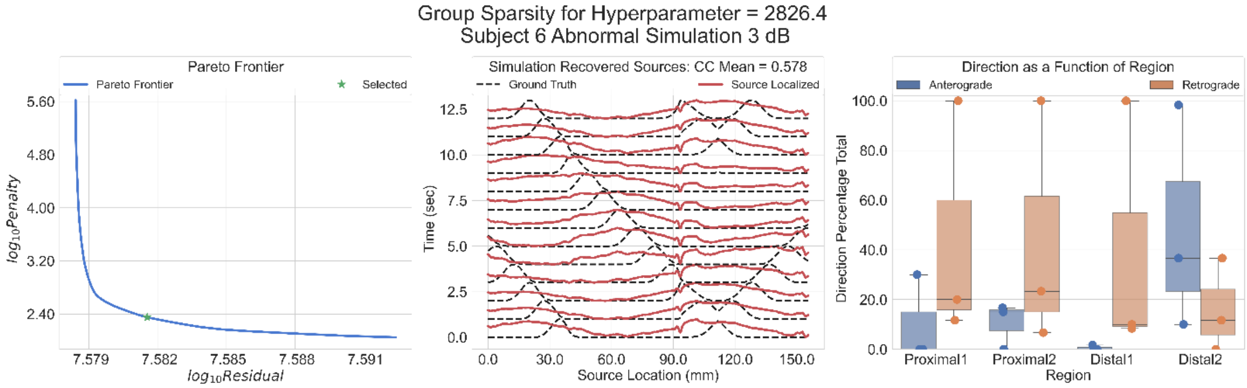

Fig. S-39 ***Subject 6 3.0 dB SNR Abnormal Simulation Results*** *– From left to right the pareto frontier with solution point selected, the recovered sources and the ground truth simulation, the directions computed from the recovered sources as a function of region. The average correlation coefficient across all time and all sources is 0.578*

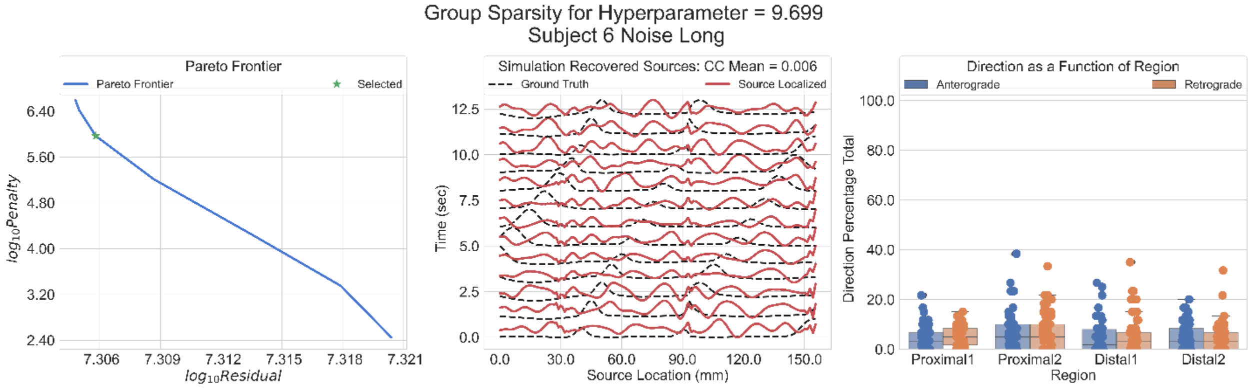

Fig. S-40 ***Subject 6 Noise Alone Observation Results –*** *From left to right, the pareto frontier with solution point identified, the recovered "sources" and the ground truth normal simulation that we compare against, the directions computed from the PGD of the recovered sources. The average correlation coefficient across all time and all spatial sources is 0.006*

Recorded Data Results

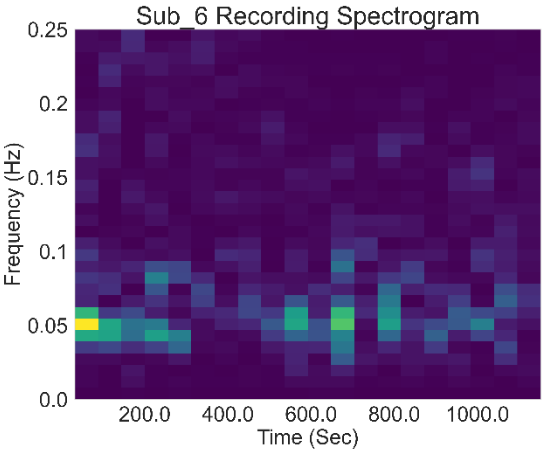

Fig. S-41 ***Recorded Data Spectrogram -*** *Spectrogram of a single channel of the HR-EGG recorded data for subject 6*

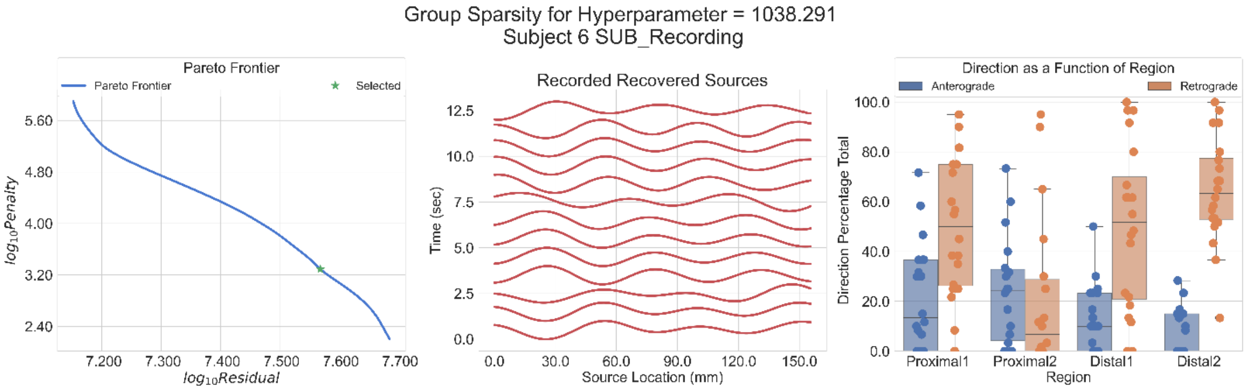

Fig. S-42 ***Subject 6 Recorded Data Results****– From left to right the pareto frontier with solution point selected, the recovered sources and the ground truth simulation, the directions computed from the recovered sources as a function of region.*

Histograms and Distributions for P-Value Computation

Correlation Coefficient

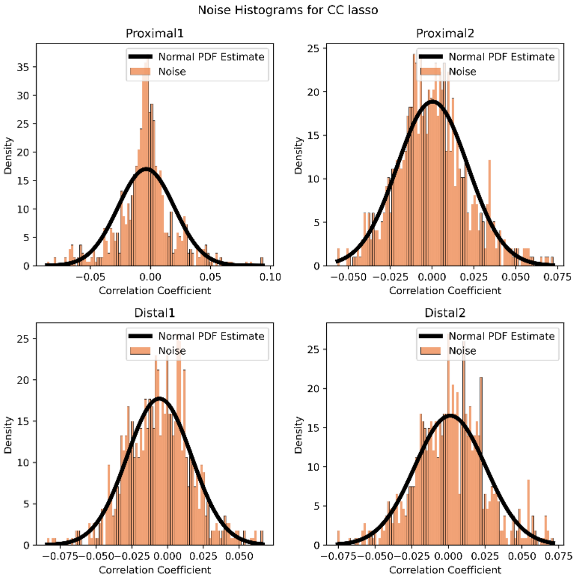

Fig. S-44 ***LKS Correlation Coefficient Distribution Estimates-*** *The histograms and density estimates for the correlation coefficients based on the noise alone simulation. The distribution estimate is made for each gastric region.*

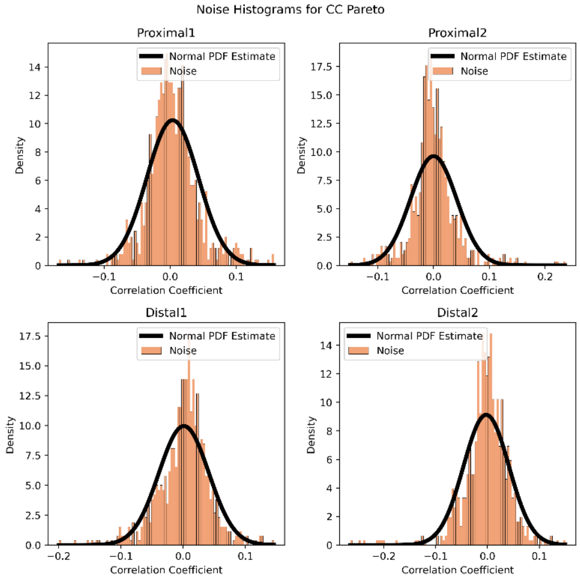

Fig. S-43 ***Group Sparsity Correlation Coefficient Distribution Estimates-*** *The histograms and density estimates for the correlation coefficients based on the noise alone simulation. The distribution estimate is made for each gastric region.*

PGD Percentage

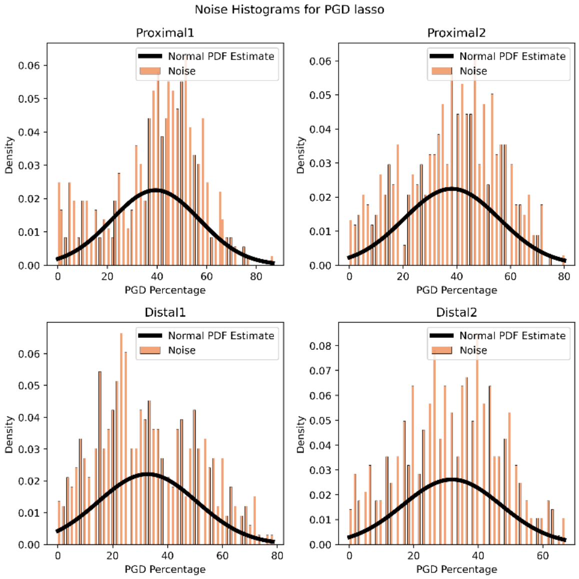

Fig. S-45 ***LKS PGD Percentage Distribution Estimates-*** *The histograms and density estimates for the percent of samples for which PGD > 0.75 based on the noise alone simulation. The distribution estimate is made for each gastric region.*

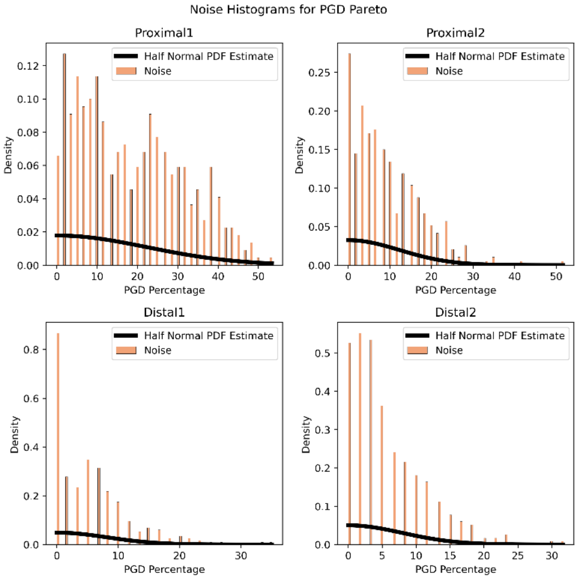

Fig. S-46 ***Group Sparsity PGD Percentage Distribution Estimates-*** *The histograms and density estimates for the percent of samples for which PGD > 0.75 based on the noise alone simulation. The distribution estimate is made for each gastric region.*

Appendix C

Chapter 3 Supplemental Materials

Overview

In these supplementary materials we present the results for:

- Abnormal simulation results
- Subject 1 Results:
  - Average CC and P-Values
  - PGD Percentages
  - 3D Models and recovered sources
- Noise histograms for p-value computations

Abnormal Simulation Results

PGD Results

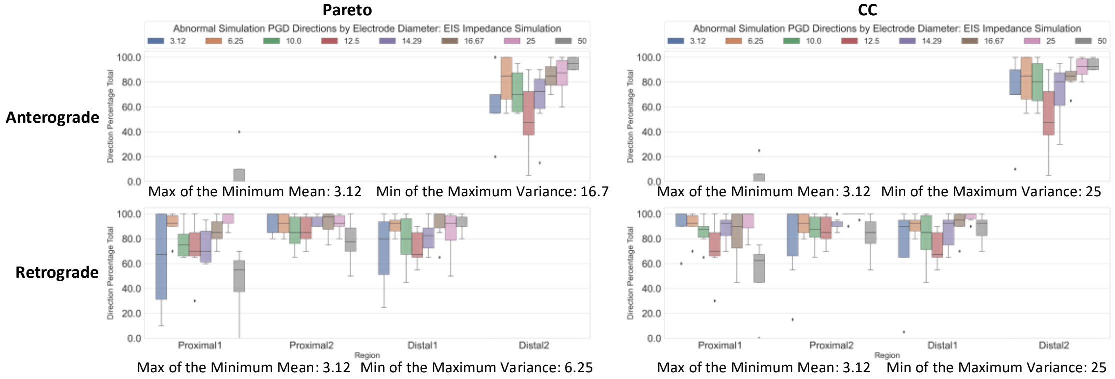

S- 1 PGD Results for the Abnormal Simulation

Table S- 1 Percent of Samples with PGD > 0.75 for each region, diameter and subject.

EIS Model	**Sub_0**				**Sub_1**			
Diam(mm)	**Prox 1**	**Prox 2**	**Distal1**	**Distal2**	**Prox 1**	**Prox 2**	**Distal1**	**Distal2**
3.12	100	100	95	80	60	56.667	35	50
6.25	95	88.333	91.667	75	86.667	95	90	100
10	93.333	91.667	86.667	81.667	76.667	81.667	73.333	65
12.5	80	78.333	81.667	53.333	75	90	75	40
14.29	96.667	93.333	98.333	95	86.667	95	85	65
16.67	98.333	100	98.333	93.333	73.333	98.333	91.667	88.333
25	100	100	98.333	95	83.333	93.333	76.667	68.333
50	60	81.667	86.667	95	0	90	90	90
Variance Model								
3.12	83.333	95	91.667	91.667	72.5	71.667	63.333	43.333
6.25	93.333	93.333	93.333	73.333	88.333	90	80	81.667
10	91.667	95	85	86.667	55	90	65	80
12.5	80	83.333	88.333	73.333	80	85	81.667	73.333
14.29	100	96.667	93.333	75	81.667	88.333	83.333	63.333
16.67	96.667	98.333	96.667	81.667	73.333	86.667	75	63.333
25	98.333	98.333	96.667	93.333	53.333	80	91.667	60
50	56.667	81.667	73.333	90	0	90	93.333	85

Abnormal Correlation Coefficient and Error Results

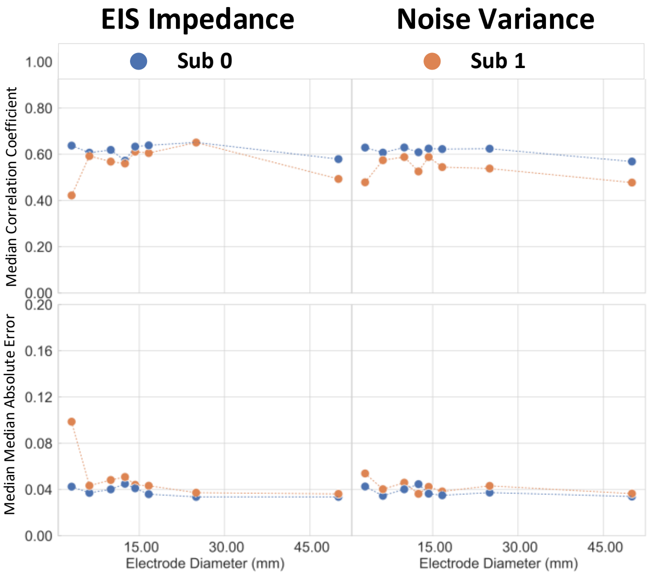

S- 2 Error and Correlation coefficient results for both subjects, abnormal simulation

Table S- 2 Correlation coefficients and associated p-values for subject 0 abnormal simulation

EIS Model	**Subject 0**							
	Proximal1		**Proximal2**		**Distal1**		**Distal2**	
Diam (mm)	**CC**	**P**	**CC**	**P**	**CC**	**P**	**CC**	**P**
3.12	0.611	0	0.568	0	0.692	0	0.712	0
6.25	0.625	0	0.542	0	0.662	0	0.679	0
10	0.6	0	0.563	0	0.663	0	0.676	0
12.5	0.569	0	0.514	0.001	0.645	0	0.622	0
14.29	0.569	0	0.559	0	0.687	0	0.717	0
16.67	0.63	0	0.546	0	0.695	0	0.714	0
25	0.629	0	0.599	0	0.701	0	0.732	0
50	0.453	0.002	0.485	0.001	0.573	0	0.626	0
Variance Model								
	Subject 0							
	Proximal1		**Proximal2**		**Distal1**		**Distal2**	
Diam (mm)	**CC**	**P**	**CC**	**P**	**CC**	**P**	**CC**	**P**
3.12	0.6	0	0.561	0	0.7	0	0.677	0
6.25	0.597	0	0.575	0	0.643	0	0.648	0
10	0.611	0	0.567	0	0.687	0	0.696	0
12.5	0.577	0	0.538	0.001	0.663	0	0.679	0
14.29	0.614	0	0.573	0	0.648	0	0.675	0
16.67	0.61	0	0.561	0	0.677	0	0.694	0
25	0.606	0	0.559	0	0.655	0	0.675	0
50	0.388	0.004	0.476	0.002	0.563	0	0.599	0

Table S- 3 Correlation coefficient results and associated p-values for subject 1 abnormal simulation

EIS Model	**Subject 1**							
	Proximal1		**Proximal2**		**Distal1**		**Distal2**	
Diameter (mm)	**CC**	**P**	**CC**	**P**	**CC**	**P**	**CC**	**P**
3.12	0.323	0.022	0.347	0.017	0.514	0.001	0.443	0.002
6.25	0.511	0.001	0.602	0	0.632	0	0.566	0
10	0.509	0.001	0.527	0.001	0.645	0	0.602	0
12.5	0.483	0.001	0.574	0	0.652	0	0.545	0
14.29	0.502	0.001	0.556	0	0.68	0	0.559	0
16.67	0.421	0.004	0.569	0	0.683	0	0.623	0
25	0.558	0	0.614	0	0.709	0	0.647	0
50	0.104	0.255	0.569	0	0.497	0.002	0.492	0.001
Variance Model								
	Subject 1							
	Proximal1		**Proximal2**		**Distal1**		**Distal2**	
Diameter (mm)	**CC**	**P**	**CC**	**P**	**CC**	**P**	**CC**	**P**
3.12	0.326	0.013	0.49	0.001	0.637	0	0.471	0.001
6.25	0.456	0.001	0.59	0	0.608	0	0.593	0
10	0.513	0	0.566	0	0.68	0	0.626	0
12.5	0.36	0.007	0.597	0	0.534	0.001	0.52	0
14.29	0.516	0	0.587	0	0.636	0	0.594	0
16.67	0.443	0.001	0.575	0	0.564	0	0.573	0
25	0.368	0.006	0.561	0	0.599	0	0.554	0
50	0.098	0.235	0.58	0	0.485	0.002	0.482	0.001

Subject 0 Abnormal Simulation Recovered Source Results

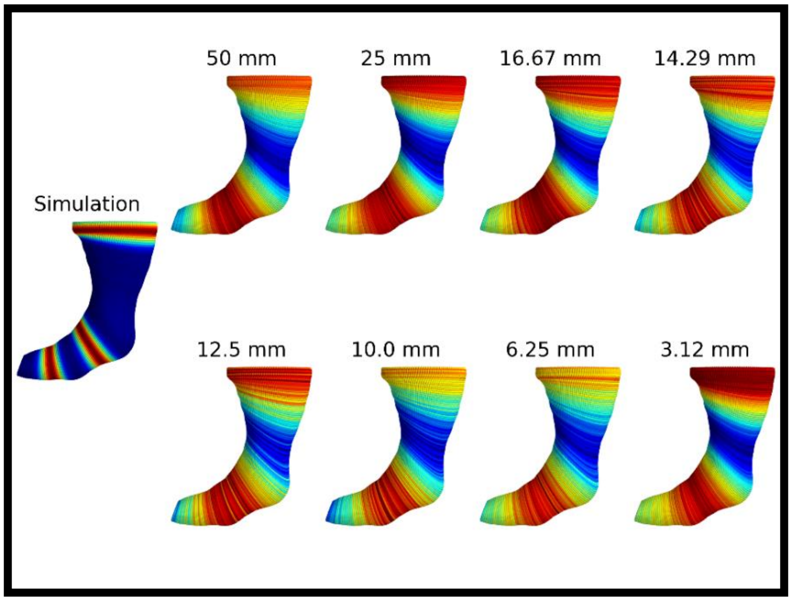

S- 3 Subject 0 abnormal simulation recovered sources mapped to 3D model for the EIS noise model

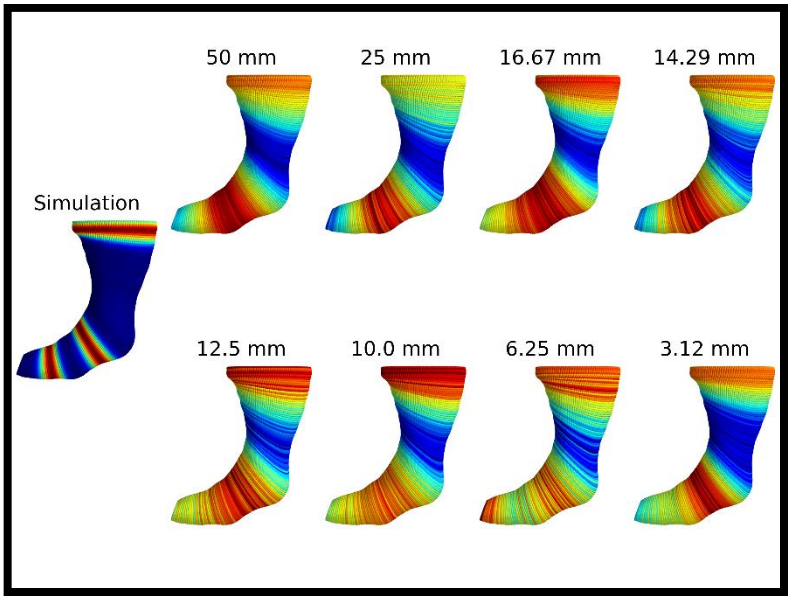

S- 4 Subject 0 abnormal simulation recovered sources mapped to 3D model for the variance noise model

Subject 1 Abnormal Simulation Recovered Source Results

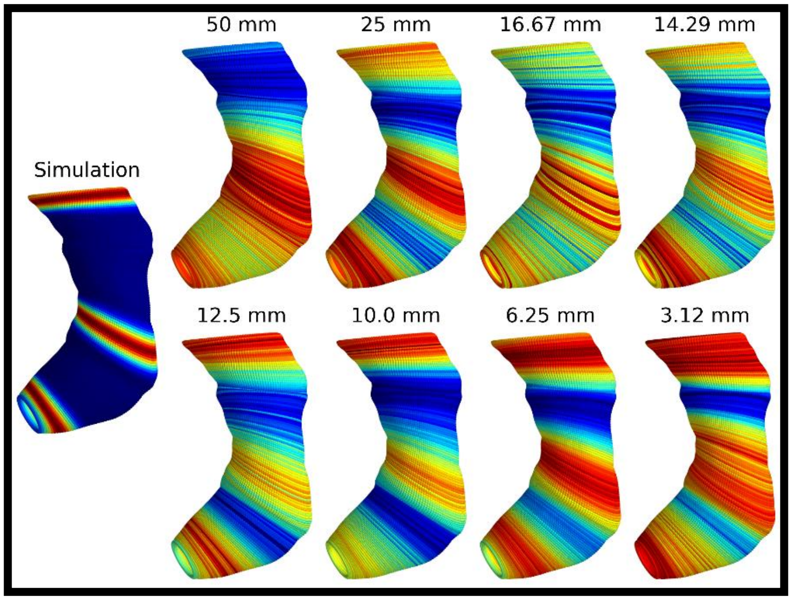

S- 5 Subject 1 abnormal simulation recovered sources mapped to 3D model for the EIS noise model

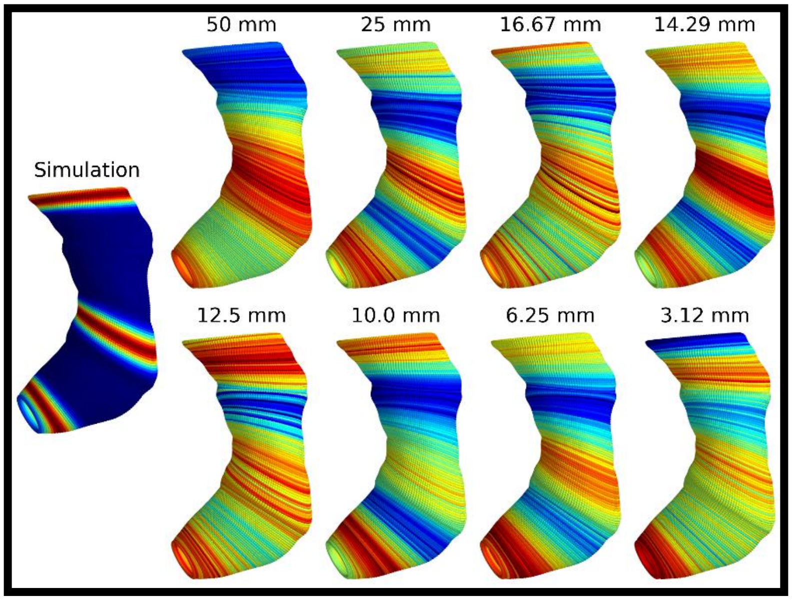

S- 6 Subject 1 abnormal simulation recovered sources mapped to 3D model for the variance noise model

Subject 1 Normal Simulation Recovered Source Results

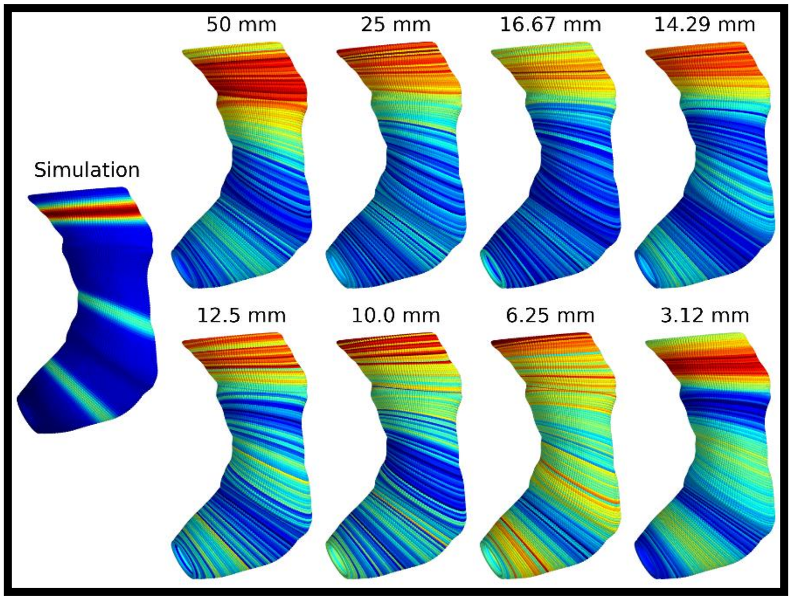

S- 7 Subject 1 normal simulation recovered sources mapped to 3D model for the EIS noise model

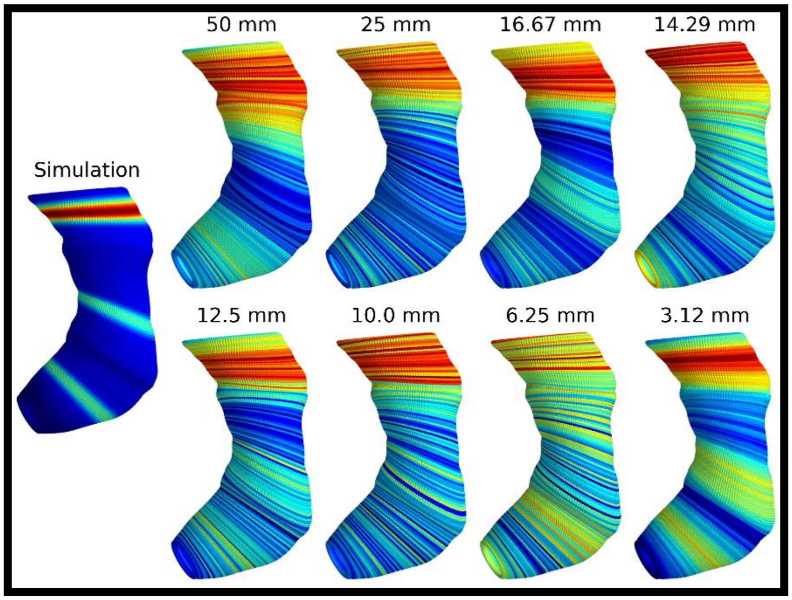

S- 8 Subject 1 normal simulation recovered sources mapped to 3D model for the variance noise model

Noise Histograms For the EIS Model

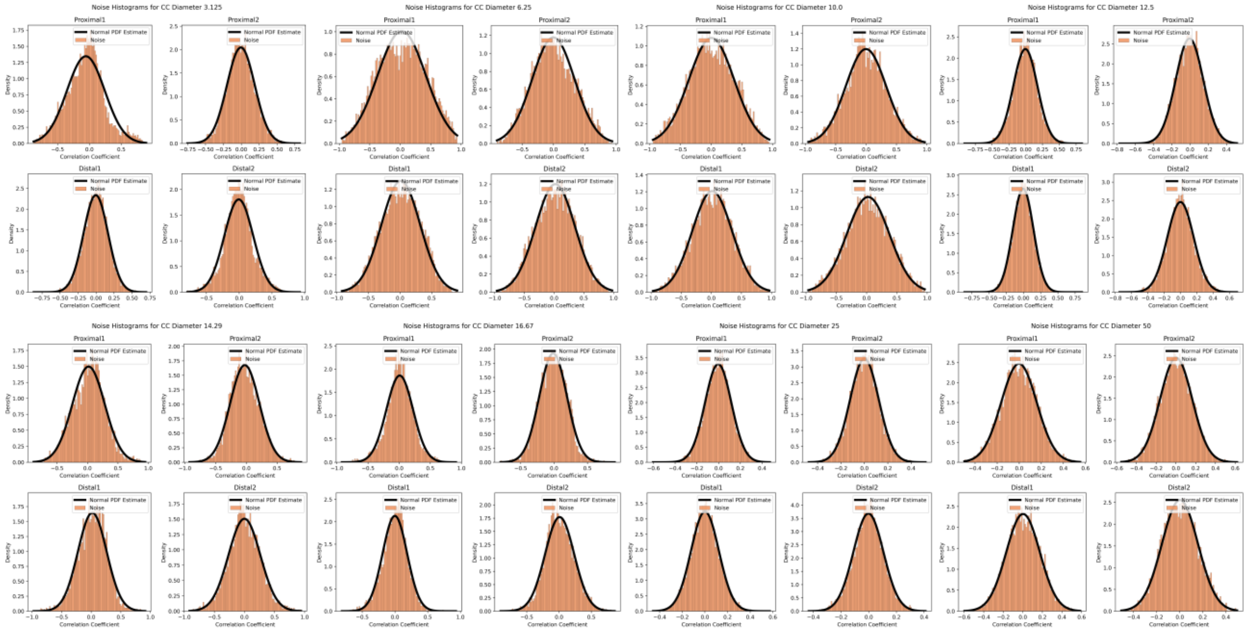

S- 9 Noise histograms and distribution estimates for the EIS model, all electrode diameters, all gastric regions

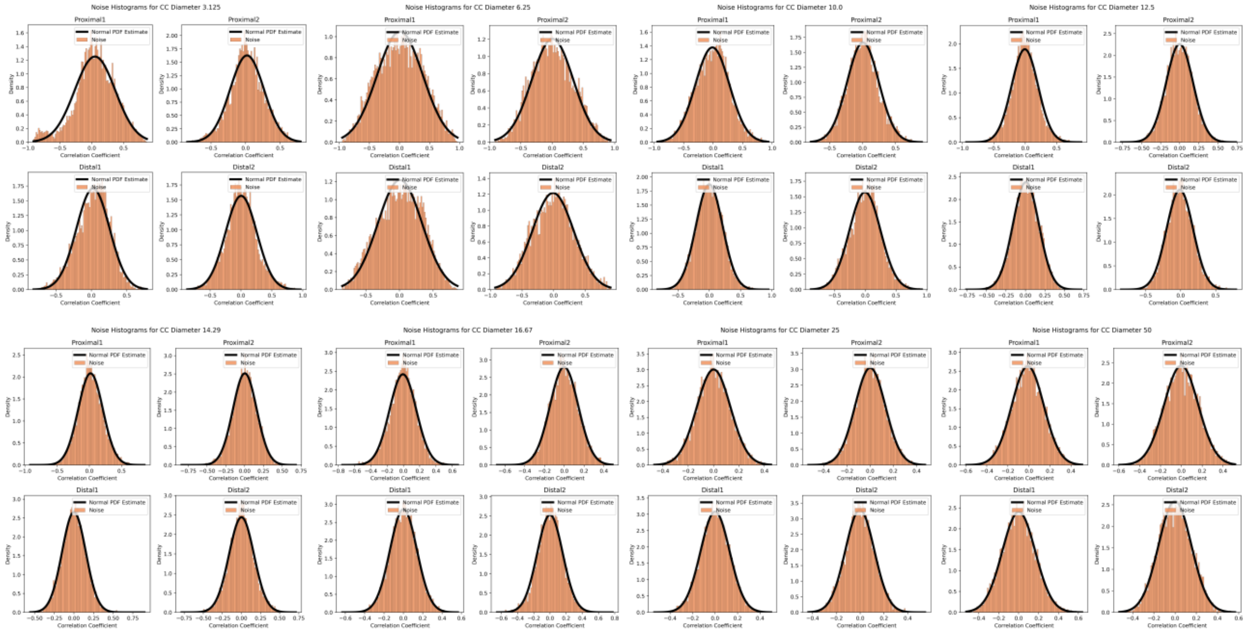

S- 10 Noise histograms and distribution estimates for the Variance model, all electrode diameters, all gastric regions

Bibliography

[1] R. Brun and B. Kuo, “Functional dyspepsia,” *Therapeutic advances in gastroenterology*, vol. 3, no. 3, pp. 145–164, 2010.

[2] A. Gikas and J. K. Triantafillidis, “The role of primary care physicians in early diagnosis and treatment of chronic gastrointestinal diseases,” *Int. J. Gen. Med.*, vol. 7, pp. 159–173, Mar. 2014.

[3] Z. S. Heetun and E. M. Quigley, “Gastroparesis and parkinsons disease: a systematic review,” *Parkinsonism & related disorders*, vol. 18, no. 5, pp. 433–440, 2012.

[4] M. Horowitz, Y.-C. Su, C. K. Rayner, and K. L. Jones, “Gastroparesis: prevalence, clinical significance and treatment,” *Canadian Journal of Gastroenterology and Hepatology*, vol. 15, no. 12, pp. 805–813, 2001.

[5] P. J. Pasricha, R. Colvin, K. Yates, W. L. Hasler, T. L. Abell, A. Unalp-Arida, L. Nguyen, G. Farrugia, K. L. Koch, H. P. Parkman, W. J. Snape, L. Lee, J. Tonascia, and F. Hamilton, “Characteristics of patients with chronic unexplained nausea and vomiting and normal gastric emptying,” *Clin. Gastroenterol. Hepatol.*, vol. 9, no. 7, pp. 567–76.e1–4, Jul. 2011.

[6] P. Janssen, M. S. Harris, M. Jones, T. Masaoka, R. Farré, H. Törnblom, L. Van Oudenhove, M. Simrén, and J. Tack, “The relation between symptom improvement and gastric emptying in the treatment of diabetic and idiopathic gastroparesis,” *Am. J. Gastroenterol.*, vol. 108, no. 9, pp. 1382–1391, Sep. 2013.

[7] R. Corinaldesi, V. Stanghellini, C. Raiti, E. Rea, R. Salgemini, and L. Barbara, “Effect of chronic administration of cisapride on gastric emptying of a solid meal and on dyspeptic symptoms in patients with idiopathic gastroparesis,” *Gut*, vol. 28, no. 3, pp. 300–305, Mar. 1987.

[8] R. W. McCallum, O. Cynshi, and Investigative Team, “Clinical trial: effect of mitemcinal (a motilin agonist) on gastric emptying in patients with gastroparesis - a randomized, multicentre, placebo-controlled study,” *Aliment. Pharmacol. Ther.*, vol. 26, no. 8, pp. 1121–1130, Oct. 2007.

[9] M. E. Barton, T. Otiker, L. V. Johnson, D. C. Robertson, R. L. Dobbins, H. P. Parkman, P. M. Hellström, J. F. Tack, B. Kuo, A. Hobson, and G. E. Dukes, “70 a randomized, Double-Blind, Placebo-Controlled phase II study (MOT114479) to evaluate the safety and efficacy and dose response of 28 days of orally administered camicinal, a motilin receptor agonist, in diabetics with gastroparesis,” *Gastroenterology*, vol. 146, no. 5, pp. S–20, 2014.

[10] J. D. Huizinga and W. J. Lammers, “Gut peristalsis is governed by a multitude of cooperating mechanisms,” *American Journal of Physiology-Gastrointestinal and Liver Physiology*, vol. 296, no. 1, pp. G1–G8, 2009.

[11] G. O’Grady, P. Du, L. K. Cheng, J. U. Egbuji, W. J. Lammers, J. A. Windsor, and A. J. Pullan, “Origin and propagation of human gastric slow-wave activity defined by high-resolution mapping,” *American Journal of Physiology-Gastrointestinal and Liver Physiology*, vol. 299, no. 3, pp. G585–G592, 2010.

[12] G. O’Grady, T. R. Angeli, P. Du, C. Lahr, W. J. E. P. Lammers, J. A. Windsor, T. L. Abell, G. Farrugia, A. J. Pullan, and L. K. Cheng, “Abnormal initiation and conduction of slow-wave activity in gastroparesis, defined by high-resolution electrical mapping,” *Gastroenterology*, vol. 143, no. 3, pp. 589–98.e1–3, 2012.

[13] T. R. Angeli, L. K. Cheng, P. Du, T. H.-H. Wang, C. E. Bernard, M.-G. Vannucchi, M. S. Faussone-Pellegrini, C. Lahr, R. Vather, J. A. Windsor, G. Farrugia, T. L. Abell, and G. O’Grady, “Loss of interstitial cells of cajal and patterns of gastric dysrhythmia in patients with chronic unexplained nausea and vomiting,” *Gastroenterology*, vol. 149, no. 1, pp. 56–66.e5, 2015.

[14] T. L. Abell, W. D. Johnson, A. Kedar, J. M. Runnels, J. Thompson, E. S. Weeks, A. Minocha, and M. E. Griswold, “A double-masked, randomized, placebo-controlled trial of temporary endoscopic mucosal gastric electrical stimulation for gastroparesis,” *Gastrointestinal endoscopy*, vol. 74, no. 3, pp. 496–503, 2011.

[15] “Abstracts from the 8th annual meeting of the canadian neuromodulation society september 26-28, 2014 halifax, nova scotia, canada,” *Neuromodulation: Technology at the Neural Interface*, vol. 18, no. 1, pp. e1–e9, 2015.

[16] T. Abell, A. Kedar, A. Stocker, K. Beatty, L. McElmurray, M. Hughes, H. Rashed, W. Kennedy, G. Wendelschafer-Crabb, X. Yang, M. Mostafa Fraig, E. Omer, E. Miller, M. Griswold, and C. Pinkston, “Gastroparesis syndromes: Response to electrical stimulation,” *Neurogastroenterology & Motility*, 2019, in Press.

[17] T. L. Abell and J.-R. Malagelada, “Electrogastrography,” *Digestive diseases and sciences*, vol. 33, no. 8, pp. 982–992, 1988.

[18] M. P. Mintchev, Y. J. Kingma, and K. L. Bowes, “Accuracy of cutaneous recordings of gastric electrical activity,” *Gastroenterology*, vol. 104, no. 5, pp. 1273–1280, 1993.

[19] M. Buist, L. Cheng, K. Sanders, and A. Pullan, “Multiscale modelling of human gastric electric activity: can the electrogastrogram detect functional electrical uncoupling?” *Experimental physiology*, vol. 91, no. 2, pp. 383–390, 2006.

[20] S. Abid and G. Lindberg, “Electrogastrography: poor correlation with antro-duodenal manometry and doubtful clinical usefulness in adults,” *World Journal of Gastroenterology: WJG*, vol. 13, no. 38, p. 5101, 2007.

[21] A. Gharibans, S. Kim, D. Kunkel, and T. Coleman, “High-resolution electrogastrogram: A novel, noninvasive method for determining gastric slow-wave direction and speed.” *IEEE Transactions on Bio-medical Engineering*, vol. 64, no. 4, pp. 807–815, 2017.

[22] A. A. Gharibans, T. P. Coleman, H. Mousa, and D. C. Kunkel, “Spatial patterns from high-resolution electrogastrography correlate with severity of symptoms in patients with functional dyspepsia and gastroparesis,” *Clinical Gastroenterology and Hepatology*, 2019.

[23] L. K. Cheng, G. O’Grady, P. Du, J. U. Egbuji, J. A. Windsor, and A. J. Pullan, “Detailed measurements of gastric electrical activity and their implications on inverse solutions,” in *2009 Annual International Conference of the IEEE Engineering in Medicine and Biology Society*. IEEE, 2009, pp. 1302–1305.

[24] D. Ba, B. Babadi, P. L. Purdon, and E. N. Brown, “Robust spectrotemporal decomposition by iteratively reweighted least squares,” *Proceedings of the National Academy of Sciences*, vol. 111, no. 50, pp. E5336–E5345, 2014.

[25] G. Schamberg, D. Ba, and T. P. Coleman, “A modularized efficient framework for Non-Markov time series estimation,” *IEEE Trans. Signal Process.*, pp. 1–1, 2018.

[26] L. Bradshaw, A. Irimia, J. Sims, M. Gallucci, R. Palmer, and W. Richards, “Biomagnetic characterization of spatiotemporal parameters of the gastric slow wave,” *Neurogastroenterology & Motility*, vol. 18, no. 8, pp. 619–631, 2006.

[27] L. Bradshaw, L. Cheng, E. Chung, C. Obioha, J. Erickson, B. Gorman, S. Somarajan, and W. Richards, “Diabetic gastroparesis alters the biomagnetic signature of the gastric slow wave,” *Neurogastroenterology & Motility*, vol. 28, no. 6, pp. 837–848, 2016.

[28] L. Bradshaw, A. Myers, A. Redmond, J. Wikswo, and W. Richards, “Biomagnetic detection of gastric electrical activity in normal and vagotomized rabbits,” *Neurogastroenterology & Motility*, vol. 15, no. 5, pp. 475–482, 2003.

[29] W. O. Richards, L. Alan Bradshaw, D. J. Staton, C. Louis Garrard, F. Liu, S. Buchanan, and J. P. Wikswo, “Magnetoenterography (meng),” *Digestive Diseases and Sciences*, vol. 41, no. 12, pp. 2293–2301, Dec 1996. [Online]. Available: https://doi.org/10.1007/BF02100117

[30] A. A. Gharibans, B. L. Smarr, D. C. Kunkel, L. J. Kriegsfeld, H. M. Mousa, and T. P. Coleman, “Artifact rejection methodology enables continuous, noninvasive measurement of

gastric myoelectric activity in ambulatory subjects," *Sci. Rep.*, vol. 8, no. 1, p. 5019, Mar. 2018.

[31] J. H. K. Kim, A. J. Pullan, and L. K. Cheng, "Reconstruction of multiple gastric electrical wave fronts using potential-based inverse methods," *Phys. Med. Biol.*, vol. 57, no. 16, pp. 5205–5219, Aug. 2012.

[32] F. Greensite, "The temporal prior in bioelectromagnetic source imaging problems," *IEEE transactions on biomedical engineering*, vol. 50, no. 10, pp. 1152–1159, 2003.

[33] A. Fedorov, R. Beichel, J. Kalpathy-Cramer, J. Finet, J.-C. Fillion-Robin, S. Pujol, C. Bauer, D. Jennings, F. Fennessy, M. Sonka, J. Buatti, S. Aylward, J. V. Miller, S. Pieper, and R. Kikinis, "3D slicer as an image computing platform for the quantitative imaging network," *Magn. Reson. Imaging*, vol. 30, no. 9, pp. 1323–1341, Nov. 2012.

[34] P. Cignoni, M. Callieri, M. Corsini, M. Dellepiane, F. Ganovelli, G. Ranzuglia, "Meshlab: an Open-Source mesh processing tool," in *Sixth Eurographics Italian Chapter Conference*, 2008, pp. 129–136.

[35] G. O'Grady, P. Du, L. K. Cheng, J. U. Egbuji, W. J. E. P. Lammers, J. A. Windsor, and A. J. Pullan, "Origin and propagation of human gastric slow-wave activity defined by high-resolution mapping," *Am. J. Physiol. Gastrointest. Liver Physiol.*, vol. 299, no. 3, pp. G585–92, Sep. 2010.

[36] A. Smout, E. Van der Schee, and J. Grashuis, "What is measured in electrogastrography?" *Digestive diseases and sciences*, vol. 25, no. 3, pp. 179–187, 1980.

[37] R. Berry, T. Miyagawa, N. Paskaranandavadivel, P. Du, T. R. Angeli, M. L. Trew, J. A. Windsor, Y. Imai, G. O'Grady, and L. K. Cheng, "Functional physiology of the human terminal antrum defined by high-resolution electrical mapping and computational modeling," *American Journal of Physiology-Gastrointestinal and Liver Physiology*, vol. 311, no. 5, pp. G895–G902, 2016.

[38] J. Malmivuo and R. Plonsey, *Bioelectromagnetism: Principles and Applications of Bioelectric and Biomagnetic Fields*. Oxford University Press, USA, 1995.

[39] B. D. Van Veen, W. van Drongelen, M. Yuchtman, and A. Suzuki, "Localization of brain electrical activity via linearly constrained minimum variance spatial filtering," *IEEE Trans. Biomed. Eng.*, vol. 44, no. 9, pp. 867–880, Sep. 1997.

[40] R. Grech, T. Cassar, J. Muscat, K. P. Camilleri, S. G. Fabri, M. Zervakis, P. Xanthopoulos, V. Sakkalis, and B. Vanrumste, "Review on solving the inverse problem in eeg source analysis," *Journal of neuroengineering and rehabilitation*, vol. 5, no. 1, p. 25, 2008.

[41] R. Tibshirani, "Regression shrinkage and selection via the lasso," *Journal of the Royal Statistical Society. Series B (Methodological)*, pp. 267–288, 1996.

[42] A. Galka, O. Yamashita, T. Ozaki, R. Biscay, and P. Valdés-Sosa, "A solution to the dynamical inverse problem of EEG generation using spatiotemporal kalman filtering," *Neuroimage*, vol. 23, no. 2, pp. 435–453, Oct. 2004.

[43] J. H. K. Kim, A. J. Pullan, and L. K. Cheng, "Reconstruction of multiple gastric electrical wave fronts using potential based inverse methods," in *2011 Annual International Conference of the IEEE Engineering in Medicine and Biology Society*, 2011.

[44] J. Sandino, F. Gonzalez, K. Mengersen, and K. J. Gaston, "UAVs and machine learning revolutionising invasive grass and vegetation surveys in remote arid lands," *Sensors*, vol. 18, no. 2, Feb. 2018.

[45] D. Duckworth, "Pykalman version 0.9.2," https://pykalman.github.io/index.html, 2012, accessed: 2019-01-04.

[46] M. Yuan and Y. Lin, "On the non-negative garrotte estimator," *J. R. Stat. Soc. Series B Stat. Methodol.*, vol. 69, no. 2, pp. 143–161, 2007.

[47] D. Ba, B. Babadi, P. L. Purdon, and E. N. Brown, "Robust spectrotemporal decomposition by iteratively reweighted least squares," *Proc. Natl. Acad. Sci. U. S. A.*, vol. 111, no. 50, pp. E5336–45, Dec. 2014.

[48] S. Boyd, N. Parikh, and E. Chu, *Distributed optimization and statistical learning via the alternating direction method of multipliers*. Now Publishers Inc, 2011.

[49] D. Rubino, K. A. Robbins, and N. G. Hatsopoulos, "Propagating waves mediate information transfer in the motor cortex," *Nature neuroscience*, vol. 9, no. 12, p. 1549, 2006.

[50] S. Krishnasamy and T. L. Abell, "Diabetic gastroparesis: principles and current trends in management," *Diabetes Therapy*, vol. 9, no. 1, pp. 1–42, 2018.

[51] D. ODonovan, C. Feinle-Bisset, K. Jones, and M. Horowitz, "Idiopathic and diabetic gastroparesis," *Current treatment options in gastroenterology*, vol. 6, no. 4, pp. 299–309, 2003.

[52] E. Pirondini, B. Babadi, G. Obregon-Henao, C. Lamus, W. Q. Malik, M. S. Hämäläinen, and P. L. Purdon, "Computationally efficient algorithms for sparse, dynamic solutions to the eeg source localization problem," *IEEE Transactions on Biomedical Engineering*, vol. 65, no. 6, pp. 1359–1372, 2018.

[53] E. Battaglia, G. Bassotti, G. Bellone, L. Dughera, A. M. Serra, L. Chiusa, A. Repici, P. Mioli, and G. Emanuelli, "Loss of interstitial cells of cajal network in severe idiopathic gastroparesis," *World journal of gastroenterology: WJG*, vol. 12, no. 38, p. 6172, 2006.

[54] M. S. Faussone-Pellegrini, M. Grover, P. J. Pasricha, C. E. Bernard, M. S. Lurken, T. C. Smyrk, H. P. Parkman, T. L. Abell, W. J. Snape, W. L. Hasler, A. nalp Arida, L. Nguyen, K. L. Koch, J. Calles, L. Lee, J. Tonascia, F. A. Hamilton, and G. Farrugia, "Ultrastructural

differences between diabetic and idiopathic gastroparesis," *Journal of cellular and molecular medicine*, vol. 16, no. 7, pp. 1573–1581, 2012.

[55] N. Pallotta, M. Cicala, C. Frandina, and E. Corazziari, "Antro-pyloric contractile patterns and transpyloric flow after meal ingestion in humans," *The American journal of gastroenterology*, vol. 93, no. 12, pp. 2513–2522, 1998.

[56] T. R. Angeli, M. J. H. Quesada, P. Du, N. Paskaranandavadivel, S. Amirapu, A. Beyder, S. J. Asirvatham, G. Farrugia, L. K. Cheng, and G. O'Grady, "Gastric ablation as a novel therapeutic technique for modulating gastric slow wave activity," *Gastroenterology*, vol. 150, no. 4, p. S721, 2016.

[57] R. W. McCallum, J. D. Z. Chen, Z. Lin, B. D. Schirmer, R. D. Williams, and R. A. Ross, "Gastric pacing improves emptying and symptoms in patients with gastroparesis," *Gastroenterology*, vol. 114, no. 3, pp. 456–461, 1998.

[58] S. Alighaleh, L. K. Cheng, T. R. Angeli, M. Amiri, S. Sathar, G. O'Grady, and N. Paskaranandavadivel, "A novel gastric pacing device to modulate slow waves and assessment by high-resolution mapping," *IEEE Transactions on Biomedical Engineering*, 2019.

[59] I. Sarosiek, B. Davis, E. Eichler, and R. W. McCallum, "Surgical approaches to treatment of gastroparesis: gastric electrical stimulation, pyloroplasty, total gastrectomy and enteral feeding tubes," *Gastroenterol. Clin. North Am.*, vol. 44, no. 1, pp. 151–167, Mar. 2015.

[60] S. Alighaleh, T. R. Angeli, S. Sathar, G. O'Grady, L. K. Cheng, and N. Paskaranandavadivel, "Design and application of a novel gastric pacemaker," *Conf. Proc. IEEE Eng. Med. Biol. Soc.*, vol. 2017, pp. 2181–2184, Jul. 2017.

[61] T. Abell, "Gastroparesis Syndromes: Pathophysiology and Response to Electrical Stimulation," https://clinicaltrials.gov/ct2/show/NCT03178370, 2017.

[62] S. Alighaleh, T. R. Angeli, S. Sathar, G. O'Grady, L. K. Cheng, and N. Paskaranandavadivel, "144 - Real-Time evaluation of a novel gastric pacing device with High-Resolution mapping," *Gastroenterology*, vol. 154, no. 6, Supplement 1, pp. S–39, 2018.

[63] H. Cochet, R. Dubois, F. Sacher, N. Derval, M. Sermesant, M. Hocini, M. Montaudon, M. Haïssaguerre, F. Laurent, and P. Jaïs, "Cardiac arrythmias: multimodal assessment integrating body surface ECG mapping into cardiac imaging," *Radiology*, vol. 271, no. 1, pp. 239–247, Apr. 2014.

[64] M. Haissaguerre, M. Hocini, A. J. Shah, N. Derval, F. Sacher, P. Jais, and R. Dubois, "Noninvasive panoramic mapping of human atrial fibrillation mechanisms: a feasibility report," *J. Cardiovasc. Electrophysiol.*, vol. 24, no. 6, pp. 711–717, Jun. 2013.

[65] M. Ferrua and R. Singh, "Modeling the fluid dynamics in a human stomach to gain insight of food digestion," *Journal of food science*, vol. 75, no. 7, pp. R151–R162, 2010.

[66] H. Kozu, I. Kobayashi, M. Nakajima, K. Uemura, S. Sato, and S. Ichikawa, “Analysis of flow phenomena in gastric contents induced by human gastric peristalsis using cfd,” *Food Biophysics*, vol. 5, no. 4, pp. 330–336, 2010.

[67] B. Kothapalli, “Electrogastrogram simulation using a three-dimensional model,” *Medical and Biological Engineering and Computing*, vol. 31, no. 5, pp. 482–486, Sep 1993. [Online]. Available: https://doi.org/10.1007/BF02441983

[68] S. Calder, G. OGrady, L. K. Cheng, and P. Du, “Torso-tank validation of high-resolution electrogastrography (egg): Forward modelling, methodology and results,” *Annals of biomedical engineering*, vol. 46, pp. 1183–1193, 2018.

[69] L. A. Bradshaw, A. Myers, J. P. Wikswo, and W. O. Richards, “A spatio-temporal dipole simulation of gastrointestinal magnetic fields,” *IEEE transactions on biomedical engineering*, vol. 50, no. 7, pp. 836–847, 2003.

[70] A. Belloni and V. Chernozhukov, “Least squares after model selection in high-dimensional sparse models,” *Bernoulli*, vol. 19, no. 2, pp. 521–547, 2013.

[71] D. Chételat, J. Lederer, and J. Salmon, “Optimal two-step prediction in regression,” *Electronic Journal of Statistics*, vol. 11, no. 1, pp. 2519–2546, 2017.

[72] C. V. Almario, M. S. Keller, M. Chen, K. Lasch, L. Ursos, J. Shklovskaya, G. Y. Melmed, and B. M. Spiegel, “Optimizing selection of biologics in inflammatory bowel disease: development of an online patient decision aid using conjoint analysis,” *American Journal of Gastroenterology*, vol. 113, no. 1, pp. 58–71, 2018.

[73] H. El-Serag and N. Talley, “The prevalence and clinical course of functional dyspepsia,” *Alimentary pharmacology & therapeutics*, vol. 19, no. 6, pp. 643–654, 2004.

[74] A. B. Allegra, A. A. Gharibans, G. E. Schamberg, D. C. Kunkel, and T. P. Coleman, “Bayesian inverse methods for spatiotemporal characterization of gastric electrical activity from cutaneous multi-electrode recordings,” *PloS one*, vol. 14, no. 10, p. e0220315, 2019.

[75] P. Ngatchou, A. Zarei, and A. El-Sharkawi, “Pareto multi objective optimization,” in *Proceedings of the 13th International Conference on, Intelligent Systems Application to Power Systems*. IEEE, 2005, pp. 84–91.

[76] J. N. Tehrani, A. McEwan, C. Jin, and A. Van Schaik, “L1 regularization method in electrical impedance tomography by using the l1-curve (pareto frontier curve),” *Applied Mathematical Modelling*, vol. 36, no. 3, pp. 1095–1105, 2012.

[77] J. Rissanen, “A universal prior for integers and estimation by minimum description length,” *The Annals of statistics*, pp. 416–431, 1983.

[78] H. Zou, T. Hastie, and R. Tibshirani, “On the degrees of freedom of the lasso,” *The Annals of Statistics*, vol. 35, no. 5, pp. 2173–2192, 2007.

[79] R. J. Tibshirani and J. Taylor, “Degrees of freedom in lasso problems,” *The Annals of Statistics*, pp. 1198–1232, 2012.

[80] J. Hadar and W. R. Russell, “Rules for ordering uncertain prospects,” *The American economic review*, vol. 59, no. 1, pp. 25–34, 1969.

[81] R. Davidson and J.-Y. Duclos, “Statistical inference for stochastic dominance and for the measurement of poverty and inequality,” *Econometrica*, vol. 68, no. 6, pp. 1435–1464, 2000.

[82] J. F. Kurniawan, B. Tjhia, V. M. Wu, A. Shin, N. L. Sit, T. Pham, A. Nguyen, C. Li, R. Kumar, M. Aguilar-Rivera, I. Lerman, D. C. Kunkel, and T. P. Coleman, “An adhesive-integrated stretchable silver-silver chloride electrode array for unobtrusive monitoring of gastric neuromuscular activity,” *Advanced Materials Technologies*, vol. 6, no. 5, p. 2001229, 2021.

[83] N. Paskaranandavadivel, T. R. Angeli, T. Manson, A. Stocker, L. McElmurray, G. OGrady, T. Abell, and L. K. Cheng, “Multi-day, multi-sensor ambulatory monitoring of gastric electrical activity,” *Physiological measurement*, vol. 40, no. 2, p. 025011, 2019.

[84] A. Shine, S. Ahmed, L. McElmurray, A. Stocker, C. Pinkston, and T. Abell, “116–electrogastography at baseline and response to temporary gastric electrical stimulation–a comparison of cutaneous with mucosal recordings,” *Gastroenterology*, vol. 156, no. 6, pp. S–30, 2019.

[85] A. B. Allegra, K. C. David, and T. P. Coleman, “Model selection procedures for bayesian inference based source localization of the gastric slow wave,” 2021, manuscript submitted for publication.

[86] J. F. Kurniawan, A. B. Allegra, T. Pham, A. K. Nguyen, N. L. J. Sit, B. Tjhia, A. J. Shin, and T. P. Coleman, “Electrochemical performance study of ag/agcl and au flexible electrodes for unobtrusive monitoring of human biopotential,” 2021, unpublished manuscript.

[87] L. Gomes, “Machine-learning maestro michael jordan on the delusions of big data and other huge engineering efforts,” *IEEE spectrum*, vol. 20, 2014.

[88] L. Malagò and G. Pistone, “Information geometry of the gaussian distribution in view of stochastic optimization,” in *Proceedings of the 2015 ACM Conference on Foundations of Genetic Algorithms XIII*, 2015, pp. 150–162.

[89] Y. C. Eldar, *Rethinking biased estimation: Improving maximum likelihood and the Cramér-Rao bound*. Now Publishers Inc, 2008.

[90] V. V. Fedorov, *Theory of optimal experiments*. Elsevier, 2013.

[91] E. Lutwak, S. Lv, D. Yang, and G. Zhang, “Extensions of fisher information and stam’s inequality,” *IEEE transactions on information theory*, vol. 58, no. 3, pp. 1319–1327, 2012.

[92] A. A. Gharibans, S. Kim, D. Kunkel, and T. P. Coleman, “High-Resolution electrogastrogram: A novel, noninvasive method for determining gastric Slow-Wave direction and speed,” *IEEE Trans. Biomed. Eng.*, vol. 64, no. 4, pp. 807–815, Apr. 2017.

[93] E. Greenwald, E. So, M. Mollazadeh, C. Maier, R. Etienne-Cummings, N. Thakor, and G. Cauwenberghs, “A 5 w/channel 9b-enob bioadc array for electrocortical recording,” in *2015 IEEE Biomedical Circuits and Systems Conference (BioCAS)*, 2015, pp. 1–4.

[94] E. Greenwald, E. So, Q. Wang, M. Mollazadeh, C. Maier, R. Etienne-Cummings, G. Cauwenberghs, and N. Thakor, “A bidirectional neural interface ic with chopper stabilized bioadc array and charge balanced stimulator,” *IEEE transactions on biomedical circuits and systems*, vol. 10, no. 5, pp. 990–1002, 2016.